

Surfactant induced flows in thin liquid films : an experimental study

Citation for published version (APA):

Sinz, D. K. N. (2012). *Surfactant induced flows in thin liquid films : an experimental study*. [Phd Thesis 1 (Research TU/e / Graduation TU/e), Applied Physics and Science Education]. Technische Universiteit Eindhoven. <https://doi.org/10.6100/IR737561>

DOI:

[10.6100/IR737561](https://doi.org/10.6100/IR737561)

Document status and date:

Published: 01/01/2012

Document Version:

Publisher's PDF, also known as Version of Record (includes final page, issue and volume numbers)

Please check the document version of this publication:

- A submitted manuscript is the version of the article upon submission and before peer-review. There can be important differences between the submitted version and the official published version of record. People interested in the research are advised to contact the author for the final version of the publication, or visit the DOI to the publisher's website.
- The final author version and the galley proof are versions of the publication after peer review.
- The final published version features the final layout of the paper including the volume, issue and page numbers.

[Link to publication](#)

General rights

Copyright and moral rights for the publications made accessible in the public portal are retained by the authors and/or other copyright owners and it is a condition of accessing publications that users recognise and abide by the legal requirements associated with these rights.

- Users may download and print one copy of any publication from the public portal for the purpose of private study or research.
- You may not further distribute the material or use it for any profit-making activity or commercial gain
- You may freely distribute the URL identifying the publication in the public portal.

If the publication is distributed under the terms of Article 25fa of the Dutch Copyright Act, indicated by the "Taverne" license above, please follow below link for the End User Agreement:

www.tue.nl/taverne

Take down policy

If you believe that this document breaches copyright please contact us at:

openaccess@tue.nl

providing details and we will investigate your claim.

**Surfactant induced flows
in thin liquid films
-
An experimental study**

David Karl Noah Sinz

Cover illustration: Experimental images by David K. N. Sinz, see chapters 5 & 6.

This research was financially supported by the Dutch Technology Foundation STW (project number 08066); in cooperation with Shell International Exploration and Production.

© Copyright 2012, David Karl Noah Sinz
Printed by Universiteitsdrukkerij TUE, Eindhoven, The Netherlands

CIP-DATA LIBRARY TECHNISCHE UNIVERSITEIT EINDHOVEN

Sinz, David K. N.

Surfactant induced flows in thin liquid films - An experimental study / by David Karl Noah Sinz. - Eindhoven: Technische Universiteit Eindhoven, 2012. - Proefschrift.

A catalogue record is available from the Eindhoven University of Technology Library

ISBN: 978-90-386-3260-5
NUR: 926

**Surfactant induced flows
in thin liquid films**

An experimental study

PROEFSCHRIFT

ter verkrijging van de graad van doctor aan de
Technische Universiteit Eindhoven, op gezag van de
rector magnificus, prof.dr.ir. C.J. van Duijn, voor een
commissie aangewezen door het College voor
Promoties in het openbaar te verdedigen
op dinsdag 6 november 2012 om 16.00 uur

door

David Karl Noah Sinz

geboren te Stuttgart, Duitsland

Dit proefschrift is goedgekeurd door de promotor:

prof.dr. A. A. Darhuber

Für Annabella und Heather

Contents

1	Introduction	1
1.1	Literature overview - Surfactant spreading	3
1.2	Literature overview - Self-propulsion phenomena	5
1.3	Outline of this thesis and technological context	7
2	Immiscible surfactant droplets on thin liquid films	11
2.1	Setup	12
2.1.1	Interference microscopy studies of the sub-phase displacement	14
2.1.2	Fluorescence microscopy studies of sub-phase expulsion dynamics	14
2.2	Results	15
2.2.1	Stable surfactant spreading dynamics	15
2.2.2	Instability during immiscible surfactant spreading	17
2.2.3	Expulsion induced modification of the spreading dynamics	19
2.2.4	Sub-phase expulsion dynamics near the three-phase contact line	20
2.2.5	Global expulsion	21
2.2.6	Local expulsion	23
2.3	Summary	25
3	Surfactant spreading on a sub-phase rivulet defined by a chemical surface pattern	27
3.1	Experimental setup	28
3.1.1	Chemical patterning	28
3.1.2	Coating of patterned substrates	28
3.2	Insoluble surfactant spreading	30
3.2.1	Propagation rate of the surfactant	33
3.2.2	Sub-phase morphology evolution	35
3.3	Soluble surfactant spreading	37
3.3.1	Solid deposition	40
3.3.2	Solution deposition	42
3.4	Summary	43

4	Surfactant spreading at the interface of two thin liquid films	45
4.1	Introduction	45
4.2	Sample fabrication and experimental setup	46
4.3	Results	48
4.4	Summary	52
5	Marangoni transport of surfactants along discontinuous liquid-liquid interfaces	55
5.1	Introduction	55
5.2	Sample fabrication and experimental setup	56
5.3	Transport rate	59
5.4	Pillar deformation	60
5.5	Low partitioning coefficient surfactant	63
5.6	Discussion and outlook	63
6	Self-sustained drop motion	65
6.1	Sample preparation	65
6.2	Interfacial tension measurements, material parameters	68
6.3	Drop propagation	68
6.4	Sub-phase mapping via fluorescence microscopy	69
6.5	A scaling argument for the drop propulsion	70
6.6	Viscosity modulation	71
6.7	Meandering motion	72
6.8	Intermittent propulsion	77
6.9	Summary and conclusions	80
7	Self-propelling surfactant droplets in chemically-confined microfluidics	83
7.1	Experimental details	84
7.2	Cargo loading and transport	86
7.3	Fluidic junction - splitting and routing	87
7.4	Summary	90
8	Summary and Perspectives	91
	Bibliography	94
	List of symbols	107
	List of Publications	111
	Summary	113
	Acknowledgments	115

Chapter 1

Introduction

Typically the influence of surface or interfacial tension on (most) large scale fluid dynamics problems is negligible. As the spatial dimensions are reduced, the surface-to-volume ratio and correspondingly the balance of forces changes such that interfacial tension gradients or Marangoni stresses are often the dominant driving force behind fluid flow. The probably most prominent example of these Marangoni flows are the widely known *Tears of Wine*. A shadowgraphy image of this phenomenon is shown in Fig. 1.1. Besides offering fascinating dinner table experiments, Marangoni flows are also harnessed in technological applications such as solution deposition techniques or liquid actuation in microfluidic devices.

A variety of mechanisms can give rise to Marangoni stresses and flows, such as thermal and compositional gradients. This thesis is focused on surfactant-induced Marangoni flows. Surfactant is an abbreviation for *surface-active agent* and denotes substances that

Figure 1.1: The probably most famous example of Marangoni flow, the Tears of Wine. The shadowgraphy image gives an idea of the complex flow phenomena as a result of surface tension gradients arising due to the evaporation induced non-uniform alcohol concentration in the liquid that is wetting the wine glass. The glass was illuminated from the right and the image was recorded with a consumer digital camera.



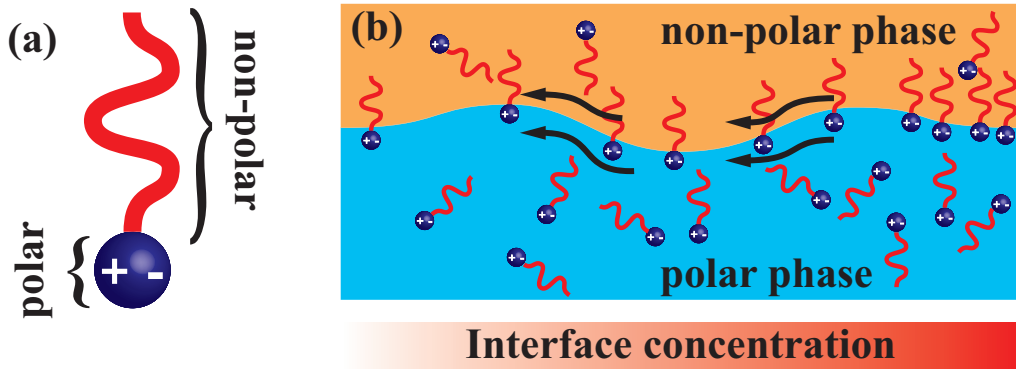


Figure 1.2: (a) Sketch illustrating the principal molecular structure of a surface-active substance. Surfactant molecules usually comprise a polar and a non-polar part, resulting in their tendency to accumulate at fluid interfaces. (b) Interface between a polar and a non-polar fluid in the presence of a non-uniformly distributed surfactant. The surfactant accumulates at the interface of the two fluids, lowering the interfacial tension. A non-uniform spatial distribution gives rise to Marangoni stresses, which in turn induce flow at the interface from regions of high interfacial concentration or low interfacial tension to regions of low interfacial concentration or high interfacial tension.

reduce interfacial tension due to their tendency to adsorb at interfaces. The origin of their surface-active nature lies in their amphiphilic molecular structure, i.e. these substances generally comprise a polar and a non-polar part. This molecular structure is qualitatively sketched in Fig. 1.2(a). At a fluid-fluid interface, regions with a high surfactant concentration therefore have a lower interfacial tension than regions of low surfactant concentration. This gives rise to flow and facilitates the spreading of the surfactants from regions of high to regions of low surfactant concentration^{3,87,152}, as sketched in Fig. 1.2(b). In this sketch the interface between a polar and a non-polar liquid is illustrated in the presence of a surfactant. Surfactant is present in both bulk phases (which dependent on the system configuration might not be the case) in different concentrations. The concentration of the surfactant at the interface increases from the left to right side. The direction of the resulting Marangoni-stress induced flow from right to left at the liquid-liquid interface as a consequence of the non-uniform surfactant distribution is indicated by the black arrows.

The work on surfactant induced flows described in this thesis can be divided in two main topics, the spreading of surfactants along liquid-air and liquid-liquid interfaces and the fascinating phenomenon of surfactant self-propulsion. In the remainder of this chapter, first an overview of the literature regarding surfactant spreading will be given, followed by an overview of self-propulsion phenomena. The introduction concludes with an outline of the structure of the thesis and an overview of the treated topics. Fur-

thermore, surfactant spreading and specifically the work presented here will be discussed in the context of technological processes. One of them being Enhanced Oil Recovery⁸³ (EOR) in this field, the spreading of surfactant could provide an interesting transport mechanism.

1.1 Literature overview - Surfactant spreading

Existing studies on surfactant spreading and the associated flows predominantly focused on the far field spreading dynamics in simple systems at liquid-air interfaces. Oil and surfactant spreading along the surface of deep liquid layers has been investigated by Fay⁴³ and Hoult⁶⁶. Huh *et al.*⁶⁷ studied the spreading rate of a thin liquid on an immiscible liquid substrate by means of experiments and an approximate quasi-steady analysis. The driving force was assumed to be a combination of gravity and interfacial forces. Foda and Cox⁴⁷ considered the spreading of a thin liquid film on a water-air interface for the case where surface tension gradients drive the motion. Camp and Berg¹⁸ performed experiments regarding the unidirectional spreading of several pure oils and oil-surfactant mixtures on water in the surface-tension regime and reported data consistent with the similarity solution of Foda and Cox⁴⁷. The leading edge position L of a spreading oleic acid film was determined to scale with time as $L \sim t^\alpha$ with the spreading exponent $\alpha = 3/4$. Jensen⁷² presented a detailed theoretical study and showed that for spreading over uncontaminated layers $L \sim ((\partial\gamma/\partial\Gamma)^2 t^3)^{1/[2(n+2)]}$, where $n = 1$ for a strip geometry and $n = 2$ for a droplet. For pre-contaminated layers he derived the asymptotic scaling $L \sim t^{3/4}$ for both strip- and droplet geometries. Joos and Van Hunsel⁷⁸ considered the spreading of droplets of surfactant solutions on immiscible organic liquids and found a spreading exponent of $3/4$ for a solution of a fluorinated surfactant on CCl_4 . For a different material combination Svitova *et al.*¹⁴⁰ reported spreading dynamics that cannot be represented by a powerlaw and that proceeded slower for pure dodecane than for a substantially more viscous mineral oil as the sub-phase. Surfactant spreading at the air-liquid interface of thin liquid films has been studied extensively in the past^{7,11,41,45,46,51,52,56,71,74,75,92,93,136,142,143,149}. Ahmad and Hansen⁷ reported on the spreading of oleic acid on glycerol films and found a spreading exponent of $\alpha = 0.5$. Using experiments and theoretical models based on the lubrication approximation, Troian *et al.*¹⁴³ as well as Grotberg and co-workers^{11,51,52} investigated axisymmetric unsteady spreading of surfactant monolayers on thin liquid films. Film thinning occurred in the vicinity of the deposited surfactant as well as film thickening and the formation of a rim near the surfactant leading edge. Jensen and Grotberg presented a model for the spreading of soluble surfactants⁷⁴ considering linearized sorption kinetics and fast vertical diffusion across the film thickness. Different solubilities of the surfactant induced qualitative differences in the flow patterns. Jensen⁷¹ discussed similarity solutions of surfactant driven flow problems. Starov *et al.* treated the spreading of a drop of a surfactant solution over a thin water film as a two-stage process¹³⁶. In a first stage the

surface concentration was kept constant to account for micellar dissolution, followed by a second stage where, after micelle depletion, the total mass of surfactant adsorbed at the surface was assumed constant.

Troian *et al.*¹⁴³, Frank and Garoff⁴⁹, He and Ketterson⁶⁴, Matar and Troian^{92,93}, Cachile *et al.*^{16,17}, Fischer and Troian^{45,46}, Afsar-Siddiqui *et al.*⁴⁻⁶, Warner *et al.*¹⁴⁹ and Jensen and Naire⁷⁵ considered instabilities occurring near the perimeter of spreading surfactant droplets and surfactant fronts. Evans *et al.* investigated the role of surfactants in the formation of crater defects in drying paint layers⁴¹. Dussaud *et al.* studied the dynamics of insoluble surfactant monolayers spreading on glycerol films³⁵. Experimental film thickness profiles were obtained by means of Moire topography. A spreading exponent of $\alpha = 0.23$ was found, which is close to the analytically predicted value for radial spreading of a finite quantity of deposited surfactant. Craster and Matar²⁴ elucidated the effect of autophobing of surfactant solutions. The combined effect of temperature and surfactant concentration gradients was studied by Borhan *et al.*, Chen and Stebe, Edmonstone and Matar, as well as Hanumanthu and Stebe^{12,22,39,59}.

In the context of pulmonary surfactant transport, several groups investigated exogenous surfactant spreading along thin liquid films adhering to the interior surface of hollow tubes^{33,40,144,151}. Davis *et al.*³³ studied axisymmetric and steady flows and reported that in the limit of negligible radial interface curvature, i.e. when the tube radius R is very much larger than the adhering film thickness h , i.e., $\delta \equiv h/R \rightarrow 0$, the flow is solely influenced by surface tension gradients. A qualitatively different behavior was predicted for small but finite δ . Espinosa *et al.*⁴⁰ found that the effect of circumferential curvature was negligible, as if spreading occurred over a flat surface. For a linear equation of state a spreading exponent $\alpha = \frac{1}{3}$ was reported. Furthermore, the presence of a resident endogenous surfactant amplified the spreading rate. Williams and Jensen¹⁵¹ considered the effect of circumferential non-uniformities of the liquid film thickness and concluded that flow-induced shape deformations of the liquid lining influence the spreading dynamics only weakly. Follows *et al.*⁴⁸ applied neutron scattering and observed the presence of multilayers at the surface of exogenous lung surfactant solutions. The authors recommended that their presence be incorporated into the existing models, which are largely based on the assumption that surfactants adsorb as monolayers. Fallest *et al.*⁴² presented experimental data of the spatio-temporal distribution of a fluorescent surfactant during spreading on a glycerol layer.

Recently Berg⁹ presented the first systematic study of Marangoni driven surfactant spreading at the interface between two deep liquid layers. In this study Berg used deep layers of decane and water. The spreading kinetics of several types of surfactant at the interface between the two layers were investigated experimentally. A scaling relation, derived by balancing the interfacial tension gradient and viscous stresses in the boundary layers in the two liquid phases, was in quantitative agreement with the experimental data.

1.2 Literature overview - Self-propulsion phenomena

The physicochemical hydrodynamics underlying the self-sustained motion, or self-propulsion, of droplets and small solid objects have received considerable attention in recent years. The probably earliest and one of the most extensively scientifically documented examples of this phenomena is the self-sustained motion of so-called camphor boats^{90,105,107,123}. There are however a variety of manifestations of self-propulsion.

A theoretical analysis of the motion exhibited by liquid drops on surfaces exhibiting a gradient in either the surface free energy or temperature was presented by Brochard¹³. Chaudhury and Whitesides showed in their experiments that surfaces exhibiting a surface energy gradient can facilitate the motion of water droplets against the direction of gravity²¹. Bain *et al.* studied the self-sustained motion of alkane droplets on hydrophilic stripes on chemically patterned glass substrates. The droplets contained a fluorinated fatty acid that can adsorb onto the clean glass and decrease its interfacial free energy, this in conjunction with the asymmetry due to the initial droplet placement in one corner of the hydrophilic pattern induces and sustains a directed motion of the alkane droplets⁸. Dos Santos and Ondarcuhu quantitatively studied the motion of these droplets using a model relating the droplet velocity to the difference in contact angles in the front and back of the droplets. The modification of the contact angle in their model is based on first-order reaction kinetics and reproduced the effects of droplet size as well as concentration of the wettability modifier¹²⁶. An experimental study of the motion of an iodine and potassium iodide containing oil droplet on an aqueous cationic surfactant solution was conducted by Magome and Yoshikawa⁸⁹. They attribute the motion of the droplet to temporal oscillations of the oil water interfacial tension observed when the two solutions are brought into contact. As already mentioned a prominent example of self-propulsion in scientific literature is the motion of camphor on water which has been studied for a variety of system configurations by various groups^{62,63,80,90,96-105,107-110,112,113,115,116,128,135,138}. Yoshikawa *et al.* studied the motion of camphor fragments of asymmetric shapes which exhibited a self-rotary mode of motion while fragments with a left-right symmetry and back-front asymmetry were reported to undergo a translational motion¹⁰⁷. Spontaneous switching between modes of motion for a camphor scraping was reported by Nakata and Hayashima¹⁰¹. Nakata *et al.* found for a camphoric acid scraping the mode of self-motion to be dependent on the pH of the aqueous phase with a change from constant translatory motion over intermittent or mode switching motion to rest with increasing pH-value¹⁰⁸. Schwartz and Eley¹²⁹ investigated the motion of droplets on substrates exhibiting spatially varying surface energies and proposed a numerical model using the lubrication approximation including viscous, capillary, disjoining and gravitational forces. A comparison with experimental results revealed qualitative agreement. Spontaneous deformation and translation of a mercury drop in a concentration field as a result of the dissolution of an oxidant crystal was investigated by Menzinger *et al.*¹¹⁴. The motion is attributed to imbalances in the interfacial tension of the mercury drop due to nonuniform oxidization. The influence of vibration

on the motion of liquid micro-droplets on surface exhibiting a spatial gradient in surface energy was studied by Daniel and Chaudhury²⁶. An increase in propulsion velocity by a factor of ≈ 5 was found and attributed to a vibrationally induced reduction of the retarding effect of contact angle hysteresis. Laibinis *et al.* employed droplets of non-polar liquid containing a wettability modifier on chemically patterned surfaces to study reactive wetting. Experimental results for the propulsion velocity as a function of the wettability modifier concentration are compared to theoretical predictions based on a kinetic as well as an equilibrium analyses⁸⁶. Whitesides *et al.* studied the self-assembly of aggregates and their influence on the dynamical behavior of autonomously moving particles. The considered particles were hemispheric plates, with varying wettability around their perimeter, moving on an aqueous hydrogen peroxide solution. The driving force of the motion was the impulse of bubbles generated by platinum-catalyzed decomposition of hydrogen peroxide. Specific wettability modification of the perimeter of the plates resulted in complex dynamics of single particles, varying interaction of several particles as well as self-assembly of particle aggregates inducing new dynamic behavior⁷⁰. Micron sized rods, segmentally constructed from Pt and Au, exhibiting self-sustained motion were studied by Paxton *et al.*¹¹⁹. Their autonomous motion was driven by Pt catalyzed decomposition of the surrounding aqueous hydrogen peroxide solution and the resulting formation of oxygen. This, due to the segmental structure of the rod, localized process gives rise to an interfacial tension gradient that is continuously re-established as the rod moves. While the origin of the driving force for self-propulsion is the Pt-catalyzed decomposition of hydrogen peroxide for both systems described by Paxton *et al.*¹¹⁹ and Whitesides *et al.*⁷⁰ the direction of the motion is inverted with respect to the location of the Pt catalyst as a result of the different driving mechanisms which are impulse and interfacial tension gradient due to bubble formation for the system described by Whitesides *et al.*⁷⁰ and Paxton *et al.*¹¹⁹, respectively. A concentration dependent change from uniform to intermittent autonomous motion of a 1,10-phenanthroline grain floating on an aqueous FeSO₄ solution was observed by Nakata *et al.*¹⁰⁶. Genzer *et al.*¹²⁰ found that the self-propulsion speed of water droplets on porous substrates exhibiting a wettability gradient is higher than the speed on an analogous smooth surface. A scaling analysis attributing this increased velocity to reduced friction at the liquid substrate interface is in quantitative agreement with the reported experiments. Coupling evolution equations for the droplets height profile and the density profile of an adsorbate layer Thiele *et al.*⁷⁶ studied the self-sustained motion of droplets on partially wetting substrates. Using a magnetic field Kline *et al.*⁸¹ were able to remote control the autonomous movement of striped metallic nano-rods propelled by Pt-catalyzed hydrogen peroxide decomposition.

Lazar *et al.*⁸⁴ presented an analysis of the reversible self-propelled motion exhibited by droplets of long chain alkanes. The melting enthalpy was identified as the energetic source of motion of droplets forming on melting solid alkane multilayers. For temperatures slightly above the bulk melting temperature, the multilayers melt into droplets moving in a self-avoiding, random path. The solid alkane is consumed by the droplets during their motion. At temperatures slightly below bulk melting the process is reversed.

The droplets then move backwards and leave a narrowing solid trail fed by the depleting droplet.

The self-propelled motion of miniature semiconductor diodes was studied by Velev *et al.*¹⁹. Floating on a water surface in an electric field, the diodes moved due to particle localized electro-osmotic flow. Using this conversion of electrical energy into mechanical propulsion, locally distributed pumping or mixing was demonstrated by embedding the diodes in the walls of micro-fluidic channels. Grzybowski *et al.*¹³⁵ used self-propelling particles, containing camphor, to study the dynamic self-assembly of particle ensembles. In a bounded geometry a critical particle density was reported which resulted in a transition from synchronized motion to the formation of an open lattice structure. This transition was attributed to the repulsive hydrodynamic interaction of these particles. Certain self-propelling droplets can also be used to solve a maze problem as described by Grzybowski *et al.*⁸². In their experiments, the droplets of an organic solvent, containing a surfactant with pH-dependent surface activity, navigated autonomously through a maze of micro-fluidic channels in which a pH-gradient was established. Recently there has also been focus on the schooling behavior and interactions of multitudes of autonomously moving objects^{65,68,70,128}.

1.3 Outline of this thesis and technological context

In the remainder of this thesis surfactant induced surface tension gradient driven flows in an array of system configurations with increasing complexity will be studied. In Chapter 2 the flow dynamics resulting from the deposition of a droplet of an insoluble surfactant onto a thin liquid film covering a solid substrate will be described. This configuration is a model system widely used in the study of insoluble surfactant spreading at the liquid-air interface. Besides the radially outwards directed displacement of the subphase, induced by the resulting Marangoni stresses, the effect of the conditions in the vicinity of the surfactant source on this displacement is elucidated. The application of interference and fluorescence microscopy led to the conclusion that these conditions have a pronounced influence on the far field spreading rate of the surfactant and sub-phase displacement. Furthermore a novel oscillatory contact line instability of the surfactant droplet is described in this context.

Injection of surfactant solutions is considered a potential means for extracting larger fractions of the oil present in underground oil reservoirs^{127,131}. Surfactant-induced reduction of interfacial tension facilitates deformations of oil-brine interfaces and the mobilization of trapped oil. This displacement of oil in the rock matrix of a reservoir is characterized by the Capillary number which is the ratio of viscous to interfacial forces. Lowering the oil-brine interfacial tension increases the Capillary number which is favorable for the displacement of oil from the porous rock matrix and can therefore have a positive effect on achievable oil recovery rates. This mechanism acts primarily in rock pores that are accessible to pressure-driven flow from injection- to production wells.

As previously outlined, spatially non-uniform surfactant distribution induces flow due to the resulting interfacial tension gradients. In the context of oil recovery these flows could be utilized to transport surfactant and functional substances, such as wettability modifiers, along dead-end pores that are inaccessible to pressure-driven transport. Under reservoir conditions the liquid-liquid interfaces between the oil and brine are subject to a multitude of confinements. These confinements can be of physical nature, i.e. imposed by rock formations, or chemical, i.e. due to non-uniform wettability of the pores in which the oil is present.

To investigate the effect of wettability induced confinement on surfactant spreading I used chemical surface patterns. In Chapter 3 the influence of spatial confinement of the sub-phase film via a chemical surface pattern on surfactant-induced flows will be presented. The wettability patterns impose a spatial restriction that leads to a pronounced transition in the morphology evolution of the flowing thin film. The experimental results are in excellent agreement with numerical simulations by Myroslava Hanyak^{61,134}. While the studies in Chapter 2 and 3 are conducted for liquid air interfaces in an oil reservoir the spreading has to occur along the interface between liquid films. This is addressed in Chapter 4 where the surfactant spreading along the liquid-liquid interface of thin films is studied, a system configuration not yet considered in the existing literature.

All existing studies in the field of surfactant spreading exclusively regards continuous interfaces. Using an optical absorption technique, I demonstrate in Chapter 5 that efficient Marangoni-stress driven transport of surfactants is not restricted to continuous liquid-liquid interfaces. This novel phenomenon of convective surfactant spreading along discontinuous interfaces is a discovery directly relevant to the spreading of surfactants in an oil reservoir. In these porous underground rock formations the oil-water interface is not necessarily connected, such that surfactant spreading through a reservoir is likely to involve transport over interface discontinuities.

In future studies it would be of interest to investigate the possibility of utilizing the described surfactant induced flow phenomena as a transport mechanism of functional substances¹⁵⁰, e.g. wettability modifiers. This would be specifically interesting for dead-end pore geometries as they are inaccessible to pressure driven flows. Suitable alteration of the wettability conditions in such pores might induce oil expulsion, e.g. via gravity driven mobilization of previously trapped oil volumes.

Another technological application in which thin film fluid flow plays a significant role is the lubrication of rolling bearings. Under correct operating conditions the lubrication of the bearing is often the determining factor for its lifetime^{25,145}. A rolling bearing is properly lubricated if the rolling element is separated from the raceway surface via low shear separation layer formed by the lubricant (oil or grease). Fluorinated surfactants could possibly modulate the surface tension of lubricant fluids to induce flows. Already minute contributions towards the reformation of lubrication layers could significantly extend the service life of closed rolling bearings where lubrication cannot be ensured via regular maintenance. In this context it could also be of interest to investigate the possibility of internal fluid management via surface energy modification of the

raceway surface.

The implications of surfactant induced flow phenomena in printing and coating applications is another interesting field for future research. Surfactants causing crater formation and dry spot nucleation in coating layers can induce mottling and therefore, in the case of automotive application, be a precursor of wear and corrosion¹⁴⁸. In inkjet printing applications the presence of surfactants in the ink was recently shown to retard the leveling process of printed lines⁶⁰. This extends the drying time of the inks since solidification prior to leveling should be avoided to ensure high quality prints. If the combination of qualitatively different surfactants, e.g. slow and fast adsorbing types, could reduce the flow retarding surface tension gradients induced by the surface deformation during leveling the combination would have a positive effect on the leveling times.

In addition to the spreading of surfactants, I also studied the self-propulsion of surfactant droplets and the results are presented in Chapter 6 and 7. The self-propulsion dynamics exhibited by insoluble surfactant droplets on thin liquid films are systematically investigated in Chapter 6. This systematic study is complemented with the outline of a potential application in microfluidic devices in Chapter 7. In this context I am describing the novel phenomenon of transporting solid cargo particles using these self-propelling droplets. It is also demonstrated that these droplets can be routed across micro-fluidic networks by controlling the temperature field around the drop e.g. using an infrared laser.

Chapter 2

Immiscible surfactant droplets on thin liquid films

Increasing the surface concentration Γ of a surfactant at the interface of two fluids decreases the interfacial or, in the case of a liquid-air interface, the surface tension γ . A localized increase in the surface concentration therefore gives rise to flow, induced by Marangoni stresses at the fluid interface. In contrast to spreading on deep liquid layers^{18,36,37,47,66,72,141}, surfactant spreading on thin liquid films induces pronounced modulations in the morphology of the sub-phase. The formation and propagation of a rim near the leading edge of the spreading surfactant front as well as substantial film thinning in the proximity of the surfactant source are characteristic for the spreading of surfactant on a thin liquid film^{11,51,52,57,73,133,134,142,143}. A fingering instability is often observed near the perimeter of spreading droplets and fronts of surfactant solutions^{16,17,45,46,49,64,92,93,142,143}. The prime origin of the instability was identified, by Warner *et al.*, as the presence of adverse mobility gradient regions at the leading edge of a spreading drop covered with an insoluble surfactant¹⁴⁹. Matar and Craster⁹¹ have recently given a review of surfactant spreading dynamics, covering stable spreading as well as fingering- and oscillatory instabilities and certain cases of self-propulsion.

The previous investigations mentioned above primarily focused either on soluble surfactants or on the influence of Marangoni-stresses on the evolution of thin liquid films *distant* from the location of the initial surfactant deposition. In this chapter, the focus lies on the ‘near field’ dynamics and the two-phase flow character at the interface of an immiscible surfactant droplet and a thin sub-phase film. Evidence is provided that, in the case of immiscible surfactant droplets, the fingering instability^{16,17,45,46,49,64,92,93,142,143} is preceded by the temporary trapping of sub-phase liquid and subsequent release from underneath the surfactant droplet, which, as will be shown, induces a pronounced increase of the observed far-field spreading rate. Using fluorescence microscopy an oscillatory instability of the three-phase contact line was investigated during this sub-phase expulsion process, which advances in two distinct stages. In an initial ‘global’ phase, liquid is

expelled in a concerted fashion around a large fraction of the perimeter of the surfactant droplet. In a second ‘local’ stage, the expulsion proceeds primarily in one or few distinct locations breaking the approximate azimuthal isotropy of the initial stage. While the general dynamic behavior of this ‘global’ phase is reminiscent of the instability described by Stocker and Bush¹³⁷, there are distinct differences: such as the independence of evaporative depletion of the surfactant, or the much lower thickness of the sub-phase films of higher viscosity.

2.1 Setup

Oleic acid is practically insoluble in glycerol. Gaver and Grotberg⁵² have measured the relation between surface tension γ and the surfactant surface concentration Γ for this material system.

The measured surface tension γ drops rapidly from the value for the pure sub-phase $\gamma_0 = 63.5 \text{ mN/m}$ and asymptotes into $\gamma_m = 39 \text{ mN/m}$ beyond a concentration $\Gamma_m = 3.5 \mu\text{l/m}^2$. The maximum spreading pressure $\Pi_{\text{max}} \equiv \gamma_0 - \gamma_m$ is therefore determined as 24 mN/m . The continuous line in Fig. 2.1(a) is a fit to the reported experimental data according to the function

$$\gamma = \gamma_m + \Pi_{\text{max}} \exp(-A\Gamma^2) \quad (2.1)$$

with the resulting in a fit parameter $A = 0.5 \text{ m}^4/\mu\text{l}^2$.

Figure 2.2(a) shows a schematic of the experimental system considered in this chapter. At time $t = 0$ a droplet of surfactant (oleic acid, denoted ‘OA’) is deposited on a uniformly flat glycerol film. Since the surface tension of the sub-phase covered with surfactant ($\gamma(\Gamma > 0)$) is lower than $\gamma(\Gamma = 0)$, Marangoni stresses [indicated by the arrows in Fig. 2.2(b)] are induced. These stresses induce flow of the sub-phase liquid from the vicinity of the surfactant droplet outward. The dynamics following the deposition

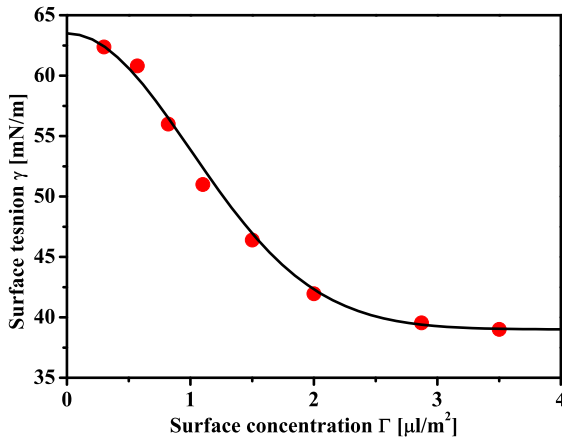
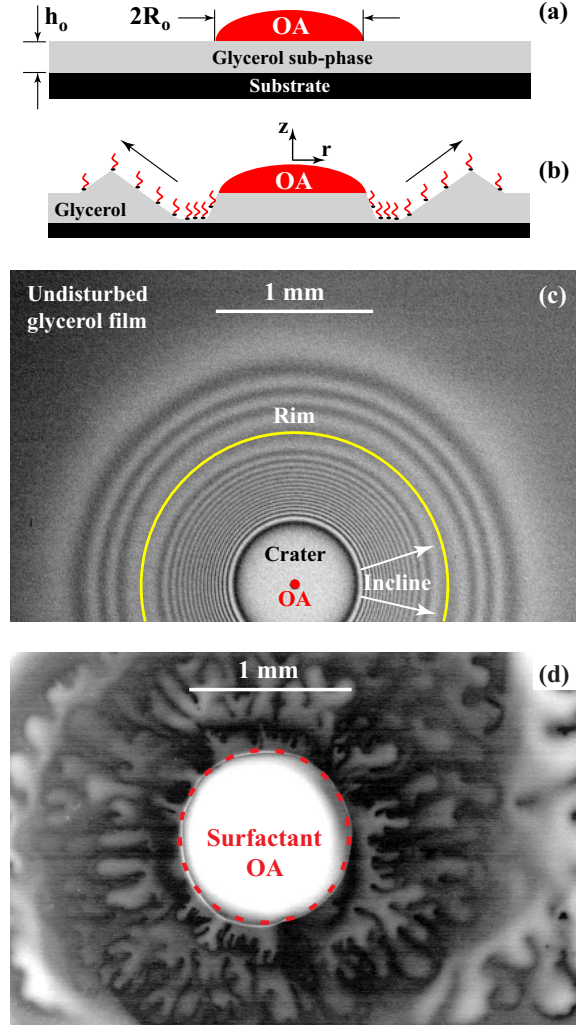


Figure 2.1: Surface tension data for the immiscible surfactant oleic acid on glycerol as measured by Gaver and Grotberg⁵². Their experimental data is given by the red circles, a fit of the form $\gamma = \gamma_m + \Pi_{\text{max}} \exp(-A\Gamma^2)$ with the resulting parameters $A = 0.5 \text{ m}^4/\mu\text{l}^2$, $\Gamma_m = 3.5 \mu\text{l/m}^2$ and $\gamma_m = 39 \text{ mN/m}$ is shown by the black line.

Figure 2.2: (a) At time $t = 0$ a surfactant droplet ('A') of radius R_0 is deposited on a flat and uniform film of liquid (labeled 'sub-phase B') of thickness h_0 and higher surface tension γ_0 . (b) Due to the surface tension imbalance, Marangoni stresses at the liquid-air interface drive the sub-phase film radially outward, which promotes the spreading of a surfactant monolayer. (c) Top-view optical interference micrograph of an oleic acid droplet ($R_0 \approx 80 \mu\text{m}$) 163 s after deposition on a film of glycerol. Image width 3.6 mm. (d) Fluorescence microscopy image of a glycerol film ($h_0 = 70 \mu\text{m}$) containing fluorescein 12.5 s after deposition of an oleic acid droplet. The image (width 3.48 mm) was recorded through a transparent glass substrate and contrast-enhanced.



are elucidated using two types of experiments. The first type is an investigation of the 'far-field' deformation and displacement of the sub-phase liquid following the surfactant deposition using highly reflective Si substrates and interference microscopy. The second is a study of the 'near-field' sub-phase dynamics underneath and in the immediate vicinity of the deposited surfactant droplet. For these experiments transparent glass substrates and fluorescence microscopy were used. All experiments were conducted at room temperature $T \approx 20^\circ\text{C}$ under ambient conditions. Details of the two experimental configurations are described in the following two subsections.

2.1.1 Interference microscopy studies of the sub-phase displacement

Anhydrous glycerol (Fluka, >99.5% purity) films with a thickness between 0.2 and 10 μm were deposited on Si wafers with a diameter of 4 inches by means of spin-coating, which ensures a flat and uniform height profile of the films. The wafers were cleaned by rinsing with trichloroethylene, acetone and isopropanol as well as immersion in a mixture of hydrogen peroxide and sulfuric acid at a temperature of 75°C prior to the experiments. Oleic acid (Fluka, 99% purity, product number 75090) was used as a surface active material, insoluble in glycerol.

After spin-coating, small droplets of surfactant were deposited on the liquid films by using either a piece of Al wire with diameter of 300 μm as a dip-pen or a Micro-drop droplet-on-demand inkjet system with a capillary nozzle diameter of 70 μm . The droplet volumes ranged from 0.2 to 100 nl. The time evolution of the sub-phase surface profiles was measured by interference microscopy with an upright Zeiss AxiotechVario microscope and a bandpass filter centered around a wavelength $\lambda = 645 \text{ nm}$. A typical snapshot is shown in Fig. 2.2(c).

2.1.2 Fluorescence microscopy studies of sub-phase expulsion dynamics

For the second type of experiments rectangular borosilicate glass microscope cover slides (Gold Seal, product number 3334) with dimensions of 48 mm \times 60 mm and thickness between 0.13-0.17 mm, were used as substrates. Prior to deposition of the sub-phase liquid in each experiment, the substrates were repeatedly cleaned using a solution of hydrogen peroxide (30%, J.T. Baker, product number 7047) and sulfuric acid (95%, J.T. Baker, product number 6057), with a volume ratio of 1:1, and subsequently by use of an ozone cleaner. After the cleaning procedure, liquid films of anhydrous glycerol (purity 99%, Sigma Aldrich, product number 49767) containing 0.5 wt% of fluorescein sodium salt (Sigma Aldrich, product number 46960) were deposited via spin coating on the substrates. Tensiometric measurements using a Wilhelmy plate showed no detectable change in surface tension due to the addition of fluorescein. The deposited films had a thickness of $h_0 = (70 \pm 2.5) \mu\text{m}$.

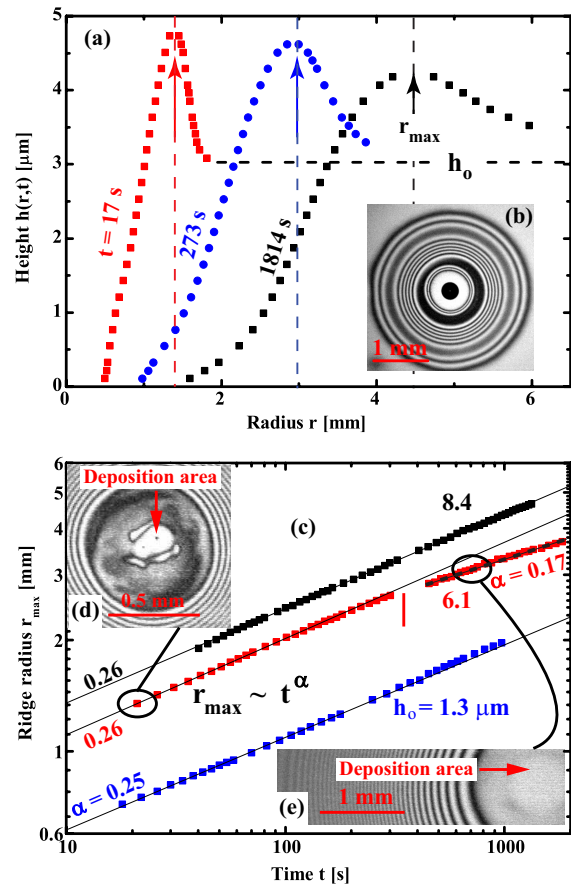
Following deposition of the sub-phase liquid, small quantities of the insoluble surfactant oleic acid (cis-9-octadecenoic acid, purity 99%, Sigma Aldrich, product number O1008) were deposited in the center of the substrates using a Hamilton 7000.5SN micro-syringe as a dip-pen. The dynamics following the surfactant deposition were then monitored by means of fluorescence microscopy using an Olympus IX71 inverted microscope. The samples were illuminated using a Thorlabs LED light source (product number M455L2-C1) and an Olympus U-MGF-PHQ fluorescence filter cube. The recorded grayscale values corresponded to fluorescence intensity, which increases with sub-phase film thickness.

2.2 Results

2.2.1 Stable surfactant spreading dynamics

Figure 2.2(c) shows the surface profile of a glycerol film after deposition of a small droplet of oleic acid (labeled ‘OA’, $R_0 \approx 80 \mu\text{m}$). The light and dark concentric rings are due to optical interference of the light reflected from the Si wafer and the glycerol-air interface. They trace contour lines of equal thickness, where consecutive dark or light fringes correspond to a vertical spacing $\Delta z = \lambda/2n_B \approx 219 \text{ nm}$. In the immediate vicinity of the surfactant droplet, which is marked ‘crater’ region in Fig. 2.2(c), the glycerol film is strongly thinned to a thickness below 50 nm . At larger radial distances the height profile increases in a ramp-like fashion [labeled ‘incline’ in Fig. 2.2(c)] and peaks in a rim. Beyond this rim, the film thickness decreases and asymptotes into the undisturbed sub-phase film thickness h_0 . No detectable instability occurred in the experiment with a very small droplet of oleic acid and a small sub-phase thickness depicted in Fig. 2.2(c).

Figure 2.3: (a) Measured height profiles $h(r, t)$ for oleic acid spreading on a $3 \mu\text{m}$ thin glycerol layer at times $t = 17, 273$ and 1814 s . (b) Optical micrograph of oleic acid spreading on glycerol at $t = 106 \text{ s}$. Image width 3.05 mm . (c) Time dependence of the rim radius $r_{\text{max}}(t)$ for three different values of h_0 ($1.3, 6.1$ and $8.4 \mu\text{m}$). The straight lines correspond to power law relations $r_{\text{max}} \sim t^\alpha$. (d) Optical micrograph of the deposition area for the second data set in (c) (red squares) short after deposition ($t = 21 \text{ s}$), the deposited droplet depleted in the course of the experiment causing a reduction in the observed spreading exponent. (e) Optical micrograph of the deposition area and propagating rim for the same data set after droplet depletion ($t = 812 \text{ s}$). In both images (d) and (e) the deposition area is marked by the red arrows.



When a larger oleic acid droplet with a diameter of about $2R_0 = 1.04$ mm was deposited on a thicker glycerol film ($h_0 = 70 \pm 2.5$ μm), a pronounced finger formation around the surfactant droplet was evident [Fig. 2.2(d)]. The unstable flow is due to the release of sub-phase liquid initially located beneath the droplet. The qualitative difference in the observed dynamics can be attributed to two factors: 1) the difference in the amount of sub-phase liquid initially located beneath the droplet and 2) the increased capillary pressure exerted by a smaller droplet onto the underlying film.

Figure 2.3 presents experimental results for oleic acid spreading on thin films of glycerol. In Fig. 2.3(b), a snapshot of the spreading process is shown. The black dot in the center is the oleic acid droplet, which maintains a finite contact angle and hence does not spread except immediately after deposition. The white ring around the oleic acid is a strongly thinned region, which merges into the incline characterized by the concentric optical interference fringes. In contrast to other references, film rupture or dewetting phenomena around the surfactant droplet were never observed^{52,73}.

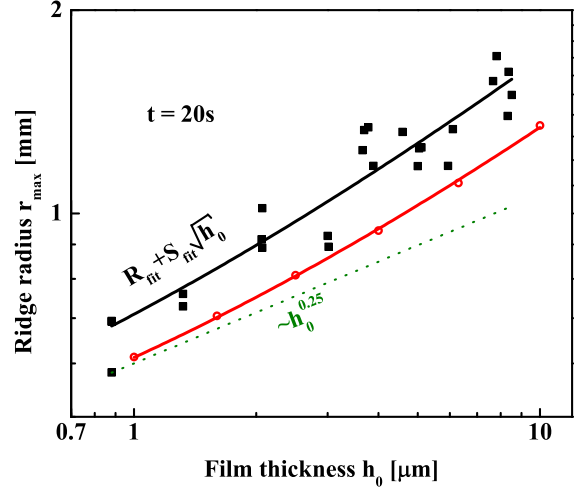
Figure 2.3(a) shows height profiles extracted from the location of the interference fringes at different times during an experiment. The vertical arrows in Fig. 2.3(a) label the radial position of the rim maximum r_{max} . The peak height h_{max} of the advancing rim at early times is about 60% higher than the asymptotic film thickness h_0 . The rim height markedly decreases and the rim width increases with time.

In Fig. 2.3(c), the rim position r_{max} is plotted as a function of time for three different values of h_0 (1.3, 6.1 and 8.4 μm). To good approximation, the rim position exhibits power law behavior $r_{\text{max}}(t) \sim t^\alpha$ with exponents around $\alpha = 0.25$. The second curve ($h_0 = 6.1$ μm) corresponds to an experiment where the deposited droplet of oleic acid was depleted after about 300 s, as indicated by the vertical line. From that moment on, the deposited oleic acid droplet was completely redistributed into a monolayer spreading on the glycerol film. As a consequence, the concentration around $r = 0$ was no longer constant and the effective spreading exponent decreased, indicating the transition from an effectively infinite to a finite surfactant volume. The spreading following the depletion can be approximated by a power law relation with an exponent of $\alpha = 0.17$, indicated by the dashed black line. Figure 2.3(d) and (e) are interference images of the deposition area before and after surfactant depletion, respectively. The original position of the small oleic acid droplet is marked in both images by the red arrows.

The data presented in Fig. 2.3(c) are somewhat misleading inasmuch as a rather wide range of spreading exponents α between about 0.23 and 0.4 has been measured, which will be elucidated in Section 2.2.2. Experiments performed not immediately after spin-coating showed a systematic decrease of α by about 4 – 8% per hour as well as a reduction in the rim height h_{max} .

Figure 2.4 presents the dependence of $r_{\text{max}}(t = 20$ s) on the initial film thickness h_0 . The scatter in the experimental data (black squares) is mainly due to variations in the surfactant droplet radius R_0 . A scaling argument for the dependence of r_{max} on h_0 follows from equating the rim propagation rate with the Marangoni velocity in the region

Figure 2.4: Rim position $r_{\max}(t = 20 \text{ s})$ as a function of h_0 . Experimentally and numerically (Myroslava Hanyak¹³³) obtained values are shown by black squares and red circles respectively. The black and red solid lines correspond to the function $r_{\max}(t = 20 \text{ s}) = R_{\text{fit}} + S_{\text{fit}}\sqrt{h_0}$ with fit parameters R_{fit} and S_{fit} . The green dotted line corresponds to a power law relation $r_{\max}(t = 20 \text{ s}) \sim h_0^{0.25}$ added for orientation.



beyond the crater area, $r > R_c$, where the film thickness is of order h_0

$$\frac{dr_{\max}}{dt} \approx \frac{h_0 \Delta\gamma_{\text{rim}}(t)}{\mu(r_{\max} - R_c)} \rightarrow r_{\max}(t) \approx R_c + S h_0^{1/2}. \quad (2.2)$$

Here, it is assumed that the expansion rate of the crater dR_c/dt is much smaller than the rim propagation rate dr_{\max}/dt . In this context, $\Delta\gamma_{\text{rim}} \equiv \gamma(r_{\max}) - \gamma(R_c)$ is the (time-dependent) surface tension difference between the edge of the crater and the rim position. The function S , which stems from the time-integration of $\Delta\gamma_{\text{rim}}/\mu$ and is, thus, influenced by the film evolution in the crater region, determines the spreading exponent α .

The open symbols in Fig. 2.4 correspond to the results of numerical simulations by Myroslava Hanyak¹³³. The solid lines correspond to the function $r_{\max} = R_{\text{fit}} + S_{\text{fit}}\sqrt{h_0}$ with fit-parameters R_{fit} and S_{fit} . For comparison, the dotted line corresponds to a power-law $r_{\max} \sim h_0^{0.25}$, shown for orientation. Both the experimental and the numerical data are very well approximated by the scaling relation Eq. (2.2) with $R_{\text{fit}} = 255 \mu\text{m}$, but slightly different prefactors S_{fit} . This difference can most likely be attributed to the fact that the numerical simulations were based on the nominal viscosity of pure, anhydrous glycerol, whereas the viscosity in the experiments can be expected to be decreased due to water uptake from the humidity of the ambient atmosphere.

2.2.2 Instability during immiscible surfactant spreading

A well-known fingering instability frequently occurs during the spreading of surfactant solutions on thin liquid films^{4–6,17,29,44–46,49,51,52,57,58,64,73,142,143,149}.

Darhuber et al.²⁹ observed that the front of the spreading surfactant droplet first steepens and develops a rim, which divides into fingers with an initially well defined

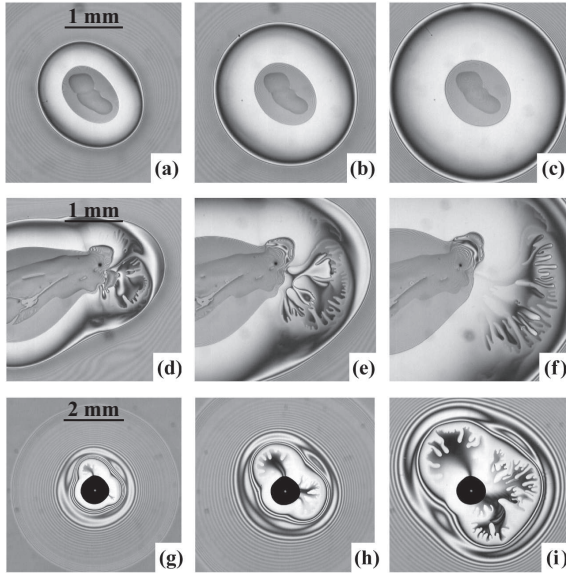


Figure 2.5: (a-c) Stable spreading of PDMS on PPTMTS. Images recorded (a) 65 s, (b) 165 s and (c) 325 s after droplet deposition. Image width 3.0 mm. (d-f) Unstable spreading of PDMS on PPTMTS. Images recorded (d) 74 s, (e) 254 s and (f) 664 s after droplet deposition. Image width 3.0 mm. (g-i) Unstable spreading of oleic acid on glycerol. Images recorded (g) 32 s, (h) 82 s and (i) 182 s after droplet deposition. Image width 5.8 mm.

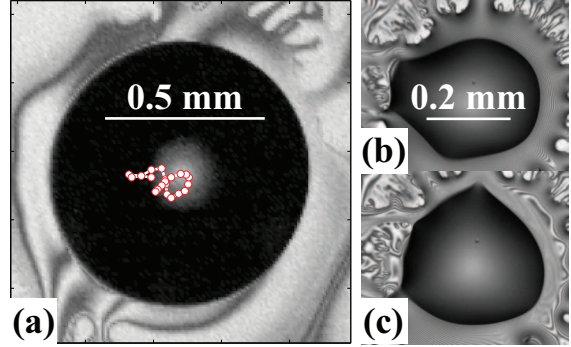
wavelength. These fingers undergo tip-splitting, which is the onset for the formation of a rather irregular morphology including branches and multiple unstable spreading fronts.

If the sub-phase and surfactant are not or only sparingly miscible, the interface between the surfactant droplet and the thin liquid film underneath has to be taken into account. Two material systems are considered here 1) oleic acid, which maintains a finite contact angle on the sub-phase glycerol and 2) PDMS (Polydimethylsiloxane) on PPTMTS (pentaphenyltrimethyltrisiloxane, Dow Corning), which wets the sub-phase completely. Both subphases completely wet the solid substrates used in the experiments. If the surface-active liquid spreads on the sub-phase film as in the case of PDMS on PPTMTS, a volume of sub-phase material becomes essentially permanently trapped underneath the spreading surfactant droplet. This phenomenon is clearly visible in Figs. 2.5(a-c) due to the large difference in the refractive indices of PDMS and PPTMTS, of $n_D^{20} = 1.404$ and 1.578 respectively. The PDMS surrounds the trapped PPTMTS volume around its entire perimeter and the spreading process is completely stable.

Figures 2.5(d-f) show unstable spreading of PDMS on PPTMTS. During deposition of the PDMS droplet the dispensing wire was moved laterally by a fraction of a mm, locally exposing the underlying PPTMTS. A finger of sub-phase liquid formed and subsequently tip split into a complex pattern. When the spreading of the PDMS droplet cut off the supply of PPTMTS, the branching stopped and the fingers gradually thinned, widened and vanished.

In contrast to PDMS, which appears to completely wet PPTMTS, oleic acid is partially wetting and maintains a finite contact angle on glycerol. Using a holographic

Figure 2.6: (a) Oleic acid droplet deposited on a thin film of glycerol. The white circles, corresponding to time differences of 8 s, denote the trajectory of the center of the surfactant droplet. (b,c) Spontaneous shape deformation of an oleic acid droplet on a thicker film of glycerol ($h_0 = 30 \mu\text{m}$). Illuminating light is passband limited around $\lambda = 550 \text{ nm}$. Time difference between frames (b) and (c) 0.1 s.



interferometer the morphology of oleic acid droplets was determined for varying sizes below the capillary length on thin films of glycerol. The glycerol films were deposited on borosilicate glass microscope cover slides, such that the considered configuration is equivalent to the one shown in Fig. 2.2 (b), (c) and Fig. 2.6 (a). The liquid-air interface of the droplets was found to maintain the shape of a spherical cap with an effective contact angle of $\theta \approx 9.5 \pm 0.5^\circ$.

An analogous instability to the one described for PDMS on PPTMTS is observed primarily for large surfactant droplets and thick sub-phase films, where glycerol trapped beneath the oleic acid is driven forward and develops fingers that subsequently tip-split and branch out [see Fig. 2.5(g-i)]. Due to the finite contact angle, the material supply is not cut off by the spreading of the surfactant droplet and the fingers continue to evolve until the trapped sub-phase material is depleted.

On thin sub-phase films ($h_0 < 10 \mu\text{m}$) the expulsion often does not affect the entire perimeter of the surfactant droplet [Fig. 2.5(g-i)], whereas on thicker films an initial stage of expulsion along the entire droplet perimeter is observed [Figs. 2.2(d) and 2.6(b,c)]. In both cases, axisymmetry is not maintained. A net force acting on the surfactant droplet results, which can induce shape deformations and swaying. Figure 2.6 shows the trajectory of the center of a droplet of oleic acid on a thin film of glycerol. After the trapped glycerol is depleted, the jiggling motion stops and the droplet perimeter assumes a circular shape.

2.2.3 Expulsion induced modification of the spreading dynamics

Besides undulating the drop contact line and position, sub-phase expulsion can have a strong effect on the spreading dynamics of the surfactant, as illustrated in Fig. 2.7(a). The ridge position r_{max} as a function of time, influenced by pronounced sub-phase expulsion at a certain time during the experiment, is shown. Two stages of spreading can be clearly identified. Initially ($t < 150 \text{ s}$) the ridge radius increases as $r_{\text{max}} \sim t^{0.26}$ (indicated by the fitted black solid line) while for later times ($t > 150 \text{ s}$) the increase can be

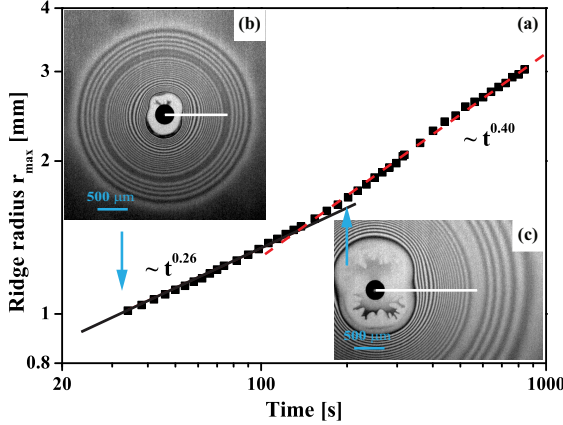


Figure 2.7: (a) Experimentally monitored rim position $r_{\max}(t)$ for $h_0 = 2.9 \mu\text{m}$, exhibiting two distinct spreading stages due to sub-phase expulsion. Initially the ridge radius follows $r_{\max} \sim t^{0.26}$ (black solid line), for later times ($t > 150 \text{ s}$) $r_{\max} \sim t^{0.40}$ holds (red dashed line). (b,c) Microscope images of the (b) initial ($t = 34 \text{ s}$) and (c) later ($t = 194 \text{ s}$) stage. (c) Expelled liquid is clearly visible and undergoes a fingering instability. Solid white lines indicate the position at which the ridge radius is measured, blue arrows mark the data points corresponding to the images.

approximated by $r_{\max} \sim t^{0.40}$ (indicated by the fitted red dashed line). Figures 2.7(b,c) show microscope images of the early and late stage respectively.

In Fig. 2.7(b) only a very small and localized amount of expelled sub-phase liquid is visible. While in Fig. 2.7(c) the expelled liquid is clearly visible and covers most of the crater region around the surfactant droplet. The expelled liquid in the crater region enhances the transport of surfactant from the droplet to the rim and causes the increase in the spreading rate in Fig. 2.7(a) at around $t = 150 \text{ s}$.

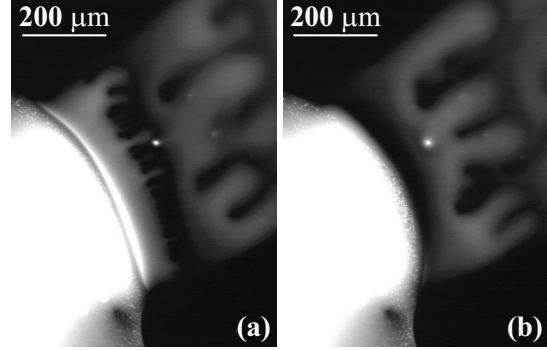
The experiment shown in Fig. 2.7 exhibits two distinct spreading phases due to delayed sub-phase expulsion. Other experiments exhibited expulsion directly after deposition which resulted in an overall increased exponent, as mentioned in section 2.2.1, rather than two distinct phases of spreading with different exponents.

2.2.4 Sub-phase expulsion dynamics near the three-phase contact line

In the experiments reported in the previous sections, rather thin films ($h_0 < 10 \mu\text{m}$) were used; the expulsion of sub-phase liquid and the associated occurrence of the fingering instability was observed only occasionally. For thicker films with $h_0 \approx 70 \mu\text{m}$, sub-phase expulsion and flow instabilities were always prominent. The expulsion process in these experiments can be divided into two stages. In the first stage the expulsion occurs in a concerted fashion along a large fraction of the perimeter of the surfactant droplet. This ‘global’ expulsion is associated with a discernible motion of the three-phase contact line of the droplet. Figure 2.2(d) shows a fluorescence microscopy image of the global expulsion stage.

The ‘global’ expulsion phase appears to be reminiscent of the spontaneous oscil-

Figure 2.8: Fluorescence microscopy images of a localized expulsion process (image width $632 \mu\text{m}$). The three-phase contact line of the surfactant droplet oscillates forward and backward in the radial direction. (a) Contact line in its most retracted and (b) in its extended position.



latory deformation of a sessile oil lens containing a volatile surfactant on an aqueous subphase, which has recently been studied by Stocker and Bush¹³⁷. In their system, however, the sub-phase layer thicknesses were approximately 100-1000 times larger, the sub-phase viscosity was three orders of magnitude smaller than for the system considered here and evaporation of the surfactant was a prerequisite for the occurrence of the oscillations. The material system, oleic acid and glycerol, can be considered nonvolatile at the experimental conditions described above.

In the second or late stage, the expulsion occurs in a localized fashion at one or a few positions around the perimeter. An example is shown in Fig. 2.8, which also illustrates the associated oscillatory deformation of the three-phase contact line of the surfactant droplet. Videos of both processes are provided as supplementary information in Ref.¹³³. In both stages, the spreading of the expelled liquid is unstable and undergoes a fingering instability.

2.2.5 Global expulsion

Due to the expulsion of liquid located under the surfactant droplet, the corresponding fluorescence intensity decreases as time progresses. During the stage of global expulsion, the rate of this decrease depends on the size of the deposited surfactant droplet. This is illustrated in Fig. 2.9(a), where the temporal evolution of the fluorescence intensity $I(t)$ in the center of various deposited surfactant droplets is shown. In each experiment, the fluorescence intensity $I(x, y, t)$ was integrated over a circular region with diameter equal to the droplet radius ($r \leq \frac{1}{2}R_0$)

$$I(t) = \int_{-R_0/2}^{R_0/2} \int_{-\sqrt{R_0^2/4-x^2}}^{\sqrt{R_0^2/4-x^2}} I(x, y, t) dy dx . \quad (2.3)$$

The droplets in the experiments presented in Fig. 2.9(a) had diameters of $2R_0 = 0.88 \text{ mm}$ (red triangles), 2.17 mm (blue circles) and 3.76 mm (black squares). It is evident that the rate of the intensity decrease is higher for the smaller droplets. At the end of the global expulsion phase $t = \Delta t$, the concerted motion of the 3-phase contact line

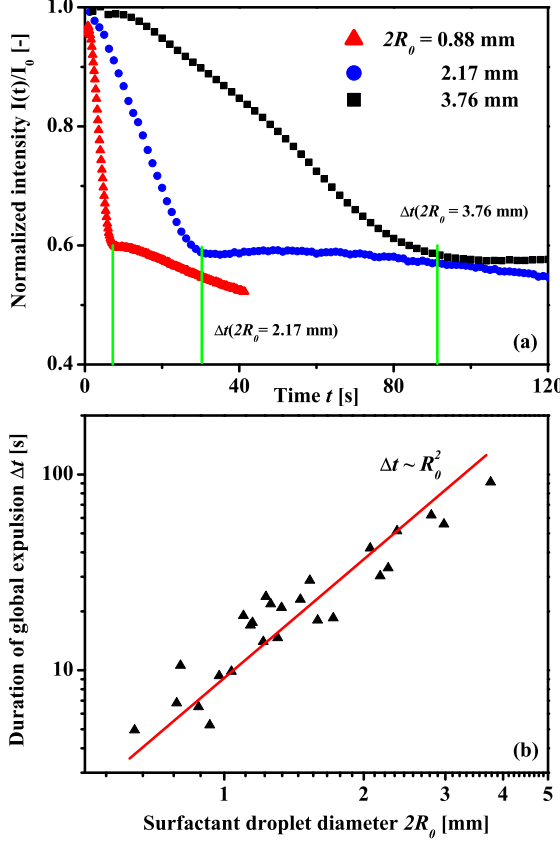


Figure 2.9: (a) Temporal evolution of the fluorescence intensity integrated over the region $r \leq 0.5R_0$ underneath the deposited surfactant droplet for $2R_0 = 0.88$ mm (red triangles), 2.17 mm (blue circles) and 3.76 mm (black squares). Vertical lines indicate the end of the global expulsion phase. (b) Duration of the global expulsion stage Δt as a function of surfactant droplet radius R_0 as determined by image analysis. The solid line corresponds to the scaling relation $\Delta t \sim R_0^2$.

ceases and the rate of decrease of the integrated fluorescence intensity is reduced as indicated by the green vertical lines. Figure 2.9(b) shows the dependence of Δt on the radius R_0 of the deposited surfactant droplet. The straight line corresponds to the scaling relation $\Delta t \sim R_0^2$, which can be derived by considering the volume of sub-phase liquid expelled in the global stage V_{gl} . Let δ be the fraction $\delta \equiv V_{gl}/V_0$ relative to the quantity initially trapped under the droplet and in an analogous way δ_I the ratio of the integrated intensity prior to and following the global expulsion stage $\delta_I \equiv I(\Delta t)/I(0)$. Figure 2.9(a) indicates that $\delta_I \approx 0.4$ is to first approximation independent of the droplet radius R_0 . The initial film height h_0 was kept constant in the experiments. Moreover, the film profiles underneath the droplet to good approximation exhibited geometrical similarity in the integration region with respect to different R_0 . Considering these two factors, it can be concluded that $\delta \equiv V_{gl}/V_0$, i.e. the fraction of expelled sub-phase liquid, is essentially independent of R_0 . In the following a scaling argument that is in qualitative agreement with the experimentally observed behavior will be outlined. A no-slip boundary condition holds at the solid-liquid interface $z = 0$ and no stress at the subphase/droplet interface, i.e. $\mu \partial v_r / \partial z|_{z=h} \approx 0$, which is admissible owing to the

large ratio of sub-phase and drop viscosity $\mu/\mu_{\text{drop}} \gg 1$. The flow velocity in radial direction then follows as $v_r = -\frac{\partial p}{\partial r} z(2h - z)/2\mu$. Assuming axisymmetry, the rate of volume loss of sub-phase liquid \dot{V} is given by

$$\dot{V} = \int_0^h \int_0^{2\pi} v_r R_0 d\varphi dz = -\frac{2\pi R_0 h^3}{3\mu} \frac{\partial p}{\partial r} \Big|_{r=R_0} \quad (2.4)$$

Integrating the volume flux \dot{V} over the duration of the global expulsion stage Δt yields the scaling relation for the expelled volume

$$V_{gl} = \delta\pi R_0^2 h_0 = \int_0^{\Delta t} \dot{V} dt \sim \frac{2\pi h_0^3}{3\mu} R_0 \frac{\partial p}{\partial r} \Delta t. \quad (2.5)$$

The expulsion duration Δt scales therefore as

$$\Delta t \frac{3\mu}{2\pi h_0^3 R_0 \frac{\partial p}{\partial r}} \delta V_0 = \frac{3\mu}{2\pi h_0^3 R_0 \frac{\partial p}{\partial r}} \delta\pi R_0^2 h_0. \quad (2.6)$$

Sub-phase liquid underneath the surfactant droplet is subject to the capillary pressure of the surfactant droplet, since the curvature of the liquid-liquid interface is negligible compared to the curvature of the liquid-air interface for thin sub-phase films $h_0 \ll R_0$. For small $R_0 < \ell_c$ this pressure is large compared to hydrostatic pressure contributions. Assuming that the relevant length scale for the pressure gradient at the 3-phase contact line of the droplet is independent of the droplet diameter $2R_0$, it scales as $\frac{\partial p}{\partial r} \sim \frac{\gamma_{\text{OA}}}{R_0}$, with γ_{OA} denoting the liquid-air interfacial tension of the deposited droplet. If - consistent with the experimental finding in Fig. 2.9(a) - also δ is presumed independent of R_0 , then the scaling $\Delta t \sim R_0^2$ results, which agrees well with the experimental data shown in Fig. 2.9(b).

2.2.6 Local expulsion

In the later stages of the experiments, localized expulsion phenomena are frequently observed, where liquid is visibly expelled from underneath the surfactant droplet only at a certain position along the droplet perimeter. This localized expulsion is associated with an oscillatory deformation of the droplet three-phase contact line as shown in the fluorescence microscopy images in Fig. 2.8. The conformation of the contact line in its most retracted position is shown in Fig. 2.8(a) and in 2.8(b) for its most extended state.

Figure 2.10(a) shows a fluorescence microscopy image of a local expulsion zone. The rectangle with length $100 \mu\text{m}$ indicates the zone over which the intensity was averaged over 10 pixels normal to the ξ -direction as well as the zero position of the ξ -axis. The averaged fluorescence intensity $\langle I \rangle(\xi, t)$ is presented in Fig. 2.10(b). Each profile has been normalized with the saturation intensity of the camera and progressively shifted along the ordinate axis by a constant amount for clarity. The local maxima in the $\langle I \rangle(\xi, t)$ profiles, approximately in the range $\xi = 80\text{-}100 \mu\text{m}$, are caused by emulsion droplets

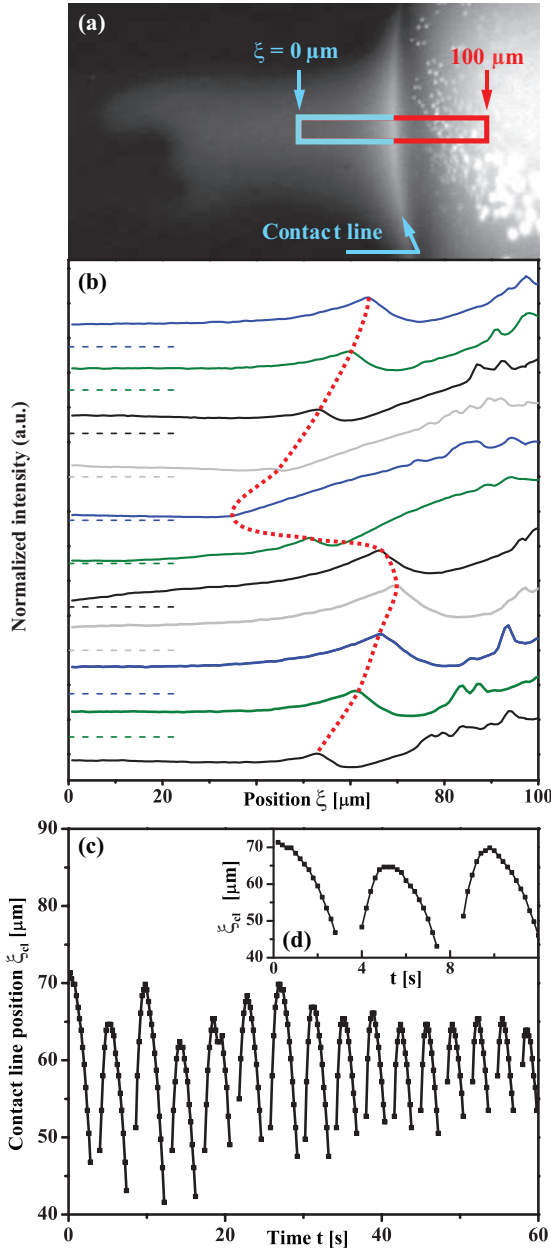


Figure 2.10: (a) Fluorescence microscopy image of a local expulsion zone. The rectangle (length $100 \mu\text{m}$) indicates the position $\xi = 0$ and the region over which the intensity was integrated normal to the ξ -direction. (b) Averaged fluorescence intensity $\langle I \rangle(\xi)$ measured perpendicular to the droplet contact line. Individual lines, corresponding to time increments of 0.6 s , are shifted vertically for clarity. The dashed lines represent the baselines ($\langle I \rangle = 0$) for each curve of the plotted curves. The dotted red line traces the local intensity maxima that is interpreted as the location of the three-phase contact line. (c) Contact line position ξ_{cl} plotted as a function of time illustrating its continued oscillatory motion. (d) Zoom of (c) emphasizing the asymmetry in the speed of the advancing and receding contact line motion.

inside the drop of oleic acid. The dotted red line traces a pronounced sequence of local maxima in $\langle I \rangle(\xi, t)$, as illustrated by the lightblue arrow in Fig. 2.10(a). They can be ascribed to a meniscus of sub-phase liquid forming at the position of the three-phase contact line ξ_{cl} .

Figures 2.10(c,d) show that ξ_{cl} undergoes an oscillatory motion, where the retraction

phase occurs much faster than the extension phase, as evident from the asymmetric peak shapes in Fig. 2.10(d). The gaps between the individual parts of the curve correspond to times in which no distinct maximum is detectable. The receding motion [positive slope in Fig. 2.10(c,d)] was consistently observed to be faster than the advancing motion [negative slope in Fig. 2.10(c,d)].

2.3 Summary

In this chapter the spreading dynamics of effectively immiscible, surface-active liquids on thin liquid films was investigated. Fluorescence microscopy and optical interferometry were applied to monitor the sub-phase morphology in the vicinity and far from the deposited surfactant droplet. A fingering instability was observed similar in appearance to the case of soluble surfactants, which is induced by the temporary entrapment of sub-phase liquid beneath the deposited surfactant droplet and its subsequent release. Two distinct phases of this expulsion process were identified: a ‘global’ regime that was observed primarily for thicker films and early times after surfactant deposition, where sub-phase liquid is expelled along most of the three-phase contact line. The global was followed by a ‘local’ expulsion stage, where flow of sub-phase liquid is restricted to one or few locations along the droplet perimeter. Furthermore, a pronounced oscillatory instability of the three-phase contact line, which temporally modulates the sub-phase flow, was described.

Note: It is acknowledged that the interferometric experiments in Fig. 2.3, 2.5, 2.6 a) and 2.7 were conducted by Anton A. Darhuber.

The results presented in this chapter have been published in combination with numerical work by Myroslava Hanyak: *D. K.N. Sinz, M. Hanyak, and A. A. Darhuber, Immiscible surfactant droplets on thin liquid films: Spreading dynamics, sub-phase expulsion and oscillatory instabilities. Journal of Colloid and Interface Science, Vol. 364 pp. 519 - 529, 2011.*

Chapter 3

Surfactant spreading on a sub-phase rivulet defined by a chemical surface pattern

In the previous chapter the flows induced by the deposition of a droplet of oleic acid on a uniform layer of glycerol were described, i.e. the radially symmetric spreading of an immiscible surfactant over a thin liquid film. Far-field spreading dynamics were shown to be strongly influenced by the conditions at the area of surfactant deposition or source of surfactant. When considering the spreading of surface active agents on the pore scale in an oil reservoir a radially symmetric liquid interface is a poor approximation. The liquid interfaces under reservoir conditions can be expected to be confined physically as well as chemically, i.e. by the rock matrix itself and by varying wettability of the rock surface. This chapter presents the first study regarding surfactant spreading on sub-phase films subjected to a spatial confinement imposed via a chemical surface pattern. The surface patterning results in heterogeneous wettability of the substrates used in the experiments, such that the sub-phase is localized on wettable or high surface energy regions. Confinement of the sub-phase to thin liquid lines, or rivulets, results in a curved liquid-air interface. As will be shown, this curvature gives rise to a transition in the morphology evolution of the sub-phase as the surfactant is spreading along the thin liquid line. Surfactant propagation along the rivulets can, as for the axisymmetric case in chapter 2, be represented by a power law relation $x \approx t^\alpha$. Experimental data for the spreading of an insoluble surfactant will be shown to be in excellent agreement with numerical simulations by Myroslava Hanyak¹³⁴ both with respect to the rate of spreading as well as the evolving morphology of the sub-phase. For a soluble surfactant systematic experimental data will be presented for different deposition procedures corresponding to a stationary as well as a spatially expanding surfactant source area.

First the chemical patterning procedure is outlined, followed by experimental data on the coating of the chemically patterned substrates with a sub-phase solution. Subse-

quently the systematic studies of the spreading of the insoluble surfactant oleic acid and the soluble surfactant sodium dodecyl sulfate are presented.

3.1 Experimental setup

In the following sections the creation of the chemical surface patterns is described, followed by experimental data on the deposition of the sub-phase liquid onto the hydrophilic parts of the patterned substrate.

3.1.1 Chemical patterning

Chemically patterned surfaces were fabricated using self-assembled monolayers of 1H, 1H, 2H, 2H-perfluorooctyl-trichlorosilane (PFOTS, purity > 97%, Sigma Aldrich product number 448931) on single-side polished Si substrates with dimensions of typically 50 mm × 50 mm × 0.7 mm. Self-assembled trichlorosilane monolayers have been studied extensively¹²⁵, in combination with photolithographic masking they can be employed to create surfaces exhibiting heterogeneous wettability³². For the experiments described here substrates were cut from Silicon wafers (n-type doped with Ph) with a diameter of 150 mm obtained from Silicon Quest (batch number SQ13869).

The substrates were cleaned in two steps, first by immersion in a solution of hydrogen peroxide (30%, J.T. Baker product number 7047) and sulfuric acid (95%, J.T. Baker product number 6057), mixed at a volume ratio of 1:1, and subsequently by exposure to an oxygen plasma. The chemical surface patterns were created by photolithography and subsequent vapor deposition of PFOTS in a sealed glass jar at a temperature of 100°C, i.e. the hydrophilic regions were masked with photo-resist and the hydrophobic ones were left unmasked prior to the vapor deposition. This patterning procedure resulted in an advancing contact angle for glycerol between 70° and 90° on the hydrophobic areas with sufficient spatial uniformity and fidelity of the patterned structure. However there exists a vast body of literature dedicated to optimization of the trichlorosilane monolayer formation¹⁴. The hydrophilic patterns, used in the spreading experiments described here, were of rectangular shape with a width of $w \leq 1.5$ mm and a length of $L = 40 - 70$ mm.

3.1.2 Coating of patterned substrates

Following the creation of the patterns, thin films of glycerol were deposited onto the hydrophilic areas via spin-coating, which ensures uniform and reproducible height profiles. Prior to spin-coating the entire substrate is covered with a glycerol film of $\approx 2 - 3$ mm thickness. Due to the rather high contact angle on the hydrophilic parts of the sample, after spinning liquid is only left on the hydrophilic parts of the sample.

A typical interference microscopy image of a coated substrate is shown in Fig. 3.1(b). The width of the chemical pattern and therefore the deposited rivulet of glycerol in this

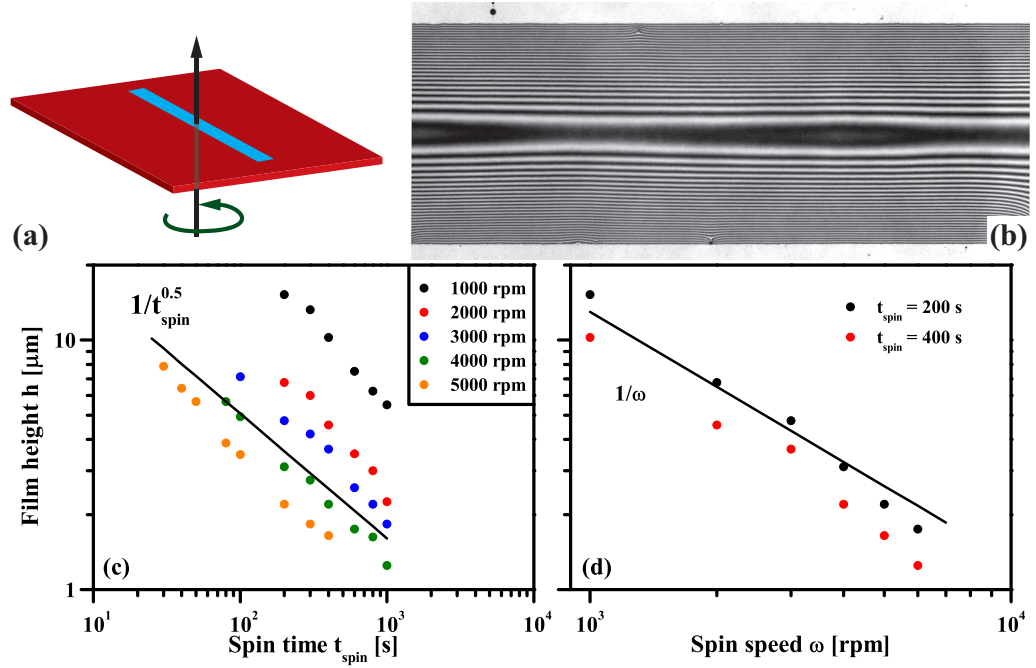


Figure 3.1: (a) Alignment of the chemical surface pattern along the axis of rotation of the spin-coater. (b) Interference microscopy images of a spin-coated rivulet. Rivulet width $w = 1.5$ mm and center height $h_0 = 6.6$ μm . (c) Center film height of spin coated rivulets as a function of the spinning time t_{spin} . (d) Center film height as a function of the spinning speed ω for two different spinning durations t_{spin} .

image is $w = 1.5$ mm. The height profile of the liquid film can be reconstructed from the interference fringes. The center height h_0 in the shown image is $h_0 \approx 6.6$ μm .

Fig. 3.1(c) shows the influence of the spinning time t_{spin} on the resulting center film thickness of coated rivulets. For all measured spinning speeds the centerline film thickness scales as $h_0 \approx t_{spin}^{-0.5}$. Film thicknesses measured for constant spinning times of $t_{spin} = 200$ s and 400 s are shown in Fig. 3.1(d) as a function of spin speed ω . The data suggests a power-law relation $h_0 \sim \omega^{-1}$ for $\omega \leq 4000$ rpm. The confinement induced curvature in the lateral direction of the coated rivulets gives rise to capillary pressure favoring a parabolic shape of the liquid interface. In the longitudinal direction the length of the rivulet is sufficiently large such that for large parts of the rivulet end effects are absent. At the ends of the rivulets this situation changes and flow of liquid in longitudinal direction is hindered by the boundaries of the hydrophilic area. This leads to film height maxima at both ends of the coated rivulets as shown in Fig. 3.2(a) for a rivulet of width $w = 1$ mm.

For high spin-speeds and long coating times another confinement induced effect was observed. For high spin-speeds the measured film heights shown in Fig. 3.1(d) slightly

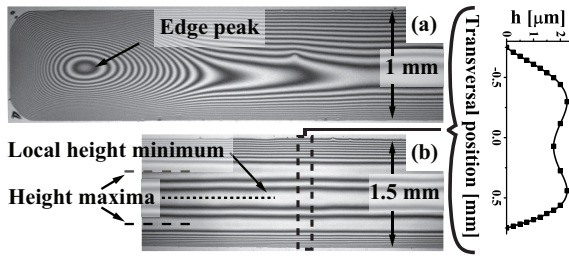


Figure 3.2: (a) The end regions of a spin-coated rivulet exhibit a strongly increased film thickness. (b) Center region of a rivulet coated with 6000 rpm exhibiting a central local minimum in film thickness in between two height maxima as indicated by the dotted and dashed lines, respectively.

deviate from the $\frac{1}{\omega}$ scaling. For these conditions a local film thickness minimum formed along the centerline of the rivulet. A typical rivulet interference pattern for the morphology resulting from these spinning conditions is shown in Fig. 3.2(b), the two film thickness maxima next to the local minimum are indicated by the dashed lines while the dotted line marks the location of the minimum. The reason for this centerline film thinning is that the centrifugal forces acting on the fluid overcome the capillary pressure that acts towards retaining a parabolic height profile. After spinning the rivulet gradually relaxes towards a parabolic height profile, which can be accelerated by heating the sample and thereby strongly reducing the viscosity of the glycerol.

Following the deposition of the sub-phase, the actual surfactant spreading experiments were conducted by localized deposition of small quantities of surfactant onto the confined sub-phase rivulet. Experimental details for an insoluble as well as a soluble surfactant are given below.

3.2 Insoluble surfactant spreading

As in the previous chapter the material combination glycerol/oleic acid was used as a model system to study the spreading of an insoluble surfactant. The dependence of the sub-phase surface tension on the surface concentration was given in Fig.2.1, as determined by Gaver and Grotberg⁵². Typically 0.1 to 0.2 μl of oleic acid (purity 99%, Sigma Aldrich product number O1008, density $\rho_{\text{oleic}} = 0.895 \text{ g/cm}^3$, surface tension $\gamma_{\text{oleic}}(25^\circ\text{C}) = 32.5 \text{ mN/m}$, viscosity $\mu_{\text{oleic}}(25^\circ\text{C}) = 28.2 \text{ mPa}\cdot\text{s}$) were deposited in

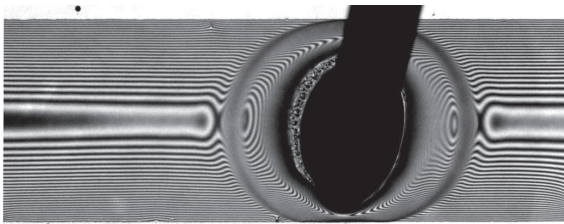


Figure 3.3: Interference microscopy image of a rivulet during deposition of a droplet of insoluble surfactant. Rivulet width $w = 1.5 \text{ mm}$ and center height $h_0 = 6.6 \mu\text{m}$. Rims, forming on both sides of the surfactant source, propagate along the rivulet.

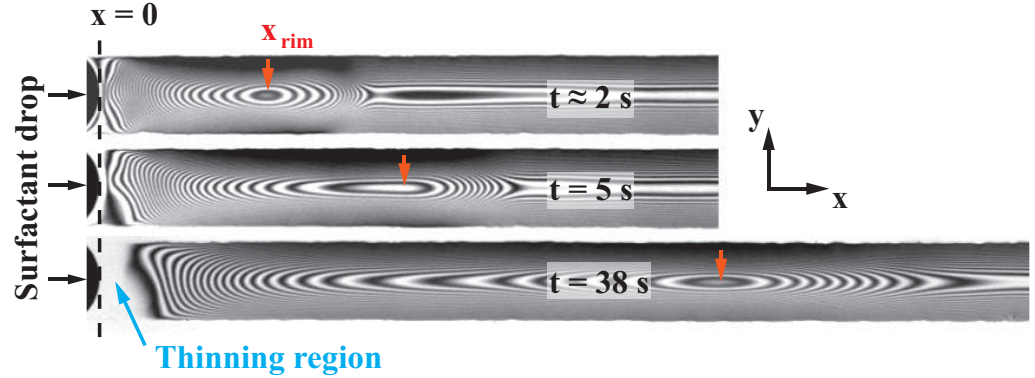


Figure 3.4: (a) Interference microscopy images of rivulet height profiles at different times $t = 2$ s, 5 s and 38 s after surfactant deposition. The black circle segment visible at the left margin of the images is part of the deposited surfactant droplet. The red arrows indicate the rim position. The blue arrow marks the region of strong film thinning adjacent to the surfactant droplet. Rivulet width $w = 0.28$ mm.

the center of the rivulets using a micro-syringe as a dip-pen. A snapshot of this deposition process is shown in Fig. 3.3. The width and center height of the shown rivulet are $w = 1.5$ mm $h_0 = 6.6$ μm , respectively. Rims form on both sides of the surfactant source and subsequently propagate along the rivulet.

The dynamics following the surfactant deposition were monitored by means of interference microscopy using an Olympus BX51 upright microscope. Depending on the sub-phase film height, the illuminating light was passband-limited around a center wavelength of $\lambda = 750$ nm or $\lambda = 550$ nm with a bandpass of $\Delta\lambda \approx 10$ nm. In the case of film heights above $h_0 = 80$ μm the evolution of the rivulet height profile was observed in a side-view configuration using a telecentric lens with a vertical resolution of approximately 5 – 10 μm . All experiments have been performed in a horizontal sample orientation with the liquid deposited on the upper side of the substrates.

Figure 3.4 shows a typical series of interference microscopy images obtained for a rivulet of width $w = 0.28$ mm. The deposition of the surfactant locally reduces the sub-phase surface tension and induces Marangoni stresses that in the case of thin liquid films cause a net flow away from the deposition region. A local maximum in the height profile is visible in Fig. 3.4, which is propagating along the rivulets as marked by the red arrows. The position of this maximum or rim is a measure of the advance of the surfactant monolayer along the rivulet⁵². In the immediate vicinity of the deposited surfactant droplet, a pronounced film thinning is observed in Fig. 3.4. Concluding from the grayscale values of the interference microscopy images, the local film thickness is well below 100 nm. A Cartesian coordinate system is introduced with the x -axis parallel to the rivulet and the z -axis normal to the substrate surface, i.e. opposite to the direction of gravity. The position $x = 0$ corresponds to the edge of the surfactant droplet; $y = 0$

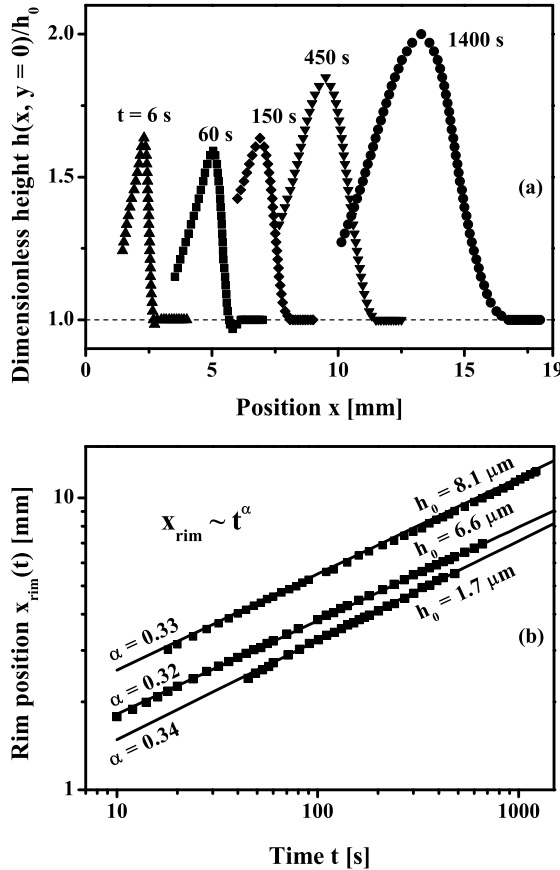


Figure 3.5: (a) Experimentally measured rivulet height profiles $h(x, y = 0, t)$ at different times after the deposition of a surfactant droplet. Rivulet width $w = 1.5$ mm, initial rivulet center film height $h_0 = 8.25 \mu\text{m}$. After an initial plateau-phase the maximum rim height increases from a value of approximately $1.6h_0$ to a value of about $2h_0$. (b) Exemplary measurements of the rim position $x_{\text{rim}}(t)$ as a function of time for various initial film heights and a rivulet width of $w = 1.5$ mm. For all the shown film heights the rim position can be approximated by a power law relation $x_{\text{rim}} \sim t^\alpha$. The solid lines correspond to power law fits with exponents α in the range of $0.32 - 0.34$ apparently independent of the different values of h_0 .

corresponds to the centerline of the rivulet, see Fig. 3.4.

In Fig. 3.5(a) typical centerline height profiles $h(x, y = 0, t)$ are presented for different times after deposition. The profiles were obtained from an analysis of the corresponding interference fringe patterns. The peak height of the rim h_{max} was determined to be approximately $1.6h_0$ at $t = 6$ s. In later stages of the experiment the width of the rim grows and an increase in the peak height to about $2h_0$ is observed. This is in strong contrast to the results obtained for radially symmetric spreading, presented in Fig. 2.3. Here the height of the propagating rim was, after an initial formation period, monotonically decreasing. This is not the case for the spreading on a chemically confined liquid film. The reason for this increase in the height of the propagating rim will be elucidated below. Figure 3.5(b) shows typical measurements of the rim position as a function of time $x_{\text{rim}}(t)$ for various values of h_0 . As for the radially symmetric configuration, the rim propagates faster along thicker rivulets. To very good approximation the experimental data can be represented by a power law relation $x_{\text{rim}} \sim t^\alpha$. The solid lines in Fig. 3.5(b) correspond to power law fits with exponents α in the range of $0.32 - 0.34$ apparently independent of h_0 .

3.2.1 Propagation rate of the surfactant

In Fig. 3.6 fitted exponents for a range of the lateral aspect ratio $\varepsilon = 2h_0/w$ are shown. Experimental results measured on rivulets of width $w = 1.5$ mm and $w = 0.28$ mm are indicated by the black squares and circles, respectively. The smaller rivulet width w allowed the application of interference microscopy for higher aspect ratios since this method is limited to film thicknesses below approximately $10 \mu\text{m}$. The gray dashed line is the average experimental value of $\langle \alpha \rangle = 0.33$. The red downwards facing triangles represent simulation results by Myroslava Hanyak¹³⁴ in excellent agreement with the experimental data. These simulation results are based on an evolution equation for the sub-phase height profile¹¹⁸ that accounts for the influence of Marangoni stresses, hydrostatic and capillary pressure gradients. This equation is combined with an equation for surfactant surface transport including the effects of convection by the liquid surface motion as well as surface diffusion as introduced by Borgas & Grotberg¹¹ and Troian *et al.*¹⁴² The derivation via the small-slope or lubrication approximation is justified for small lateral aspect ratios, i.e. $\varepsilon \equiv 2h_0/w \ll 1$. Using the non-dimensional variables

$$\bar{x} = \frac{2x}{w}, \quad \bar{y} = \frac{2y}{w}, \quad \bar{h} = \frac{h}{h_0} \quad (3.1)$$

$$\bar{\Gamma} = \frac{\Gamma}{\Gamma_0}, \quad \bar{p} = \frac{pw^2}{4h_0\Pi_{\max}}, \quad \bar{t} = t \frac{4h_0\Pi_{\max}}{\mu w^2}, \quad (3.2)$$

the final non-dimensional system of equations as used by Hanyak¹³⁴, given here for the sake of completeness, is

$$\frac{\partial \bar{h}}{\partial \bar{t}} + \bar{\nabla} \left[\frac{1}{2} (\bar{h}^2 \bar{\nabla} \bar{\gamma}) - \frac{\text{Bo}}{3} \bar{h}^3 \bar{\nabla} \bar{h} - \frac{\varepsilon^2}{3} \bar{h}^3 \bar{\nabla} \bar{p} \right] = 0 \quad (3.3)$$

$$\frac{\partial \bar{\Gamma}}{\partial \bar{t}} + \bar{\nabla} \left[\bar{h} \bar{\Gamma} \bar{\nabla} \bar{\gamma} - \frac{\text{Bo}}{2} \bar{h}^2 \bar{\Gamma} \bar{\nabla} \bar{h} - \frac{\varepsilon^2}{2} \bar{h}^2 \bar{\Gamma} \bar{\nabla} \bar{p} - \frac{1}{\text{Pe}_s} \bar{\nabla} \bar{\Gamma} \right] = 0 \quad (3.4)$$

$$\bar{p} = -\bar{\gamma} \bar{\nabla}^2 \bar{h} \quad (3.5)$$

$$\bar{\gamma} = \frac{\gamma_m}{\Pi_{\max}} + \exp(-\bar{A} \bar{\Gamma}^2), \quad (3.6)$$

where $\text{Bo} \equiv \rho g h_0^2 / \Pi_{\max}$ is the Bond number, $\text{Pe}_s \equiv h_0 \Pi_{\max} / (\mu D_s)$ is the surface Peclet number, μ and ρ are the sub-phase viscosity and density, respectively, and D_s is the surfactant surface diffusivity. The second term in Eqs. (3.3,3.4) represents the influence of Marangoni stresses arising from gradients in surface tension $\bar{\gamma}$. The third term in both equations accounts for hydrostatic pressure gradients and the fourth term reflects capillary pressure gradients. The last term in Eq. (3.4) describes surface diffusion along the liquid-air interface. Equation (3.5) corresponds to the Laplace-Young equation. Equation (3.6) is the non-dimensional version of Eq. (2.1).

The initial height profile was assumed to be parabolic, which is justified since the influence of gravity is negligible in the experiments. At the lateral edges of the hydrophilic

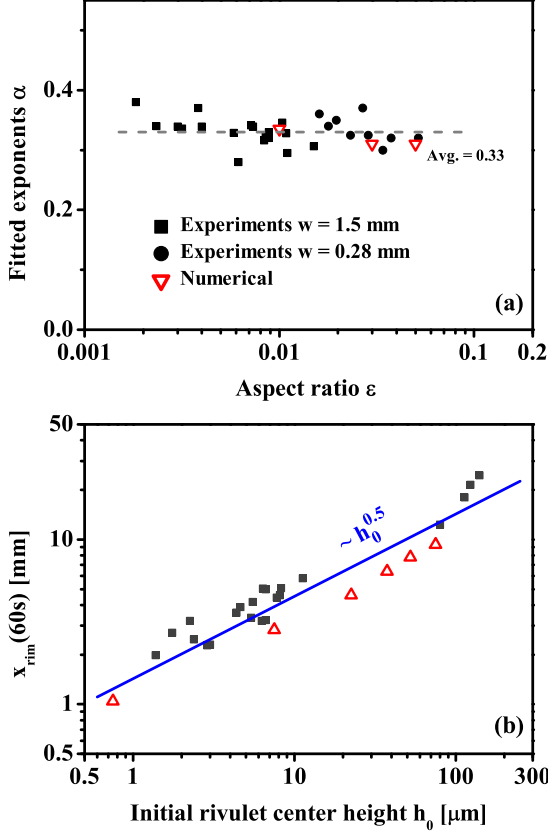


Figure 3.6: (a) Spreading exponents α as a function of the aspect ratio $\epsilon = 2h_0/w$. Black symbols indicate experimental results measured on rivulets of width $w = 1.5$ mm (squares) and $w = 0.28$ mm (circles). The average experimental value of $\langle \alpha \rangle = 0.33$ is indicated by the gray dashed line. Simulation results are indicated by the red down-triangles. (b) Rim position 60 s after surfactant deposition as a function of the initial film height for $w = 1.5$ mm. Experimental data and numerical results are given by black squares and red triangles, respectively. The scaling behavior $x_{\text{rim}}(t = 60\text{ s}) \sim \sqrt{h_0}$ is indicated by the solid blue line

stripe zero film height and a no flux boundary condition for the sub-phase and the surfactant were imposed. At large distances from the deposition area a surfactant free liquid surface and undisturbed height profile of the rivulet were enforced.

In order to closely resemble the experimental conditions in which the relatively large amount of surfactant in the droplet ensures a ongoing supply of surfactant during the course of an experiment¹³⁴ a constant surfactant surface concentration was imposed, i.e., $\bar{\Gamma}(\bar{x} = 0, \bar{y}, \bar{t}) = \text{const.}$

Figure 3.6(b) shows the rim position 60 s after deposition, $x_{\text{rim}}(60\text{ s})$, as a function of the initial rivulet center height h_0 for $w = 1.5$ mm. Filled symbols represent experimental data, open triangles indicate numerical simulations by Myroslava Hanyak computed using the equations discussed above. A scaling relation for the rim position can be derived following the arguments made in chapter 2. The rim propagation rate is equated with the Marangoni velocity in the region beyond the crater area, $x > x_c$, where the film thickness is of order h_0

$$\frac{dx_{\text{rim}}}{dt} \approx \frac{h_0 \Delta \gamma_{\text{rim}}(t)}{\mu(x_{\text{rim}} - x_c)} \rightarrow x_{\text{rim}}(t) \approx x_c + S h_0^{1/2}. \quad (3.7)$$

Here, it is assumed that the expansion rate of the crater dx_c/dt is much smaller than the rim propagation rate dx_{rim}/dt . In this context, $\Delta\gamma_{\text{rim}} \equiv \gamma(x_{\text{rim}}) - \gamma(x_c)$ is the (time-dependent) surface tension difference between the edge of the crater and the rim position. The function S , which stems from the time-integration of $\Delta\gamma_{\text{rim}}/\mu$ and is, thus, influenced by the film evolution in the crater region, determines the spreading exponent α . It should be noted, that in chapter 2 the rim position was measured from the center of the deposited drop while for the data presented here the rim position was measured from the edge of the surfactant droplet, i.e. the edge of the surfactant droplet corresponds to $x = 0$, as shown in Fig. 3.4.

The numerically obtained peak positions in Fig. 3.6 appear to systematically lie slightly below the experimental values. A probable reason for this offset is water absorption from the ambient atmosphere due to the hygroscopic nature of glycerol. Already a water weight fraction as low as 3% results in a viscosity decrease of roughly 50% in the relevant temperature range¹³⁰. The plotted simulation results were converted to dimensional values assuming the viscosity of pure glycerol at 25 °C.

3.2.2 Sub-phase morphology evolution

A systematic change in the height and shape of the propagating rim can be observed during the course of an experiment as is illustrated by the interference images shown in Fig. 3.7. Initially the rim exhibits a considerable asymmetry in the streamwise direction, which gradually disappears at later stages. This asymmetry in early stages manifests itself in the longitudinal spacing of the interference fringes, which is more dense ahead of the peak position than behind it, as depicted in Fig. 3.7(a) for $t = 30$ s. In Fig. 3.7(b), at $t = 250$ s, the asymmetry, which is especially pronounced for low aspect ratio experiments, has largely disappeared.

In Fig. 3.8 the experimentally determined temporal evolution of the non-dimensional rim height h_{max}/h_0 is compared with numerically obtained values as presented by Myroslava Hanyak¹³⁴. The dimensionless time was hereby calculated according to eq.(3.1).

During the initial formation process of the rim, a rapid increase of h_{max} for times below $\bar{t} = 0.2$ is observed in the numerical simulations by Myroslava Hanyak¹³⁴, represented by the red solid line. These early times are not straight forwardly accessible in experiments since the microscope field of view is frequently obstructed by the deposition needle and the interference fringes are spaced close to each other, due to the high slopes of the rim, as seen in Fig. 3.3. High magnification objectives, suffering from limitations on the field of view, would therefore be necessary to resolve the interference pattern sufficiently. Following the initial formation process the rim height then effectively reaches a plateau value as shown for an aspect ratio $\varepsilon = 0.01$ in Fig. 3.8. At later times a pronounced increase of h_{max} is apparent. The experimental data obtained for $\varepsilon \approx 0.01$ (represented by circles and squares in Fig. 3.8) reproduce this behavior very well, both with respect to the onset time and amplitude of the peak height increase. The experimental data is in almost perfect quantitative agreement with the numerical results.

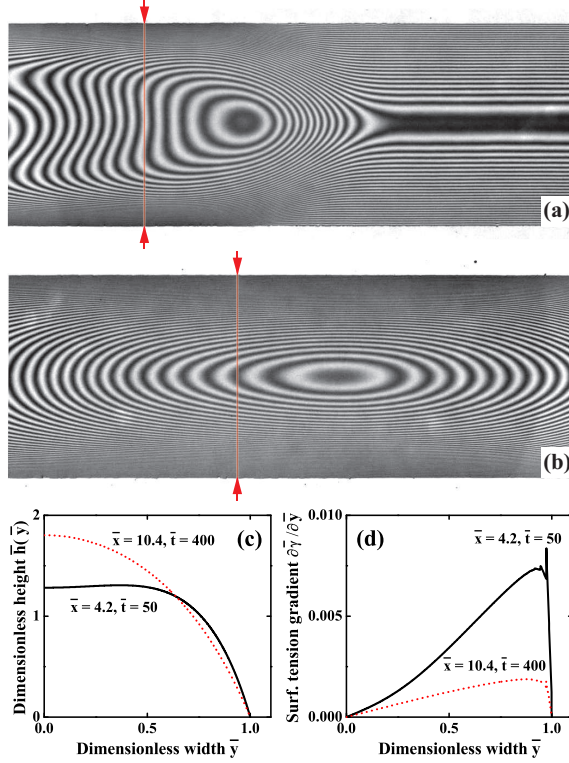
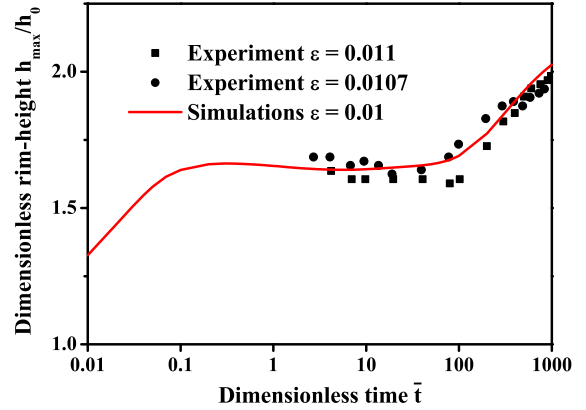


Figure 3.7: Interference microscopy images of the propagating rim at (a) an early stage ($t = 30$ s) and (b) a later stage ($t = 250$ s). The images clearly illustrate a transition in the morphology of the propagating rim. (c) Numerically calculated transverse height profiles $\bar{h}(\bar{y}, \bar{t})$ for times $\bar{t} = 50$ and $\bar{t} = 400$ located at the distance $w/2$, behind the rim. (d) Corresponding surface tension gradients in y -direction $\partial\bar{\gamma}/\partial\bar{y}$ for $\bar{t} = 50$ and $\bar{t} = 400$ located at the distance of $w/2$, behind the rim. Input parameters for (c) and (d) are $\bar{x}_0 = 0.5$, $Pe_s = 1000$, $\varepsilon = 0.01$, and $Bo = 0$, as used by Hanyak¹³⁴.

The increase in the rim height can be attributed to changes in the transverse rivulet height profile, which are a consequence of declining lateral surface tension gradients. The transverse height profile at the position of the red markers in Fig. 3.7 exhibits a strong flattening in the middle of the rivulet as evidenced by the straight run of the interference fringes. At a later time [Fig. 3.7(b)] this flattening has disappeared and the rivulet cross-section is to good approximation parabolic. The same behavior is observed in numerical simulations depicted in Fig. 3.7(c), where the dimensionless height profile $\bar{h}(\bar{x}_{\text{rim}} - 1, \bar{y})$ at a distance of half a rivulet width behind the peak position is plotted for two different times.

This qualitative difference in the height profiles is caused by lateral concentration gradients originating from the non-uniform surface velocity profile. As the driving force of the spreading process is Marangoni stress, the flow velocity scales with the local film thickness. Since the film thickness is 0 at the boundaries of the hydrophilic stripe, the streamwise velocity is higher in the middle of the rivulet as compared to its edges. The lateral shear in the velocity distribution initially leads to a non-uniform surfactant surface distribution $\Gamma(y)$. Darhuber *et al.*²⁸ studied rivulet shape distortions as a consequence of transverse temperature gradients and identified the relevant non-dimensional number as $\tau/(\varepsilon p_{\text{cap}})$ where p_{cap} is the capillary pressure. As soon as the value of $\tau = \nabla_{\parallel}\gamma$ falls below a certain threshold, the shape distortion gradually vanishes and the parabolic

Figure 3.8: Temporal evolution of the dimensionless rim height $\bar{h}_{\max}(\bar{t})$. The solid red line represents a simulation by Myroslava Hanyak¹³⁴. Symbols represent experimental data obtained for $w = 1.5$ mm and aspect ratios of $\varepsilon = 0.011$ (squares) and $\varepsilon = 0.0107$ (circles). The experimental data is in almost perfect quantitative agreement with the numerical results.



cross-section is restored. The same mechanism is conjectured to be the origin of the shape distortions in Figs. 3.7(a-d). This is supported by Fig. 3.7(d) where a strong decay of the lateral surface tension gradient at positions and times corresponding to the curves in Fig. 3.7(c) is evident. The relaxation of the transverse height profile towards a parabolic shape implicates an increase in the center height, which explains the increase in rim height h_{\max} observed in Fig. 3.8. Larger values of the aspect ratio ε are associated with a higher lateral curvature and hence an increased capillary pressure, which acts as the restoring force for the transition in the height profile. Consequently the transition occurs earlier for larger aspect ratios¹³⁴. Note that an increase in the peak height observed for one-dimensional spreading can only occur due to sub-phase expulsion¹³³ and that the effect observed in Fig. 3.8 is a consequence of lateral confinement due to chemical patterning.

3.3 Soluble surfactant spreading

In contrast to the insoluble oleic acid, which is only spreading in the form of a monolayer along the surface of a glycerol film, sodium dodecyl sulfate (SDS, Sigma-Aldrich Product number 436143, purity 99%) is a soluble surfactant, i.e. being present in the bulk of the sub-phase liquid as well as at its surface. As will be illustrated by the systematic data presented in this section, this difference in the surfactant behavior results in a quantitative difference in the spreading dynamics of the surfactant as well as the evolution of the sub-phase morphology compared to the previously presented case of an insoluble surfactant.

The dependence of the glycerol surface tension γ on the SDS bulk concentration c was determined experimentally using a Wilhelmy plate technique, with the resulting data shown in Fig. 3.9. Using the Langmuir equilibrium surfactant adsorption isotherm

$$\frac{\Gamma_{\text{eq}}}{\Gamma_{\infty}} = \frac{c}{k_{1,2}\Gamma_{\infty} + c} \quad (3.8)$$

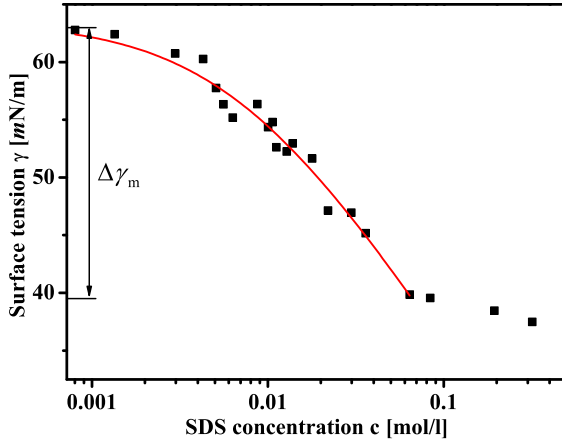


Figure 3.9: Surface tension of glycerol as a function of the SDS bulk concentration. The shown data was obtained using a Wilhelmy plate. For concentrations c exceeding 0.064 mol/l, a pronounced transition is visible in the surface tension dependence which can be ascribed to the formation of micelles in the bulk fluid. The red solid line corresponds to a fit according to eq.(3.8) and (3.9).

and the surface equation of state

$$\gamma = \gamma_0 + RT\Gamma_\infty \ln \left(1 - \frac{\Gamma}{\Gamma_\infty} \right) \quad (3.9)$$

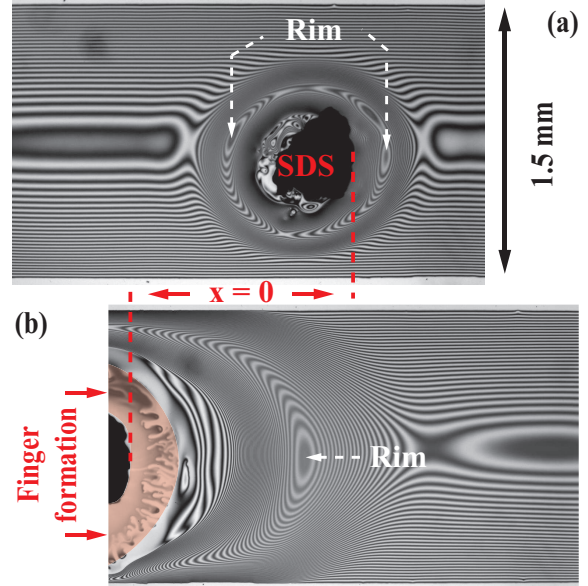
the experimental data was fitted as indicated by the red solid line where R is the universal gas constant and T is the absolute temperature. The corresponding fit parameters are a maximum surface coverage of $\Gamma_\infty = 4.2 \times 10^{-6} \text{ mol m}^{-2}$ and a ratio of the desorption and adsorption rate constants $k_{1,2} = 1.7 \times 10^6 \text{ m}^{-1}$.

For concentrations c exceeding 0.064 mol/l, a pronounced transition is visible in Fig. 3.9, which indicates the formation of micelles. In this range we furthermore observed gelation of the liquid associated with a strong change in the rheology of the liquid, which made surface tension determination in this concentration region somewhat unreliable.

Preparation of the initial conditions for the experiments described here is analogous to the insoluble case, i.e. a hydrophilic stripe is created on a hydrophobic background followed by the deposition of a thin liquid film of glycerol onto the hydrophilic area. While oleic acid is liquid at the experimental conditions and was deposited in the form of a droplet, SDS is a solid powder. Two different types of experiments are presented here. In the first type, termed *solid deposition*, a small pellet of compressed SDS powder was deposited onto the glycerol rivulets, in the second type, termed *solution deposition*, a 0.1 – 0.2 μl droplet of an SDS-glycerol solution with varying concentration was deposited.

Figure 3.10 (a) shows a typical example of a rivulet directly after deposition ($t = 0.33 \text{ s}$) of a solid piece of SDS. As in the case of the insoluble oleic acid, a crater forms around the location of deposition, rims form and propagate from the surfactant source along the sub-phase rivulet. Figure 3.10 (b) shows a rim propagating away from the surfactant source, 30.33 s after deposition. In the crater region around the surfactant source a slight formation of a fingering instability is visible, highlighted in red.

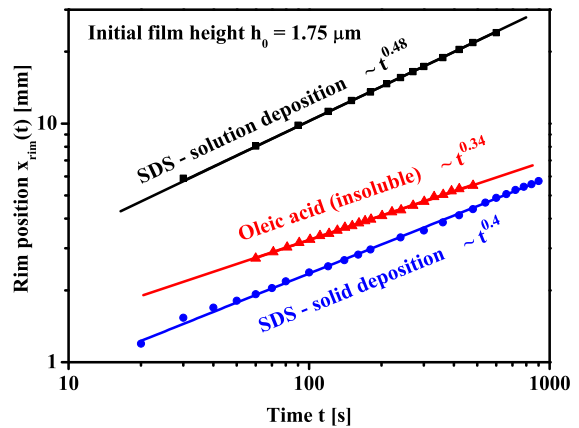
Figure 3.10: (a) Interference microscopy images of a glycerol rivulet, after deposition, $t = 0.33$ s, of a solid piece of SDS. A crater is forming around the deposited piece of surfactant and rims are forming and propagating along the rivulet. (b) A rim propagating away from the surfactant source, at $t = 30.33$ s. Slight finger formation in the crater region close to the surfactant source is visible (marked by the red underlay). Rivulet width $w = 1.5$ mm and initial center height $h_0 \approx 5.8 \mu\text{m}$, illumination $\lambda = 650$ nm.



In the case of solution deposition, i.e. the deposition of a droplet of SDS-glycerol solution onto the rivulet, the surfactant is not localized as for solid deposition. The deposited solution droplet, the surfactant source, spreads along the rivulet exhibiting a pronounced formation of digitated structures or fingers. To quantify the spreading rate in this case the center location of the initial contact of the surfactant drop and the sub-phase is taken as $x = 0$.

For both deposition techniques rims form and propagate away from the location of deposition and offer a convenient measure for the propagation of the surfactant front.

Figure 3.11: Measurements of the rim position as a function of time for solution- (black squares) and solid deposition (blue circles) of SDS as well as for the previously discussed insoluble surfactant oleic acid. The solid lines correspond to power law fits of the form $x_{\text{rim}} \sim t^\alpha$ with exponents α of 0.48 and 0.4 for solution and solid deposition, respectively. The propagation rate for the insoluble case is approximated by an exponent $\alpha = 0.34$.



In Fig. 3.11 the rim propagation as a function of time is shown for a solid and a liquid deposition experiment as well as for the insoluble oleic acid with identical initial sub-phase film thicknesses of $h_0 = 1.75 \mu\text{m}$. In all cases the rim position follows a power law of the form $x_{\text{rim}} \sim t^\alpha$ as illustrated by the solid lines, the fitted exponents are $\alpha = 0.48$ and 0.4 for solution and solid deposition, respectively. The propagation rate for the insoluble case is approximated by an exponent $\alpha = 0.34$. In the following, systematic results are presented first for solid deposition and subsequently for liquid deposition.

3.3.1 Solid deposition

Figure 3.12(a) shows fitted power law exponents α for solid deposition as a function of the aspect ratio $\varepsilon = 2h_0/w$. The exponents were obtained for rivulet widths of $w = 1.5 \text{ mm}$ and $w = 0.3 \text{ mm}$ as indicated by the triangles and squares, respectively. Since interference microscopy is limited to low film thicknesses, the smaller rivulet width w allowed the application of this method for higher aspect ratios.

As in the case of the previously discussed insoluble oleic acid the exponents are independent of the aspect ratio ε within the investigated range. The average numerical value of $\langle\alpha\rangle = 0.41$ however, is higher than the one measured for the spreading of the insoluble surfactant ($\langle\alpha\rangle = 0.33$). Figure 3.12(b) shows the rim position $x_{\text{rim}}(t = 1000 \text{ s})$ after solid deposition as a function of the initial film thickness for $w = 1.5 \text{ mm}$. The solid line in Fig. 3.12(b) corresponds to a power law relation $x_{\text{rim}}(1000 \text{ s}) \sim \sqrt{h_0}$, which

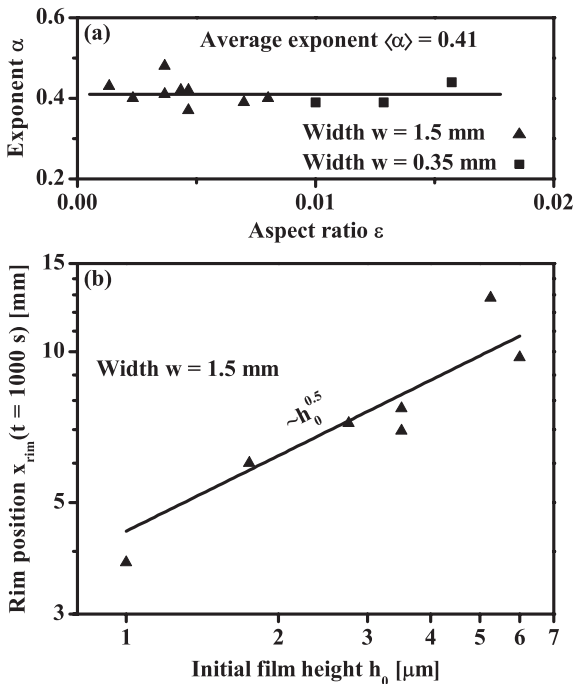
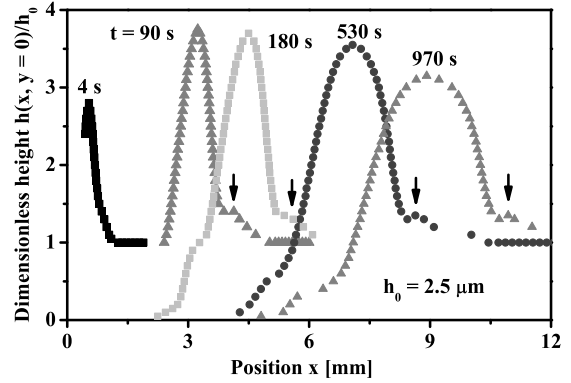


Figure 3.12: (a) Spreading exponents α for solid deposition as a function of the aspect ratio ε for rivulet widths of $w = 1.5 \text{ mm}$ (triangles) and $w = 0.3 \text{ mm}$ (squares). The average value of $\langle\alpha\rangle = 0.41$ is indicated by the solid line. (b) Rim position $x_{\text{rim}}(t = 1000 \text{ s})$ as a function of h_0 after solid deposition onto rivulets of width $w = 1.5 \text{ mm}$. Experimentally obtained values are indicated by symbols, the scaling relation $x_{\text{rim}}(1000 \text{ s}) \sim \sqrt{h_0}$ is indicated by the solid line.

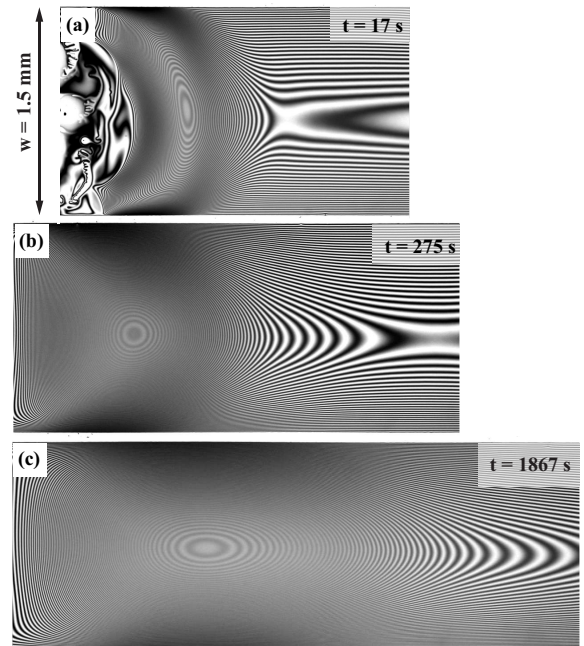
Figure 3.13: Centerline height profiles $h(x, y = 0, t)$, obtained by analysis of the corresponding interference fringe patterns. An initial sharp increase in rim height is followed by a broadening of the peak. The black arrows indicate a plateau region ahead of the rim, which is a possible signature of a minute surface active contamination of the substrate⁶¹.



is an excellent approximation to the experimentally measured results. The same scaling with h_0 had been observed for the case of insoluble surfactants^{133,134} as described earlier in this chapter. The scaling argument leading to Eq. (2.2) and Eq. (3.7) can be applied here. The different type of surfactant influences the difference in local surface tensions between the crater edge at x_c and the rim $\Delta\gamma_{\text{rim}} \equiv \gamma(x_{\text{rim}}) - \gamma(x_c)$. This in turn enters into the pre-factor following the time integration, such that the scaling $x_{\text{rim}}(1000 \text{ s}) \sim h_0^{0.5}$ remains.

In Fig. 3.13 exemplary centerline height profiles $h(x, y = 0, t)$, obtained by analysis

Figure 3.14: Interference microscopy images of a rim propagating along a glycerol rivulet following the deposition of compressed SDS powder, i.e. solid deposition, at, (a) $t = 17 \text{ s}$, (c) $t = 275 \text{ s}$ and (d) $t = 1867 \text{ s}$. Rivulet width $w = 1.5 \text{ mm}$ and initial center height $h_0 = 5.63 \mu\text{m}$. In the initial stage of the spreading the propagating rim exhibits a strong asymmetry between front and back.



of corresponding interference fringe patterns, are presented for different times after solid deposition. The peak height of the rim h_{\max} is initially increasing and was determined to reach a maximum value of about $3.75h_0$ in intermediate stages of the experiment. As the spreading progresses the peak is observed to widen over time and in later stages a decrease of the peak height is visible. Noteworthy in the height profiles shown in Fig. 3.13 is the existence of a small plateau region or local maximum ahead of the propagating rim, indicated by the downwards facing arrows. A possible origin for this peculiarity in the rim shape was found to be a minute amount of a pre-existing surface active contaminant on the sub-phase rivulet⁶¹. While such a contamination would not measurably affect the spreading rate of the surfactant, it can lead to distortions in the morphology.

As in the case of the earlier discussed insoluble surfactant spreading, a systematic change in the shape of the rim as it propagates along the rivulet was observed in experiments. Initially the rim exhibits a considerable asymmetry in the stream-wise direction, which gradually disappears at later times. The asymmetry at early stages manifests itself in the curvature of the interference fringes, which is strong ahead of the peak position while the fringes are practically orthogonal to the flow direction behind the peak, as depicted in Fig. 3.14(b). As the experiment progresses this asymmetry vanishes as shown in Fig. 3.14(c). This is reminiscent of the morphology transition discussed before in the context of insoluble surfactant spreading, e.g. Fig. 3.7, which was associated with diminishing transversal surface tension gradients.

3.3.2 Solution deposition

While in experiments where a drop of insoluble or a solid piece of soluble surfactant was deposit onto the rivulet, a well defined localized source region was present, this was not

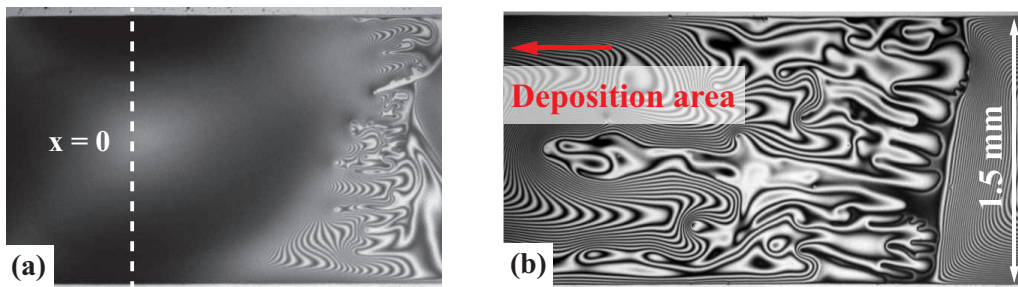
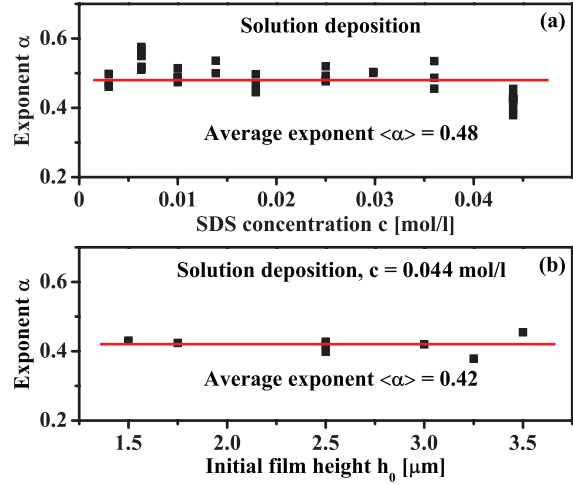


Figure 3.15: (a) Expanding deposition area in a solution deposition experiment, 8 s after deposition. Strong fingering accompanies the expansion of the surfactant source. The center of the initial contact region between the deposited drop and the sub-phase rivulet, $x = 0$, is indicated via the dashed white line. (b) Solution deposition results in pronounced finger formation as the deposited droplet of surfactant solution spreads along the rivulet, as seen in this microscope image for $h_0 = 1.63 \mu\text{m}$, $w = 1.5 \text{ mm}$ and $t = 542 \text{ s}$ after deposition.

Figure 3.16: (a) Fitted spreading exponents for various concentrations of deposited SDS solution for initial liquid film heights in the range of $1.5 \mu\text{m} \leq h_0 \leq 4.5 \mu\text{m}$. (b) Fitted spreading exponents as a function of initial liquid film height for the concentration $c_0 = 0.044 \text{ mol/l}$ of the deposited SDS solution.



the case for solution deposition experiments. The deposited droplets of SDS glycerol solution spread out as shown in Fig. 3.15 such that these experiments are subject to an expanding source of surfactant. Figure 3.15(a) shows a typical snapshot of such an expanding source area 8 s after deposition, the drop spreads out under a pronounced formation of fingers^{4-6,45,46,75,91,143,149}.

Figure 3.16(a) shows the spreading exponent α for the case of solution deposition, as a function of the surfactant concentration in the deposited droplet. The exponent appears to be independent of the surfactant concentration with an average value of $\langle \alpha \rangle = 0.48$. Merely for the highest of the investigated concentrations of $c = 0.044 \text{ mol/l}$, a slight decrease in the spreading exponent is noticeable. The SDS solution with concentration of $c = 0.044 \text{ mol/l}$ became turbid and gel-like, furthermore, its viscosity was increased as compared to solutions with lower concentration. The corresponding local increase in viscosity retarded the spreading dynamics of the deposited solution droplet, such that the experiment resembles more the case of solid SDS deposition. Consistent with this notion, a reduction of the measured spreading exponent towards the average value shown in Fig. 3.12 for solid deposition is observed. Figure 3.16(b) shows the spreading exponent α measured for different initial film heights h_0 and deposited droplets with a surfactant concentration of $c = 0.044 \text{ mol/l}$, consistent with the results in Fig. 3.12. The spreading exponent is to good approximation independent of the film thickness within the considered range with an average value of $\langle \alpha \rangle = 0.42$.

3.4 Summary

In this chapter a systematic study of surfactant spreading on sub-phase films exhibiting a confinement-induced surface curvature has been presented. This is the first study in

which chemical surface patterns were experimentally employed to implement a sub-phase confinement in the context of surfactant spreading. An insoluble as well as a soluble surfactant were considered and both were found to spread according to a power law relation $x_{\text{rim}} \sim t^\alpha$. The spreading exponent α for the insoluble surfactant oleic acid was determined to be $\alpha = 0.33$. For the soluble surfactant SDS results for two types of experiments were presented, in the first a solid piece of SDS was deposited and in the later a drop of SDS solution. Exponents were found to lay above the value determined for the insoluble surfactant with $\alpha = 0.41$ and $\alpha = 0.48$ for solid and solution deposition, respectively. An expanding surfactant source area was suggested as the origin of the increased spreading exponents measured for solution deposition.

Besides the spreading rate of the surfactants the sub-phase morphology evolution was evaluated. A pronounced transition in the shape of the rim, propagating along the rivulet as a consequence of the spreading, was described for the insoluble surfactant. On the basis of a quantitative comparison of the experimental data with numerical results of Myroslava Hanyak¹³⁴ it was shown that the transition in the sub-phase morphology is induced by diminishing lateral surface tension gradients. These surface tension gradients are a consequence of the laterally non-uniform velocity and surfactant surface concentration profiles resulting from the curved sub-phase interface due to the chemical confinement. Besides the quantitative agreement of the morphology evolution comparison with numerical results also confirms the experimentally measured value of the spreading exponent¹³⁴.

Note: The results presented in this chapter have been published in combination with numerical work by Myroslava Hanyak: *D. K. N. Sinz, M. Hanyak, J. C. H. Zeegers, and A. A. Darhuber, Insoluble surfactant spreading along thin liquid films confined by chemical surface patterns, Physical Chemistry Chemical Physics, Vol. 13 pp. 9768 - 9777, 2011.* as well as *M. Hanyak, D. K. N. Sinz, and A. A. Darhuber, Soluble surfactant spreading on spatially confined thin liquid films, Soft matter, Vol. 8 pp. 7660-7671, 2012.*⁶¹.

Chapter 4

Surfactant spreading at the interface of two thin liquid films

4.1 Introduction

In the introduction of chapter 1 a review of the vast body of literature dedicated to surfactant spreading^{4-6,11,15,35,38,46,49,51,52,57,58,61,64,73,91,133,134,143,146,149} at the air interface of liquid layers comprising various configurations was given. The spreading of surfactants at the interface between two liquid phases on the other hand, has not received much attention yet. Recently, a first systematic study of Marangoni driven surfactant spreading at the interface between two deep liquid layers has been presented by Berg⁹. In this study Berg used deep layers of decane and water. The spreading kinetics of several types of surfactant at the interface between the two layers were investigated experimentally. A scaling relation, derived by balancing the interfacial tension gradient and viscous stresses in the boundary layers in the two liquid phases, was in quantitative agreement with the experimental data. As already pointed out in chapter 1 for the application of surfactants in an oil reservoir the spreading at the interface between an oil- and a water-phase can be expected to dominate the distribution of introduced surfactants or surfactant solutions. When considering surfactant spreading in the context of oil recovery the liquid layers can be expected to be subjected to both physical and chemical confinements, i.e. physical rock structures as well as varying wettability of these structures.

This chapter addresses surfactant spreading in an experimental configuration intended to emulate certain aspects of spreading under reservoir conditions. Spreading is investigated at the interface between two thin liquid layers. As in the previous chapter, one of the liquids is confined by a chemical surface pattern inducing a curvature of the liquid interface. For these experiments a thin rivulet of polar liquid is immersed in a thin layer of a second, non-polar liquid. The spreading dynamics of a surfactant, soluble in the polar/aqueous-like phase, are investigated systematically. Details of the experimental setup are explained below.

4.2 Sample fabrication and experimental setup

Figure 4.1 illustrates the preparation of the initial condition for the experiments discussed in this chapter. Chemical patterning was used to create hydrophilic stripes with a length of $L = 50$ mm and a width $w = 1.5$ mm on masked borosilicate glass slides (Gold Seal coverslips, dimensions 48 mm \times 60 mm, thickness 150 mm, product number 3334) in the same fashion as described in chapter 3.

Hydrophilic regions of the chemically patterned glass substrates (bottom substrate) were spin-coated with a thin film of glycerol (rivulet) in which fluorescein sodium salt (Sigma Aldrich, product number 46960) was dissolved at a concentration of 0.05 wt%, Fig. 4.1 (a). Two spacers (borosilicate glass slides, thickness 80 μ m) were placed on both sides of the rivulet which kept a second glass slide (top-plate) elevated at a well-defined distance. The length of the top plate is slightly shorter than the rivulet, as illustrated in Fig. 4.1 (c,d). Using two stainless steel clamps on either side of the rivulet the entire setup was then clamped together. Once the glass construction was fixed, dodecane was deposited at one edge of the top-plate and imbibed into the cavity space between the two glass plates by capillary action, Fig. 4.1 (d). As a consequence of the high viscosity contrast, the initial liquid distribution along the length of the glycerol rivulet remained unaltered by the imbibing dodecane. Spacers, top-plate as well as the steel clamps were thoroughly cleaned before the individual experiments. Prior to the patterning and experiments, the substrates were cleaned by immersion in a solution of hydrogen peroxide (30%, J.T. Baker product number 7047) and sulfuric acid (95%, J.T. Baker product number 6057), mixed at a volume ratio of 1:1.

High purity grade dodecane (purity $> 99\%$, Sigma Aldrich product number 221104) was used in the experiments. However, measurements using a pendant drop tensiometer showed the interfacial tension of the dodecane against DI-water, not only to strongly

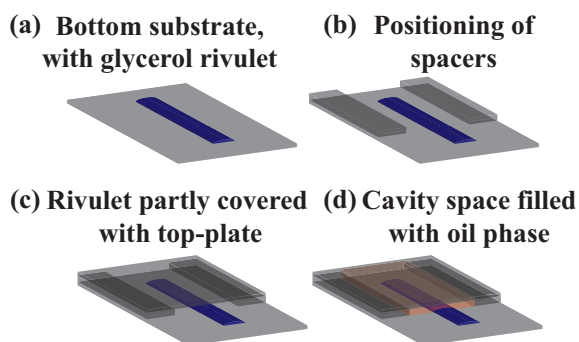
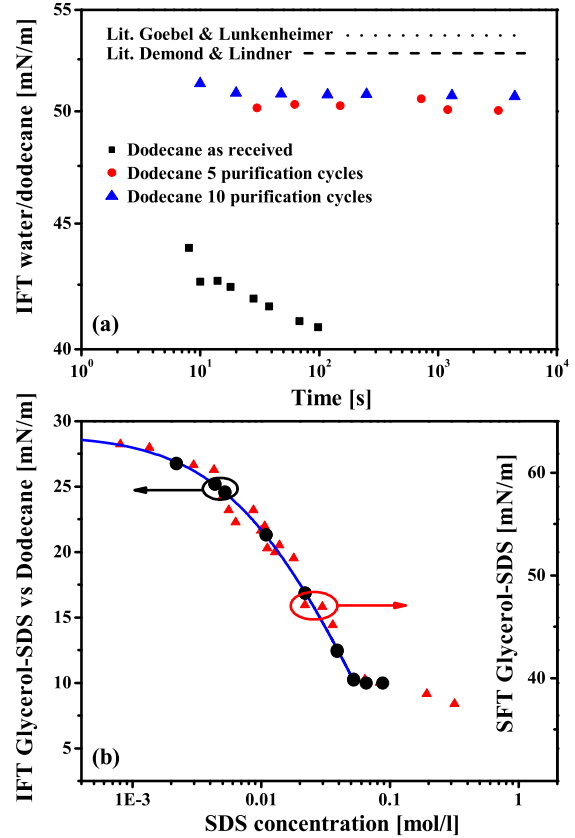


Figure 4.1: Sketch of the experimental configuration for the spreading of surfactants at the liquid-liquid interface of spatially confined thin fluid layers. (a) A thin film of glycerol, containing fluorescein, is deposited on a chemically patterned glass slide. (b,c) Two glass spacers, placed parallel to the rivulet, elevate a top cover plate at a distance of ≈ 80 μ m above the bottom substrate. (d) The resulting cavity space is filled with dodecane.

Figure 4.2: (a) Interfacial tension of dodecane against water, measured using a pendant drop tensiometer. Shown are values for dodecane as received (black squares), dodecane that was purified 5 (red circles) and 10 times (blue triangles) as well as literature values (black dashed and dotted lines). (b) Liquid-liquid interfacial tension of glycerol-SDS solutions against purified dodecane, measured using a pendant drop tensiometer (black circles, left axis). Also shown, air-liquid surface tension values of glycerol-SDS solutions (red triangles, right axis, see section 3.3). The solid blue line represents a Langmuir isotherm $\gamma = \gamma_0 + A \ln(1 - \frac{c}{c+B})$ fitted onto the liquid-liquid interfacial tension data with the parameters $A = 9.9 \text{ mN/m}$, $B = 0.00915 \text{ mol/l}$ and the interfacial tension for a clean interface of $\gamma_0 = 29 \text{ mN/m}$.



differ from literature values of $\gamma_{O/W}(25^\circ\text{C}) \approx 53 \text{ mN/m}$ ^{34,54,153} but also to exhibit a time dependence as shown in Fig. 4.2(a). This is known to indicate the presence of surface active impurities in unpurified alkanes^{34,50,53,54,153}. To eliminate any influence on the spreading dynamics during experiments, the dodecane was purified by adding basic Aluminum oxide (Sigma Aldrich, product number 199443). After several hours the Aluminum oxide was removed using a vacuum filtration setup. This cleaning step was repeated ten times, the IFT values measured for the dodecane purified in this fashion were within the range of scatter for the different reported literature values and showed no time dependence over the course of one hour, as shown in Fig. 4.2(a).

In Figure 4.2(b) IFT values for the purified dodecane against glycerol-SDS solutions are shown as a function of the SDS content in the glycerol phase. Also shown are values for the air-liquid surface tension of glycerol-SDS solutions measured using a Wilhelmy plate (red triangles, right axis). The experimental data for the liquid-liquid interfacial tension was fitted with a Langmuir isotherm $\gamma = \gamma_0 + A \ln(1 - \frac{c}{c+B})$ with the parameters $A = 9.9 \text{ mN/m}$, $B = 0.00915 \text{ mol/l}$ and the interfacial tension for a clean interface of $\gamma_0 = 29 \text{ mN/m}$, shown by the solid blue line in Fig. 4.2(b).

After preparation of the initial condition as shown in Fig. 4.1 (d), a solid pellet of the surfactant SDS (Sodium Dodecyl Sulfate, purity > 99%, Sigma Aldrich product number 436143) was deposited onto the glycerol rivulet, between the glass slides. As in the case of deposition at the liquid-air interface (chapter 3) the glycerol rivulet thinned around the deposited surfactant source and a rim formed and propagated along the rivulet. The dynamics following the surfactant deposition were monitored by fluorescence microscopy using an Olympus BX71 inverted microscope.

For sample illumination a Thorlabs LED light source (product number M470L2-C1) was combined with a fluorescence filter cube, limiting the wavelength for excitation λ_{exc} to $460 \text{ nm} < \lambda_{exc} < 480 \text{ nm}$. The dichroic mirror had a cut off wavelength of $\approx 485 \text{ nm}$ and the emission filter limited the wavelength of the emitted light reaching the detector λ_{em} to $495 \text{ nm} < \lambda_{em} < 540 \text{ nm}$. Recorded grayscale values, corresponding to fluorescence intensity, increased with sub-phase film thickness. In order to allow for quantitative morphology evaluations during the entire course of the experiment, the illuminating light was pulsed to avoid photo-bleaching. To correlate the measured fluorescence intensity values to film height of the deposited glycerol layer, a rivulet of known film height was used to calibrate the relation between measured fluorescence intensity and film thickness. The known relation between lateral position and film thickness allows for an accurate calibration of the film thickness vs. fluorescence intensity⁷⁹.

4.3 Results

Following surfactant deposition, as in the case for spreading at liquid-air interfaces, a pronounced thinning of the sub-phase liquid in the vicinity of the deposited surfactant source is observed along with the formation and propagation of a rim or maximum in sub-phase film thickness^{15,35,73,133,134}. Figure 4.3 shows the typical experimentally observed evolution of the height of this rim as a function of time. The initial rivulet center film height in this experiment was $h_0 = 7.7 \mu\text{m}$. In the initial phase of the experiment the

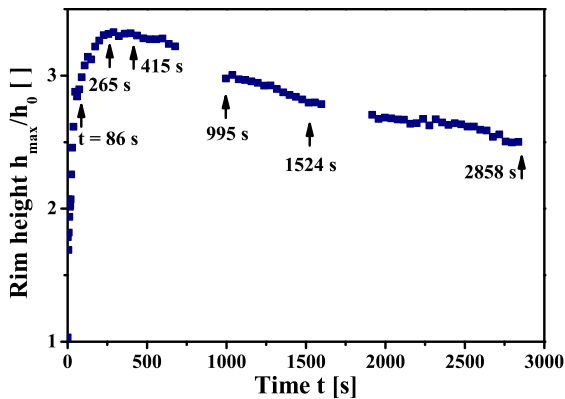


Figure 4.3: Dimensionless height of the propagating rim h_{max}/h_0 as a function of time. The initial film thickness in this experiment was $h_0 = 7.7 \mu\text{m}$. A maximum in the rim height is reached at $t \approx 300 \text{ s}$ after surfactant deposition.

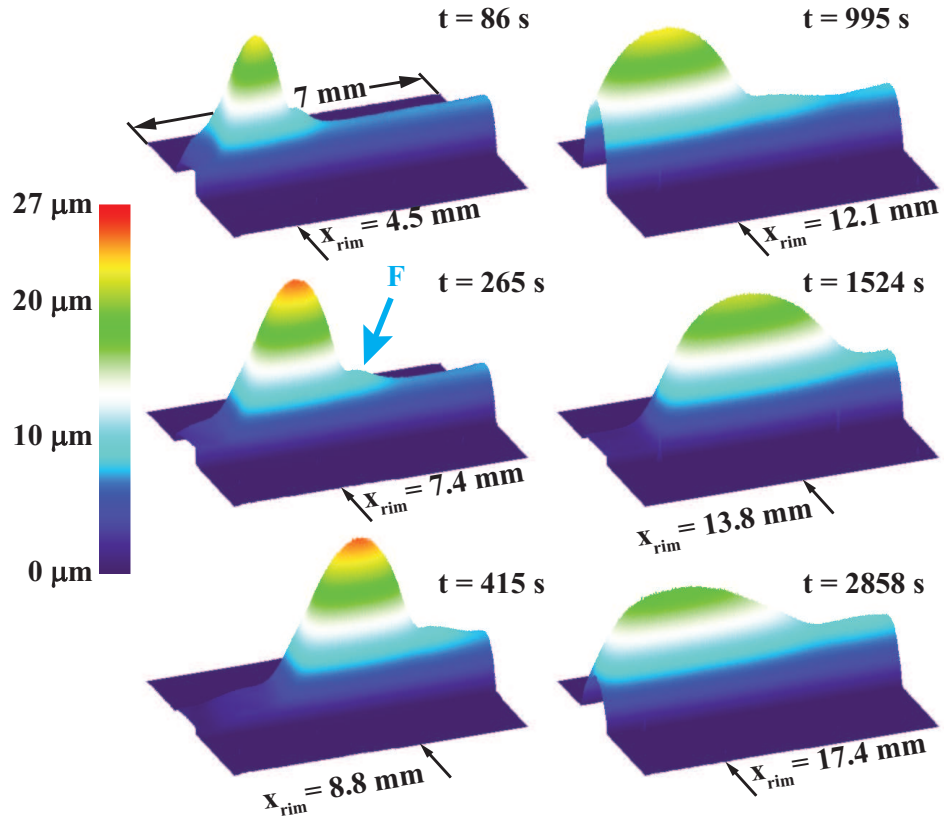


Figure 4.4: 3-D color-coded contour plots of the rim morphology evolution, initial rivulet center film thickness $h_0 = 7.7 \mu\text{m}$ and width $w = 1.5 \text{ mm}$. The rim height evolution of the same experiment is shown in Fig. 4.3. The times corresponding to the different snapshots are indicated along with the respective rim positions. The blue arrow labeled F (plot for $t = 265 \text{ s}$) indicates a local plateau region or 'foot' preceding the advancing rim.

height of the rim increased rapidly and reached its maximum height of $h_{max}/h_0 \approx 3.3$ at $t \approx 300 \text{ s}$, followed by a gradual decrease. Figure 4.4 shows 3-D color-coded contour plots of the advancing rim at different times after deposition for the same experiment as shown in Fig. 4.3. The morphology maps were obtained by conversion of the measured 2-D fluorescence intensity profiles via the calibration curve described above. The corresponding rim positions are indicated along with the times at which the snapshots were obtained. In the first two images ($t = 86 \text{ s}$ and $t = 265 \text{ s}$) the rim exhibits a steeper longitudinal slope ahead of its peak than behind it. In the course of the experiment this configuration changes and the longitudinal slope ahead of the peak becomes increasingly shallow ($t = 415 \text{ s}$ to $t = 2858 \text{ s}$). This decrease in the slope of the film is accompanied

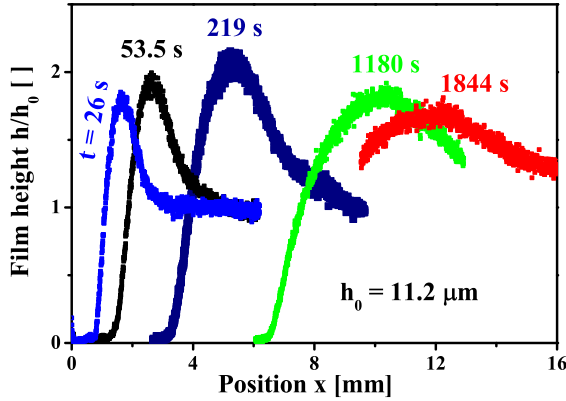


Figure 4.5: Dimensionless center-line height profiles illustrating the morphology evolution of a propagating rim for different times following surfactant deposition onto a rivulet of initial height $h_0 = 11.2 \mu\text{m}$. In this experiment unpurified dodecane was used. Compared to experiments with purified dodecane a drastic decrease in the maximum measured film height is evident.

by a decrease in maximum film height h_{max} as already shown in Fig. 4.3.

Another feature of the advancing rim is a small preceding plateau region or foot ahead of the actual rim. This foot is marked in Fig. 4.4 at $t = 265 \text{ s}$ with a blue arrow labeled F. For SDS spreading at the air-liquid interface of glycerol rivulets this foot was already described in Chapter 3. As previously mentioned, the presence of low concentration of surface active impurities in the glycerol offers an explanation for this phenomenon⁶¹.

This peculiarity in the rim morphology, however, does not originate from the surface-active contaminants present in the unpurified dodecane oil-phase described in section 4.2. Typical centerline height profiles for spreading experiments with the unpurified oil-phase are shown in Fig. 4.5. The discussed foot ahead of the rim is not present in the shown profiles. Furthermore, compared to the experiments with purified dodecane, a drastic decrease in the maximum measured film height is evident. With the unpurified oil-phase, a maximum dimensional rim height of only $\approx 2.1h_0$ was reached, while for the case of a purified oil phase was purified (Fig. 4.4 and Fig. 4.3) a maximum value of

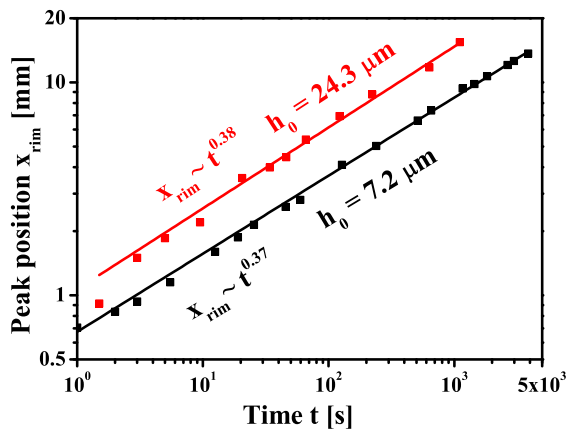
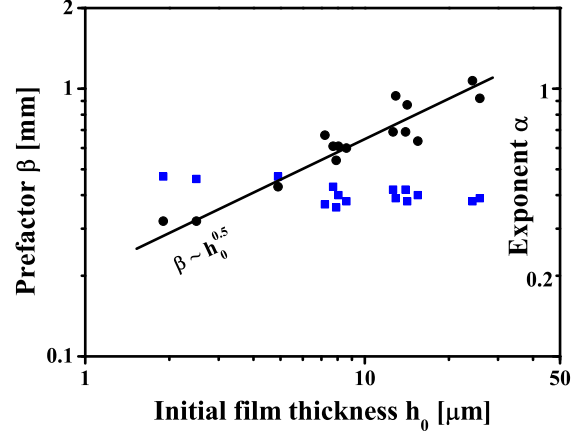


Figure 4.6: Example measurements of the rim position as a function of time for film heights of $h_0 = 24.3 \mu\text{m}$ (red squares) and $h_0 = 7.2 \mu\text{m}$ (black squares). The rim positions $x_{rim}(t)$ are approximated by the power-law relation $x_{rim}(t) = \beta t^\alpha$ (solid lines).

Figure 4.7: Prefactors β (black circles) and exponents α (blue squares) for a power-law of the form $x_{rim}(t) = \beta t^\alpha$ fitted to experimental data. Values are given as a function of the initial centerline film height h_0 . The black solid line indicates the scaling behavior for the prefactor with the film thickness $\beta \sim h_0^{0.5}$.

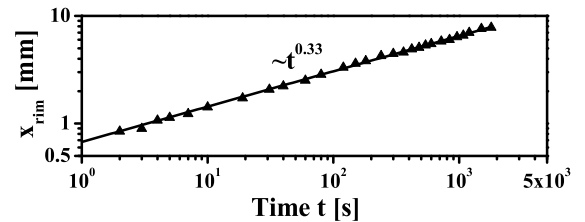


$h_{max}/h_0 \approx 3.3$ was reached.

Rim positions $x_{rim}(t)$ as a function of time are shown in Fig. 4.6 for film thicknesses of $h_0 = 7.2 \mu\text{m}$ and $h_0 = 24.3 \mu\text{m}$, indicated by red and black symbols respectively. In both cases $x_{rim}(t)$ is approximated by a power-law of the form $x_{rim}(t) = \beta t^\alpha$ (solid lines). Figure 4.7 shows fitted spreading exponents α (blue squares) and prefactors β (black circles) as a function of the initial rivulet centerline film height h_0 . Spreading exponents appear to first approximation constant over the investigated range with an average value of $\alpha = 0.4$. This value is slightly increased for the experiments with an initial rivulet height $h_0 \leq 5 \mu\text{m}$. The solid black line indicates the scaling behavior for the prefactor with the film thickness $\beta \sim h_0^{0.5}$. The scaling is therefore equivalent to the one for liquid air spreading. The relation can be derived analogously to chapter 2 and 3 since the viscous friction occurs predominantly in the glycerol and the viscosity (≈ 870 mPas) of the dodecane layer (≈ 1.3 mPas) can be neglected. This is also supported by the fact that the qualitative spreading dynamics, i.e. the spreading exponents are very close to the ones measured for deposition of solid SDS at the liquid-air interface (section 3.3).

Besides a pronounced influence on the morphology of the rim, the use of unpurified dodecane in the spreading experiments also resulted in a reduction of the observed spreading exponents. A typical graph for the rim position as a function of time for spreading in unpurified dodecane is shown in Fig. 4.8, where the experimental data is approximated by $x_{rim} \sim t^{0.33}$. A reasonable explanation for the decrease in the exponent,

Figure 4.8: Rim position as a function of time for spreading along a glycerol rivulet ($h_0 = 15 \mu\text{m}$) immersed in an **unpurified** dodecane layer.



compared to the case of purified dodecane shown in Fig. 4.7, is an effective decrease in the spreading pressure of the deposited surfactant $\Pi = \gamma(\Gamma = 0) - \gamma(\Gamma = \Gamma_\infty)$ in the course of the experiments. This hypothesis is supported by the data shown in Fig. 4.2, the interfacial tension of the unpurified dodecane (black squares) against water gradually decreased over time. An analogous behavior can be expected for the interfacial tension against glycerol. In the spreading experiments, therefore, the interfacial tension of the rivulet ahead of the spreading front decreases in time and with it the effective spreading pressure of the surfactant.

In his experiments on spreading between deep layers of decane and water, Berg⁹ used the alkane as received, i.e. without prior purification. This is also reflected in the reported interfacial tension value between decane and water of 48 mN/m which is below the value of ≈ 52 mN/m in other references^{50,54}. However, while the purification of the oil-phase proved to have a significant influence on the both the qualitative spreading behavior and the temporal morphology evolution of the thin rivulet described here, no such effects are to be expected for the spreading between deep fluid layers. The duration of the spreading experiments reported here was in the range of several 1000 s while the spreading in Berg's experiments was completed within < 1 s. Based on the interfacial tension data shown in Fig. 4.2 for the unpurified alkane, changes in the interfacial tension within 1 s would be small compared to the spreading pressure of the surfactant. The changes would therefore have an influence on the spreading far below the measurement accuracy, assuming the nature of the impurities is equivalent to the ones reported here.

4.4 Summary

The existing literature on surfactant spreading is mainly focused on the spreading at liquid-air interfaces. The spreading has been investigated at the interface between air and deep^{18,36,37,47,66,72,141} as well as thin^{11,51,52,57,73,133,134,142,143} liquid layers. The spreading of surface active substances at the interface of two deep liquid layers was recently studied by Berg⁹. As in the case of the liquid-air interface, spreading dynamics change when the step to thin liquid films is taken. In this chapter the spreading of a surfactant at the interface of a thin rivulet of polar liquid under a layer of non-polar liquid was examined. Both liquid layers were spatially confined, on the one hand by glass substrates and in the case of the polar liquid by a chemical surface pattern. Both the spreading dynamics as well as the liquid-liquid interface morphology evolution were studied systematically.

The surfactant used in the presented study was ionic and to good approximation insoluble in the non-polar phase. A change in the spreading dynamics can be expected for the application of a surfactant soluble in the non-polar phase or both phases. In the current configuration the surfactant concentration at the liquid-liquid interface is influenced by the desorption into the rivulet, i.e. the polar bulk-phase. For a surfactant soluble in both phases, desorption fluxes of the surfactant from the interface into both the bulk phases influence the interfacial concentration. In the current setup the non-polar bulk

occupies a significantly larger volume. Depending on partitioning coefficients, desorption into the non-polar phase therefore can potentially reduce the interfacial surfactant concentration significantly stronger than the desorption into the polar bulk in the current experiments.

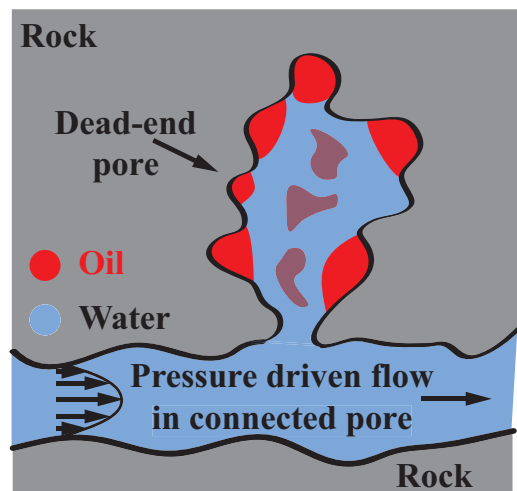
Chapter 5

Marangoni transport of surfactants along discontinuous liquid-liquid interfaces

5.1 Introduction

In the previous chapter the spreading of a surfactant at the interface of two thin liquid layers was addressed. This study was, as all existing surfactant spreading literature, limited to a configuration with a continuous interface between the different phases along which the surfactant spread. Considering conditions in an oil reservoir, interfaces may not be continuous over long distances, but either the oil or the water phase can be in discrete locations predetermined for example by varying wettability of the surrounding rock pores. As already pointed out in section 1 surfactant induced Marangoni flow offers

Figure 5.1: Artists impression of a dead-end pore geometry with a mixed wet pore surface as potentially encountered in an oil reservoir. Grey areas symbolize rock, blue areas correspond to pore space filled with water and the red areas depict un-connected oil droplets or films. Pressure driven flow from injection to production wells would not allow to mobilize oil in such a pore configuration. Transport of functional materials, e.g. wettability modifiers, by these flows is also limited to connected pore paths.



an efficient mechanism to create flow in dead-end pore geometries that are inaccessible to regular pressure driven flow created for example during a water flood. For the case of a continuous oil-water-interface the spreading of an injected surfactant would proceed along this interface similar to the configuration discussed in the previous chapter. Specifically, in mixed-wet reservoirs the condition of a continuous interface between the aqueous-phase and the oil-phase in the reservoir will not be fulfilled. In this chapter experimental evidence will be presented that Marangoni driven transport of surfactants is not limited to continuous liquid interfaces. This novel phenomenon has not previously been described in literature. Besides the transport of surfactant the associated flows could be employed to deliver functional substances into previously inaccessible reservoir regions. These substances in turn can increase crude oil recovery rates^{94,150}, e.g. via wettability modification of the rock matrix.

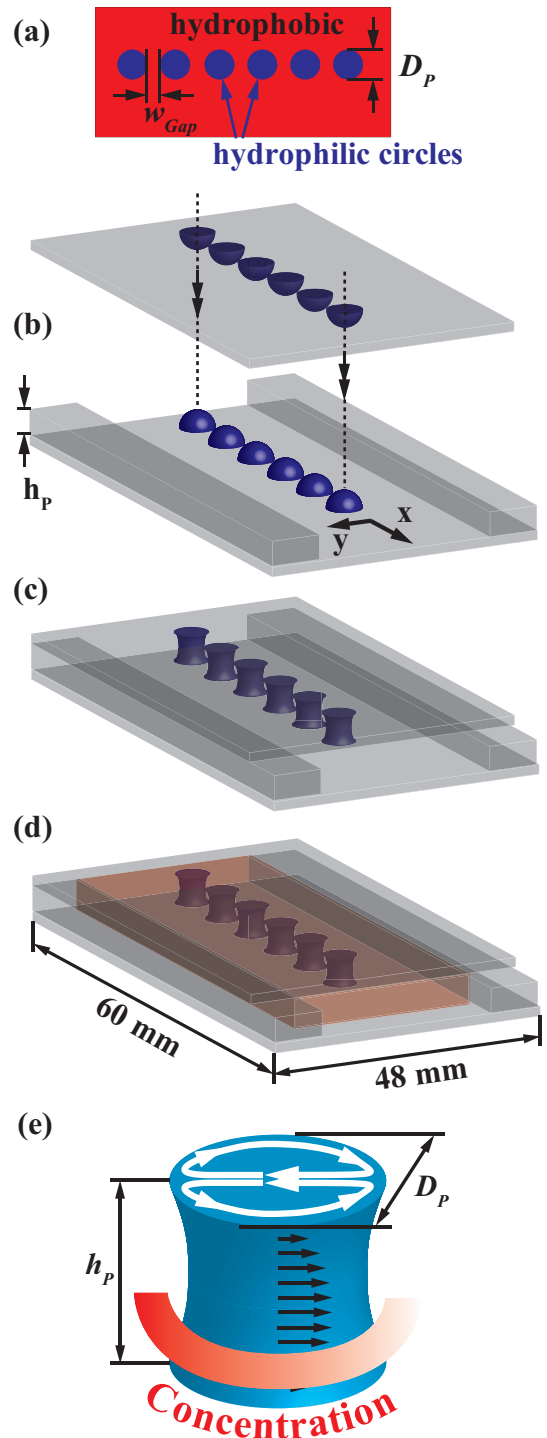
In the experimental model geometry used here, a discontinuous interface is implemented experimentally by using chemical surface patterns to confine an aqueous phase liquid to discrete locations inside a continuous oil-bulk-phase. In addition to the chemical surface patterns, both liquid-phases are confined between parallel plates reminiscent of a Hele-shaw-cell. In the following first the sample fabrication and the experimental layout will be described. Subsequently experimental results regarding the spreading of a surfactant in this system will be presented.

5.2 Sample fabrication and experimental setup

A top and bottom glass substrate are both chemically patterned with a linear array of hydrophilic circles with diameter D_P on a hydrophobic background. The individual circles are separated by a distance w_{Gap} as illustrated in Fig. 5.2(a). Chemical surface patterns were created via the same photolithography based procedure as in the previous chapters. Using a Hamilton micro-syringe, droplets of ethylene glycol (Sigma Aldrich, product number 324558, purity 99.8%) are deposited onto each of the hydrophilic spots, Fig. 5.2(b). Two glass spacers of thickness h_P are placed on both sides of the bottom substrate parallel to the droplet array. The distance between the droplet array and the spacers is approximately 10 mm, Fig. 5.2(b). As shown in Fig. 5.2(c), the top substrate is placed onto the spacers with the droplets facing downwards towards the bottom substrate. Upon contact the droplets on the two substrates merge and liquid pillars are formed. The final pillar height is determined by the thickness of the afore mentioned glass spacers h_P .

The resulting glass construction is clamped together using stainless steel clamps as in the experiments for continuous interfaces, described in section 4.2. The remaining cavity space is filled with dodecane, which has been purified using basic Aluminum oxide as described in section 4.2. The entire setup is placed above a light source providing homogeneous illumination. The intensity of the light transmitted through the sample is measured using a camera with a telecentric lens which mounted above the sample.

Figure 5.2: Sample preparation procedure for the study of surfactant transport along discontinuous liquid-liquid interfaces. (a) Chemical surface pattern on the top and bottom substrate. Both patterns consist of a linear array of hydrophilic circles with a diameter D_P on a hydrophobic background. The individual circles are separated by a distance w_{Gap} . (b) Ethylene glycol droplets are deposited onto the hydrophilic spots on the top and bottom substrate. Glass spacers of thickness h_P are placed on the bottom substrate on both sides of the droplet array. (c) The top substrate is placed onto the spacers, such that the droplet arrays on both substrates are aligned and the substrates are kept at a well-defined distance determined by the glass spacers. Upon contact with each other the droplets on the two patterned glass substrates merge and form liquid pillars. (d) The remaining cavity space is filled with dodecane, purified using aluminum oxide as described in Chapter 4. The dodecane is deposited at the opening of the cavity space and imbibes due to capillary action. (e) Qualitative sketch illustrating the Marangoni stress induced flow-field inside a pillar. Also sketched is the presumed qualitative concentration profile of surfactant along the interface.



A drop of a dyed surfactant solution in dodecane is deposited on one end of the immersed pillar array into the cavity space. The surfactant solution used in the experiments described here was a solution of 2 wt% Triton™ X-15 (Sigma Aldrich, product number X15-500ML) in dodecane, dyed with Oil Red O (Sigma Aldrich, product number O0625). Using a syringe filter, undissolved dye was removed to obtain a practically particle free solution. Due to the presence of the dye, the height-averaged spatial distribution of the surfactant front can be monitored through light absorption in a transmission configuration.

When the front of the injected surfactant solution reaches the first ethylene glycol pillar, its interfacial tension is locally reduced and the resulting interfacial tension gradients give rise to flow along and around its interface. In Fig. 5.2(e) a qualitative sketch of the flow-field inside a liquid pillar is shown alongside with the presumed concentration profile of the surfactant around the pillar. Figure 5.3 shows experimental images taken at different stages of this spreading process. The recorded grayscale images were inverted such that regions with a high surfactant (and dye) concentration appear bright. The deposited surfactant solution prior to contact with the first pillar ($t < 0$) is shown in

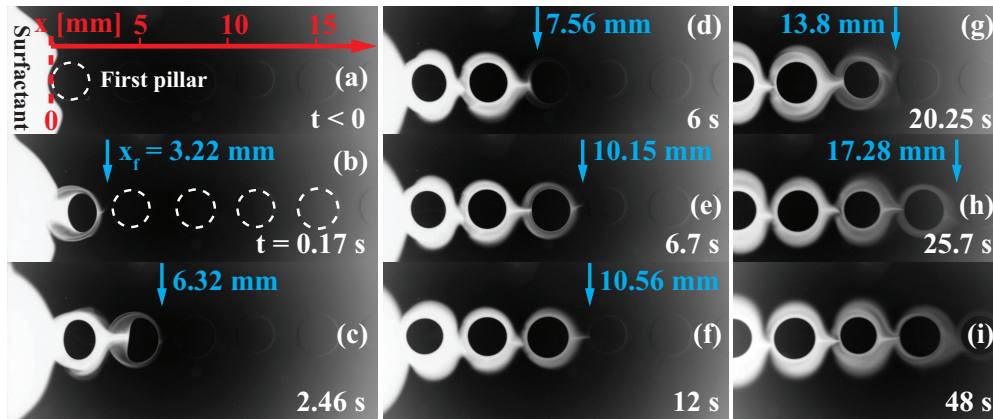


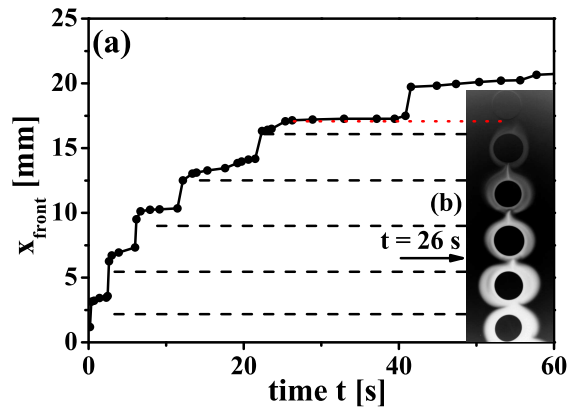
Figure 5.3: Contrast enhanced negative transmission images obtained at different stages during a spreading experiment with parameter values of pillar height $h_P = 450 \mu\text{m}$, nominal pillar footprint diameter $D_P = 3 \text{ mm}$ and gap width $w_{Gap} = 1 \text{ mm}$. After contact of the surfactant solution with the first pillar (indicated by the dashed white line in (a)), the leading edge of the front spreads from pillar to pillar. As the leading edge advances from pillar to pillar the concentration at the moving front progressively decreases along with the surfactant induced interfacial tension gradients on the pillar interfaces. As a consequence the front propagation slows down and the deformation of newly reached pillars is decreased. The convection around the pillars appeared to continue with decreasing intensity in the course of the experiments. A signature of this continued convection is the widening of the surfactant distribution around the pillars in the y -direction.

Fig. 5.3(a). Upon contact with the first pillar the surfactant solution is quickly spreading along its interface, Fig. 5.3(b). The Marangoni flow along the interface causes a complex flow-field in the surrounding oil-bulk-phase. The convected oil phase around the liquid pillar transports surfactant to the next liquid pillar with a clean interface, Fig. 5.3(c). The flow continues in this fashion and the surfactant is transported through the oil phase from one ethylene glycol pillar to the next, Fig. 5.3(d-i). This Marangoni driven transport process is many orders of magnitude faster than if diffusion would be the dominating mechanism behind the transport. In the course of this spreading process, the concentration of the surfactant front reaching the new pillars decreases and the surfactant induced Marangoni stresses drop correspondingly. In the images of Fig. 5.3, the dark regions at the location of the pillars are the smallest diameter along the height of the pillars. In most cases the lenses had a slightly concave shape, i.e. the pillar volume was chosen slightly below the volume of a cylinder with equivalent foot-print.

5.3 Transport rate

Figure 5.4(a) shows the position of a propagating surfactant front as a function of time for pillars of height $h_P = 450 \mu\text{m}$, a nominal diameter of the pillar footprint $D_P = 3 \text{ mm}$ and a gap width $w_{Gap} = 1 \text{ mm}$. The step-wise appearance of the propagation data is a result of the strongly differing propagation rates of the surfactant front along the pillar interfaces and across the gaps between neighboring pillars. Along the pillar interface the propagation proceeds rapidly compared to the propagation through the gaps. Across the gaps the propagation occurs through convection of surfactant-rich oil-bulk-phase due to the velocity field decaying from the pillar interface into the oil-phase. An experimental image of the spreading process at $t = 26 \text{ s}$ is shown in Fig. 5.4(b) in the same scale as the ordinate axis in (a). The dashed black lines indicate the positions of the pillars, the front position at $t = 26 \text{ s}$ is indicated by the red dotted line. Figure 5.5 shows

Figure 5.4: (a) Surfactant front position as a function of time, for $h_P = 450 \mu\text{m}$, $D_P = 3 \text{ mm}$ and $w_{Gap} = 1 \text{ mm}$. The step-wise propagation is caused by the different propagation rates along the pillar interfaces and across the gaps between neighboring pillars (b) Experimental image ($t = 26 \text{ s}$) in the same scale as the ordinate axis in (a), the pillar positions are highlighted by the dashed black lines. The red dotted line marks the front position in the image.



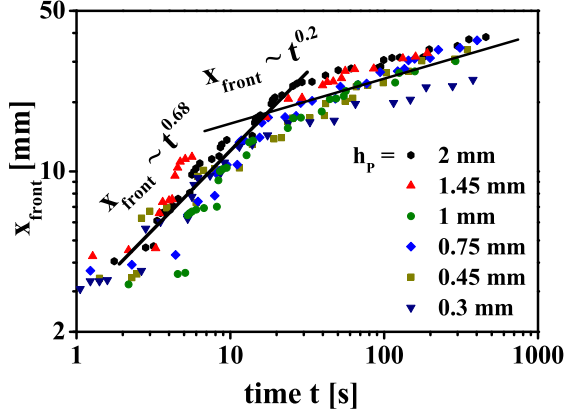


Figure 5.5: (a) Surfactant front position as a function of time, for $D_P = 3$ mm and $w_{Gap} = 1$ mm and a variety of pillar heights h_P . Due to the log-log scale the step-wise nature of the propagation is less apparent than in Fig. 5.4(a). The propagation can initially ($t \lesssim 20$ s) be approximated by $x_{front} \sim t^{0.68}$, and in a later stage ($t \gtrsim 20$ s) by $x_{front} \sim t^{0.2}$.

surfactant front positions as a function of time, for a variety of pillar heights h_P . The footprint diameter and the gap width were kept constant at $D_P = 3$ mm and $w_{Gap} = 1$ mm, respectively. The data suggest that the initial phase of the spreading, $t \lesssim 20$ s, can be approximated by $x_{front} \sim t^{0.68}$. In later stages the spreading appears to decrease in speed and the data in Fig. 5.5 is well approximated by $x_{front} \sim t^{0.2}$. The change in the spreading exponent from 0.68 to 0.2 suggests a qualitative change in the spreading conditions. We currently speculate that the saturation of the first pillar volume with surfactant could be responsible for such a transition. Once the bulk of a pillar is saturated with surfactant, desorption of surfactant from the liquid-liquid interface ceases. This desorption can, until pillar saturation, support an interfacial tension driven flow around a pillar since the interface is depleted of surfactant and interfacial tension gradients due to spatially varying adsorption from the surrounding oil bulk can be maintained.

Considering the data shown in Figure 5.5, the spreading seems to be only minutely influenced by the pillar height for the parameter range investigated.

5.4 Pillar deformation

During the initial stage of the spreading, the interfacial tension gradients, induced by the non-uniform surfactant distribution on the pillar interface, are sufficiently large to result in a strong deformation of the pillar shape. Snapshots of such a deformation, typically observed on the first 3 to 4 pillars, are shown in Fig. 5.6. In the first image ($t = 2.29$ s) the surfactant front has just reached the second pillar. The cross-section of the waist of the pillar is indicated by the white dashed circle in Fig. 5.6(a).

Highlighted in blue in Fig. 5.6(b) is the footprint area of the second pillar, which is clearly visible at $t = 2.46$ s due to the surfactant solution that spread along the entire pillar surface. Furthermore, a strong deformation of the pillar shape is evident. At $t = 3.17$ s the pillar center section has practically again assumed a circular shape, as the initially strong gradients in the surfactant distribution on the pillar surface have decreased.

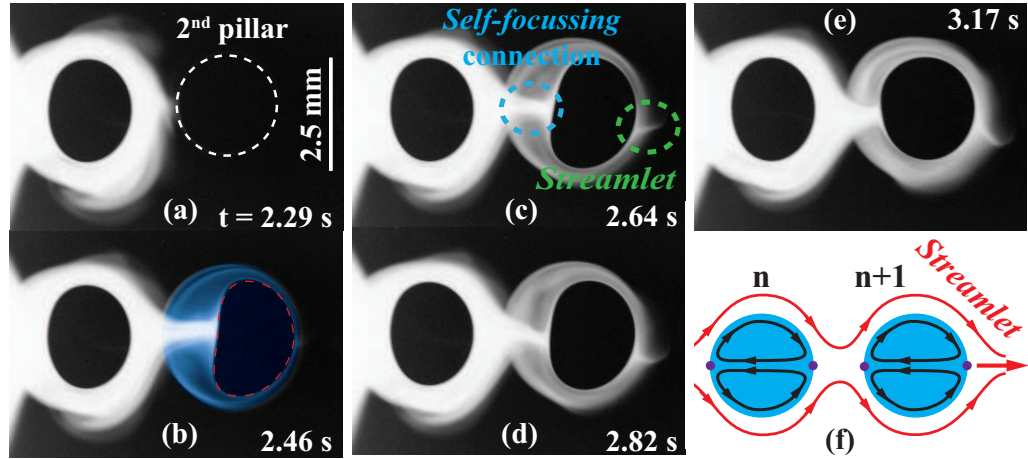


Figure 5.6: Strong deformation of the second pillar waist section in a spreading experiment with a pillar height $h_P = 450 \mu\text{m}$, nominal pillar footprint diameter $D_P = 3 \text{ mm}$ and gap width $w_{\text{Gap}} = 1 \text{ mm}$. At $t = 2.29 \text{ s}$ the surfactant front reached the second pillar. The pillar cross section at its waist is indicated by the white dashed line in (a). Shortly after contact of the surfactant front with the pillar midsection, the footprint area of the second pillar is clearly visible in (b), highlighted in blue. Due to the non-uniform distribution of the surfactant on the pillar surface the shape of the pillar is strongly distorted from its equilibrium shape. This is clearly visible by the off-centered non-circular cross-section of the pillar waist section as indicated in (b) by the red dashed curve. The initially strong gradients in the surfactant distribution on the pillar surface quickly decrease and the pillar center section assumes an approximately circular shape, (e). (f) Qualitative sketch of the convection pattern in and around the two pillars just behind the surfactant front. The purple points represent stagnation points in the flow field.

Short after initial contact of the surfactant front with the second pillar, a *streamlet* of surfactant rich oil phase formed at the distant edge of the pillar, as marked by the green dashed oval. These *streamlets* of surfactant rich oil are also visible in the experimental images in Fig. 5.3. They are forming as a consequence of the convection pattern in and around the pillars (qualitatively sketched in Fig. 5.2(e) and Fig. 5.6(f)) which is convergent near the proximal and extensional near the distal stagnation points.

When these *streamlets* reach adjacent pillars, Marangoni flows are induced in the latter as a consequence of the locally high surfactant concentration. The resulting flow-field in the surrounding oil-bulk-phase facilitates a *self-focussing* of the surfactant rich connection between the pillars. This *self-focussing* connection is indicated in Fig. 5.6(c). Considering the flow-field around a pillar pair as sketched in Fig. 5.6(f) the mechanism behind the *self-focussing* can be rationalized as the flow-field behind pillar n converging towards a single line, the previously described *streamlets*. Once the surfactant rich oil reaches the pillar $n+1$ the same convection pattern in and around the pillar forms as for

pillar n . As a consequence, the *streamlet* formation in pillar n is enhanced since the right side of pillar n , close to pillar $n+1$, is depleted of surfactant. This depletion causes an ongoing flow around the interface of pillar n . Once the surfactant front has reached pillar $n+2$ the same chain of events follows with the effects reaching back the entire array of pillars.

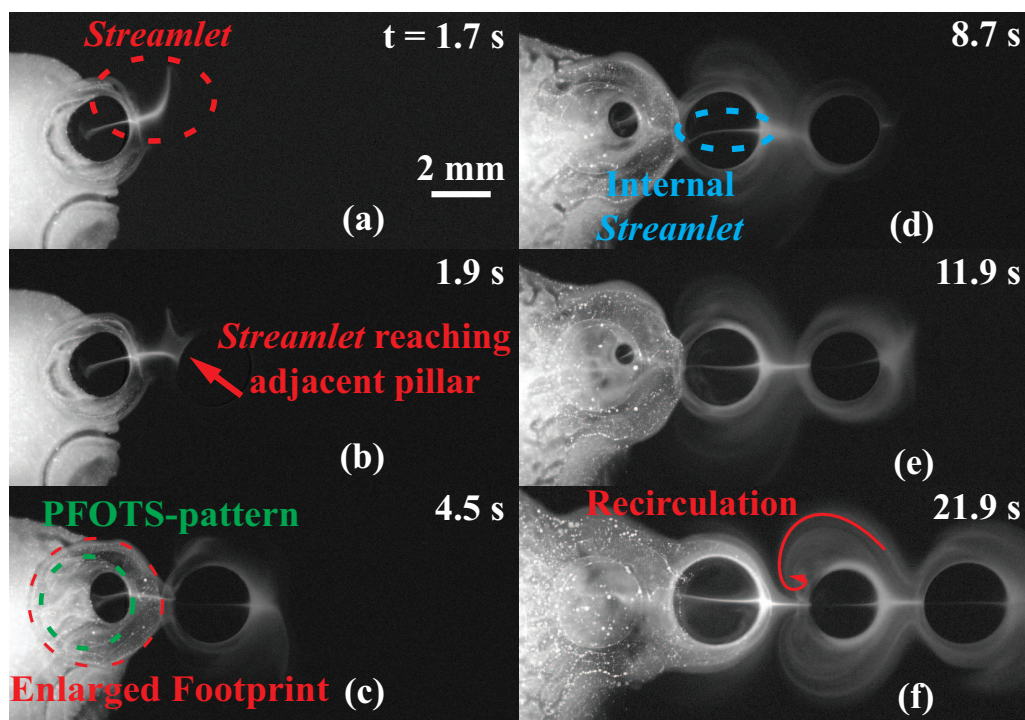


Figure 5.7: Spreading of TritonTM X-45 alongside with wettability modification induced snap-off of the pillar initially contacted by the surfactant solution. The transmission images were inverted, contrast enhanced and background corrected. The same characteristic *Streamlet* formation at the distal stagnation point of the pillars was observed as for TritonTM X-15 and is highlighted in image (a). Due to higher solubility of TritonTM X-45 and dye entrainment, internal *Streamlets* are also visible, as indicated in (d). In image (c) the presumed foot-print area is indicated via the red dashed line. As a result of wettability modification of the PFOTS-treated region the footprint has significantly enlarged from the $D_P = 3$ mm, originally imposed by the PFOTS-pattern indicated in (c) by the green dashed line. The spreading of the pillar liquid onto the formerly non-wetting region continued and the liquid on the top- and bottom-substrate eventually disconnect at $t \approx 12.7$ s. The waist diameter of the second pillar appears to have increased between $t = 11.9$ s and $t = 21.9$ s, i.e. from image (e) to (f). This is presumably caused by absorption of liquid from pillar 1 that has reached pillar 2.

5.5 Low partitioning coefficient surfactant

In first qualitative experiments a similar spreading behavior as described above was observed for experiments conducted with TritonTM X-45 instead of TritonTM X-15. TritonTM X-45 (Sigma Aldrich, product number X45-100ML) is a surfactant of the same type as TritonTM X-15 with an increased length of the hydrophilic polyethylene oxide chain. This increase in the length of the hydrophilic chain can be expected to increase the solubility of TritonTM X-45 in the ethylene glycol compared to TritonTM X-15. Corresponding experimental images are shown in Fig. 5.7. In the shown experiment Sudan Black (Sigma Aldrich, product number 199664) was used to stain the surfactant solution, furthermore the concentration of the surfactant was 5 wt%. This exceeded the solubility limit and dispersed surfactant droplets were present in the deposited surfactant solution. These droplets contained increased quantities of the dye which caused the grainy appearance and the occurrence of the bright spots in the inverted experimental transmission images in Fig. 5.7. A qualitative difference in these experiments relative to TritonTM X-15 shown in Fig. 5.3 was that the flow inside the pillars behind the surfactant front was more pronounced. A signature of this continued flow around the first pillars in the array is a recirculatory flow pattern as indicated in Fig. 5.7(f). We speculated that the higher polarity of the TritonTM X-45 increases its desorption rate into the pillars which depletes the surfactant concentration at the interface. This depletion of the interface allows flow from the surfactant rich region to continue for a longer period of time than in the case of TritonTM X-15. An indication for the increased dissolution of the TritonTM X-45 is the entrainment of dye into the pillars which reveals their internal flow field. As a consequence of this entrainment internal *Streamlets* were observed in these experiments, indicated in Fig. 5.7(d). This entrainment phenomenon was completely absent in the TritonTM X-15 experiments, e.g. Fig. 5.6.

An additional effect associated with the use of TritonTM X-45 is wettability modification of the substrate regions that were initially non-wetting for the ethylene glycol. This is observed primarily in regions of high surfactant concentration, i.e. in the region of initial surfactant deposition. The ethylene glycol of the first pillar spread from its originally confining hydrophilic circle onto the PFOTS regions. The footprint of the first pillar is indicated in Fig. 5.7(c) by the red dashed line while the hydrophilic circle in the PFOTS-pattern is indicated in green. As a consequence of the enlarged footprint area the pillar waist diameter decreased and eventually the liquid on the bottom- and top-substrate disconnected at $t \approx 12.7$ s.

5.6 Discussion and outlook

The existing literature on surfactant spreading considers exclusively continuous interfaces. The spreading of surfactants has been investigated at the interface between air and deep^{18,36,37,47,66,72,141} as well as thin^{11,51,52,57,73,133,134,142,143} liquid layers. Recently

Berg⁹ has presented the first study of surfactant spreading between two deep liquid layers. This work has been extended towards the spreading between thin liquid films in the previous chapter.

In this chapter it was shown for the first time that surfactant induced Marangoni flows can also transport surfactant along *discontinuous* liquid-liquid interfaces. This was demonstrated for spreading of a mainly oil-soluble surfactant along a line array of pillars of a polar liquid immersed in a continuous oil-phase. The surfactant is propagated by the Marangoni-stress induced flow field in the continuous phase. This flow field is a consequence of the surfactant induced flows along the interfaces of the individual pillars.

This newly discovered phenomenon is directly relevant when considering the spreading of surfactants in an oil reservoir. Under reservoir conditions a continuous interface between the oil-phase and an aqueous phase in the reservoir is, dependent on conditions, unlikely to be given over long distances. Although the experiments shown here were conducted in systems with ethylene glycol pillars, the same spreading was observed analogously along arrays of water pillars immersed in dodecane in proof of principle experiments, i.e. a material combination resembling potential reservoir conditions. However, ethylene glycol offers the advantage of a low volatility facilitating sample preparation.

The variation of the surfactant is a promising way to examine the role of surfactant transport from the location of initial deposition towards the leading edge. If this transport is more pronounced, as in the case of the TritonTM X-45, experiments then the propagation rate of the surfactant front is likely to be boosted. The notion that desorption of surfactant from the pillar interface into its bulk is necessary for pronounced spreading is supported by the fact that a solution of 2 wt% of oleic acid in dodecane does not spread along an array of water pillars with a distance of $w_{Gap} = 1$ mm. In the experiments with oleic acid, the surfactant solution spread rapidly around the first pillar but the flow seized in a fraction of a second without transporting sizable amounts of surfactant through the oil-bulk-phase surrounding the pillar. As a consequence the consecutive pillars were not reached by the surfactant solution. Oleic acid and water is a model system for an insoluble surfactant. While TritonTM X-15 is claimed to be insoluble in water by the manufacturer, we presume it is slightly soluble in ethylene glycol and water, resulting in the, to oleic acid, qualitatively different spreading behavior.

In future experiments the role of the spatial dimension of the presented flow problem should be investigated. It would be of interest to systematically vary the pillar height to lower values than the ones presented up to now, specifically when regarding spreading under reservoir conditions where the encountered film thicknesses might be significantly lower. To determine the influence of the pillar spacing would also be of interest, i.e. how large the extend of the interface discontinuities can be such that surfactant can still be transported effectively. A variation in the pillar diameter and hence the pillar volume offers could offer conclusions regarding the importance of surfactant desorption into the pillars.

Chapter 6

Self-sustained drop motion

The physicochemical hydrodynamics underlying the self-sustained motion, or self-propulsion, of droplets and small solid objects have received considerable attention in recent years. Famous examples include the motion of water droplets on surfaces exhibiting a wettability gradient as predicted by Greenspan⁵⁵ and first demonstrated by Chaudhury²¹, the reactive flow of drops containing a wettability modifying substance demonstrated by Bain⁸ and of course the famous camphor boats, extensively studied amongst others by Nakata et al^{98,100,102,104,107,108,111,112,115,116}. Most of the existing literature on self-sustained droplet motion reviewed in chapter 1 is concerned with the the propulsion on solid substrates or deep liquid layers. In this chapter a system will be examined in which surfactant droplets undergo an autonomous motion on thin liquid sub-phase films. These sub-phase films are confined by chemical surface patterns, prescribing the path of the droplets. As will be shown in the next chapter, this droplet motion also offers interesting applicational aspects with respect to lab-on-a-chip technology. Here a systematic investigation of different propulsion conditions and their influence on the propagation of the droplets is presented. Amongst others the ratio of droplet size and sub-phase film thickness will be shown to have a pronounced influence on the propulsion behavior. The drop dynamics were investigated using interference microscopy. Fluorescence microscopy was applied to characterize the sub-phase morphology evolution in the vicinity of the moving droplets. Experimental initial and boundary conditions were varied and various modes of motion were identified.

6.1 Sample preparation

Using photolithography and self-assembling mono-layers of 1H,1H,2H,2H-perfluorooctyltrichlorosilane, as previously described¹³⁴, chemically patterned surfaces with hydrophilic stripes of different widths w and length L on a hydrophobic background were created. Single-side polished Si wafers (n -type doped with Ph) were used as substrates in interferometry experiments. When fluorescence microscopy was applied, rectangular

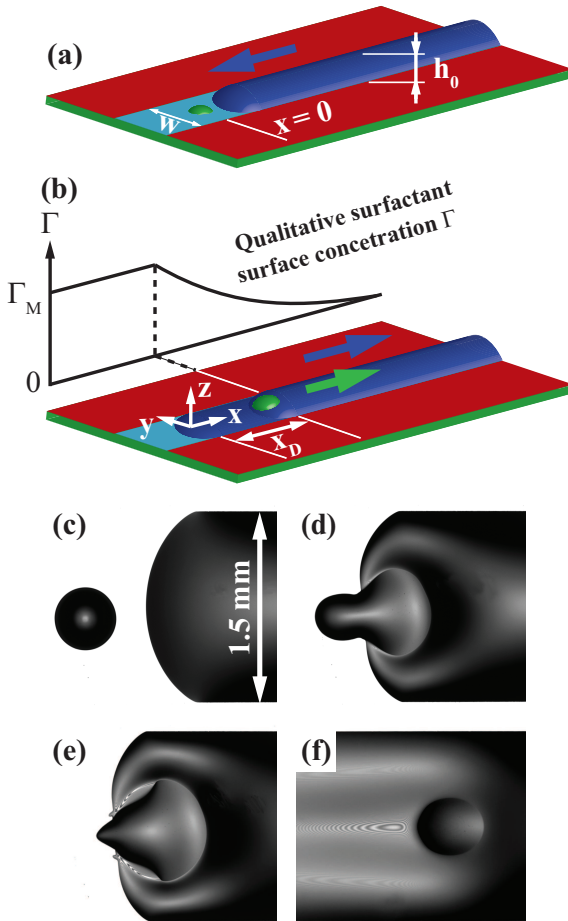
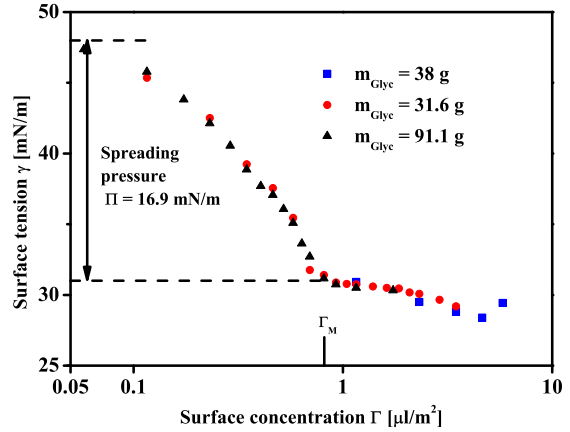


Figure 6.1: a) Sketch of the sub-phase film (blue, center thickness h_0), deposited ahead of the droplet, advancing towards the surfactant droplet (green) due to capillary pressure and gravity. b) Sketch of a droplet at position x_D propelling along the sub-phase rivulet. The hypothesized surfactant surface concentration Γ of the sub-phase is qualitatively illustrated. Behind the droplet the surface can be assumed to be covered by a dense mono-layer of the surfactant ($\Gamma = \Gamma_M$). Ahead of the droplet the surfactant spreads along the rivulet surface towards regions of low surface concentration. The consequence is a concentration gradient ahead of the droplet associated with Marangoni flow of the sub-phase in the direction of droplet motion. Experimental images of a droplet, c) prior to, d+e) during mobilization ($t = 0.1$ s and $t = 0.2$ s after contact) as well as f) during propulsion ($t = 45$ s) along the rivulet.

borosilicate glass microscope cover slides (Gold Seal, product number 3334) with a thickness between 0.13-0.17 mm were used as substrates. Prior to patterning and experiments the substrates were cleaned using Piranha, a 1:1 mixture of hydrogen peroxide (J.T. Baker, product number 7047, 30%) and sulfuric acid (J.T. Baker, product number 6057, 95%). Droplets (10-60 nl) of the surfactant cis-9-octadecen-1-ol (oleyl alcohol, Sigma O8880, 99% purity) were deposited on one edge of the hydrophilic stripe using a thin glass fiber or a Hamilton 7000.5SN micro-syringe as a dip-pen. A thin film (center thickness h_0), or rivulet of the subphase liquid, a solution of 0.55 wt% sodium-dodecylsulfate (SDS, Aldrich product number 71727, purity 99%) in anhydrous glycerol (Aldrich, product number 49767, purity 99%) was then manually deposited on the remaining hydrophilic region using a Hamilton 1710RN gastight micro-syringe. A small area around the surfactant droplet was excluded, i.e. left dry.

Following the deposition of the droplet and the sub-phase rivulet onto the hydrophilic stripe, capillary pressure and gravity cause the contact line of the sub-phase liquid to ad-

Figure 6.2: Sub-phase surface tension γ_{S-Air} as a function of oleyl alcohol surface concentration, measured using a Wilhelmy-plate. Γ_M indicates the concentration at which a dense mono-layer covers the surface. Indicated is also the spreading pressure $\Pi = \gamma(\Gamma = 0) - \gamma(\Gamma_M)$.



vance towards the surfactant droplet. The corresponding sketch and experimental image are shown in Fig. 6.1 a) and c) respectively. Experiments were monitored using an Olympus BX-51 upright microscope with passband-limited illumination with various center wavelengths. When the advancing rivulet comes in contact with the surfactant droplet ($t = 0$) at its initial position $x = 0$, two main effects are observed, 1) surfactant induced Marangoni flow in the sub-phase and 2) mobilization and self-propulsion of the droplet along the rivulet. The initial propulsion or mobilization of a droplet is shown in the experimental images Fig. 6.1 (d,e) for $t = 0.1$ s and $t = 0.2$ s, after initial contact respectively. A strong deformation from a circular footprint of the droplet is evident in these images. This deformation reduces over time and the droplet propels along the rivulet assuming an elliptical footprint as shown in Fig. 6.1 f) for the droplet at $t = 45$ s. The droplet width was measured after the initial strong deformation has decayed and the footprint is elliptical. Associated with the propulsion is a strong thinning of the rivulet behind the advancing droplet as shown by the interference fringes in the experimental images in Fig. 6.1 e) and f).

The droplet motion occurs alongside a Marangoni flow in the sub-phase caused by the high concentration of surfactant at the interface around the droplet. The interfacial concentration is decreasing ahead of the droplet, whereas behind the droplet the rivulet interface can be assumed to be covered by a dense mono-layer of surfactant. The gradient in the surfactant surface concentration induces a gradient in surface tension which gives rise to the sub-phase flow¹³⁴. This flow facilitates the spreading of a sub-mono-layer of surfactant along the rivulet ahead of the propelling droplet. The presumed surface concentration profile is illustrated qualitatively in Fig. 6.1 b) alongside with the monitored drop position x_D .

6.2 Interfacial tension measurements, material parameters

Figure 6.2 shows the dependence of the sub-phase surface tension on the surface concentration of oleyl alcohol. A mixture of hexane and oleyl alcohol was deposited onto different bulk amounts of subphase, denoted by the different symbols in Fig. 6.2, while the surface area of the sub-phase was kept constant. Upon evaporation of the hexane only the oleyl alcohol was left on the surface and a constant value for the surface tension γ_{S-Air} was measured using a Wilhelmy plate. For equal amounts of deposited surfactant, the surface tension was the same for the different amounts of sub-phase showing that the droplet surfactant is insoluble in the sub-phase. An initial steep decrease in surface tension with increasing surface concentration is followed by a quasi plateau region. This quasi plateau region is an indication of a dense mono-layer covering the surface, indicated in Fig. 6.2 by Γ_M . The difference in surface tensions of a clean interface and an interface covered by a dense mono-layer is termed the spreading pressure of the surfactant $\Pi = \gamma(\Gamma = 0) - \gamma(\Gamma_M)$.

An equilibrium value of $\gamma_{D-S} = 3.8 \frac{\text{mN}}{\text{m}}$ was measured for the liquid-liquid interfacial tension between the sub-phase and the droplet surfactant using a pendant drop tensiometer.

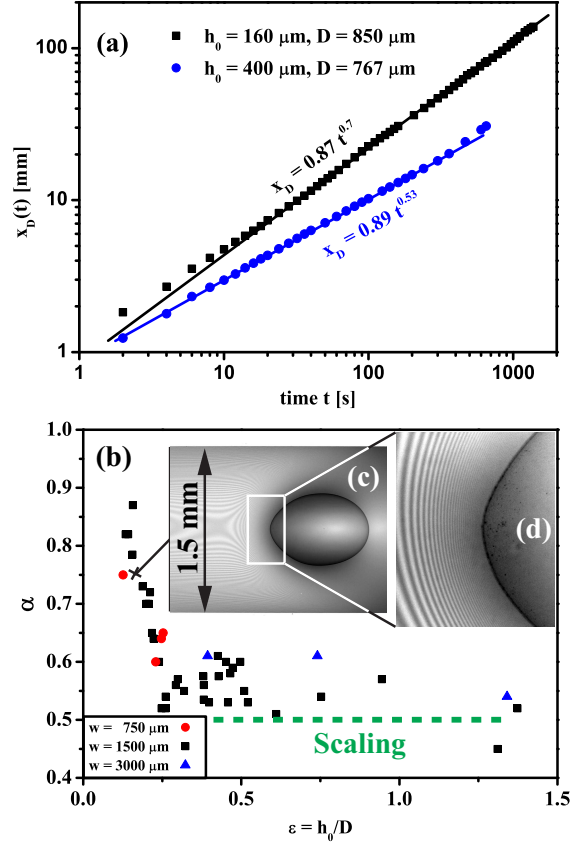
At 25°C, the temperature at which most of our experiments were conducted, we measured the viscosity of the pure subphase $\mu_S = 866 \text{ Pa s}$ using a Brookfield DV-II+ Pro viscosimeter. This is in agreement with literature values for pure glycerol, with a density of 1260 kg/m^3 and a refractive index $n_{\text{gly}} = 1.47$. The surface tension of oleyl alcohol was measured as $\gamma_{D-Air} = 32 \frac{\text{mN}}{\text{m}}$ via pendant drop tensiometry, its density is given in literature as 895 kg/m^3 , i.e. significantly lower than the density of the sub-phase.

6.3 Drop propagation

The position of the moving droplets x_D was measured as a function of time t , as shown in Fig. 6.3 (a). For the experiments shown, the droplet widths were $D = 767 \mu\text{m}$ and $850 \mu\text{m}$ for propulsion on sub-phase films of thickness $h_0 = 400 \mu\text{m}$ (blue circles) and $160 \mu\text{m}$ (black squares), respectively with a rivulet width of $w = 1.5 \text{ mm}$. For both cases shown, a power-law of the form $x_D = \beta t^\alpha$ approximates the experimentally measured dynamics very well. The propulsion exponents α of the two droplets are $\alpha = 0.53$ and $\alpha = 0.7$.

The propulsion exponent α depends on the ratio ϵ between film thickness of the subphase h_0 and the droplet width D as shown in Fig. 6.3 b). Propulsion exponents as a function of ϵ , are shown for rivulets of width $w = 0.75 \text{ mm}$ (red circles), 1.5 mm (black squares) and 3 mm (blue triangles). For values of $\epsilon \geq 0.25$, the exponents appear to be constant with a value of slightly above $\alpha \approx 0.5$. For lower values of, $\epsilon \leq 0.25$, i.e. thinner films or larger drops, the propulsion exponents increase significantly with the highest measured values around $\alpha \approx 0.9$, i.e. motion with almost constant velocity.

Figure 6.3: a) Drop positions x_D as a function of time for two propelling droplets. Striking is the difference in propulsion exponent $\alpha = 0.53$ and 0.7 for the different ratios $\epsilon = \frac{h_0}{D} = 0.52$ and 0.19 respectively. b) Propulsion exponents α for a range of ϵ . The exponents appear to be constant or independent of ϵ for $\epsilon \geq 0.25$. For smaller values of ϵ , a steep increase in the measured exponents is evident, with the highest values of $\alpha \approx 0.9$ which represents motion with an almost constant speed. The green dashed line indicates an exponent $\alpha = 0.5$. c) Interference microscopy image (illumination $\lambda = 750$ nm) of a propelling droplet with $\epsilon \approx 0.17$. d) Magnified view of the back of the droplet. The decreasing fringe spacing towards the droplet clearly indicates a steepening of the sub-phase profile towards the droplet.



In Fig. 6.3 c) an interference image (illumination center wavelength $\lambda = 750$ nm) of a droplet with $\epsilon \approx 0.17$ is shown. The fringes give an indication of the sub-phase topography around the drop. Considering the decreasing fringe spacing towards the back end of the drop, shown in a magnified fashion in Fig. 6.3 d), a steepening of the sub-phase profile towards the droplet is evident. An analysis of the sub-phase configuration around the droplet using interference microscopy is only feasible in the back of the droplets, where the sub-phase film has significantly thinned.

6.4 Sub-phase mapping via fluorescence microscopy

To obtain information about the sub-phase thickness profile around the entire perimeter of the droplet inverted fluorescence microscopy was employed. For these experiments $0.1 \text{ wt}\%$ of fluorescein sodium salt was added to the sub-phase and transparent glass substrates used with a pattern width of $w = 750 \mu\text{m}$. The fluorescence intensity was correlated to film thickness by calibration via a rivulet of sub-phase with a known

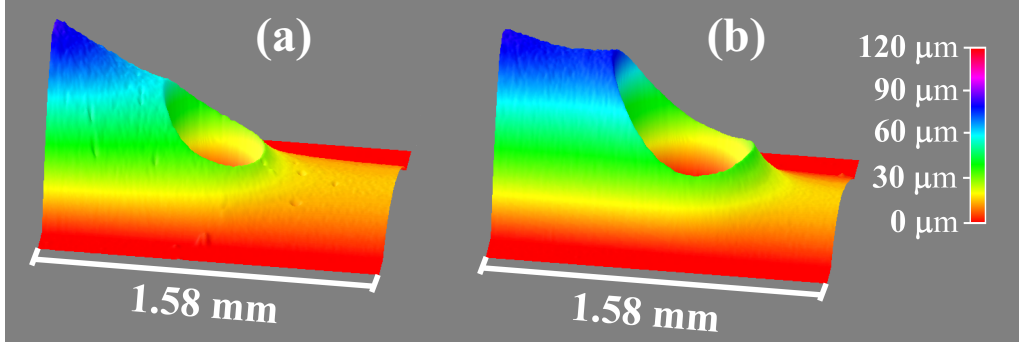


Figure 6.4: (a,b) show color-coded contour plots of the sub-phase topography around propelling droplets with $D = 410 \mu\text{m}$ and $D = 530 \mu\text{m}$ on films of initial film heights $h_0 = 135 \mu\text{m}$ and $h_0 = 70 \mu\text{m}$, respectively and a pattern width of $w = 0.75 \text{ mm}$. Iso-height values are color-coded according to the legend on the right.

morphology. The obtained relation between fluorescence intensity and sub-phase morphology allows a conversion of the recorded 2-D intensity maps into 3-D contour plots. Figures 6.4 (a,b) show color-coded contour plots of the sub-phase topography around propelling droplets with $D = 410 \mu\text{m}$ and $D = 530 \mu\text{m}$ on films of initial film heights $h_0 = 135 \mu\text{m}$ and $h_0 = 70 \mu\text{m}$, respectively and a pattern width of $w = 0.75 \text{ mm}$.

6.5 A scaling argument for the drop propulsion

Under certain assumptions a scaling argument can be given for the propulsion of the droplets

Assuming the droplet to move proportional to the Marangoni flow of the sub-phase at its position, $\frac{\delta x_D}{\delta t} u(x = x_D)$, and the front position of the spreading surfactant layer ahead of the droplet x_F to propagate with, $\frac{\delta x_F}{\delta t} = u|_{z=h_0}(x = x_F)$, i.e. with the surface velocity at its position. Considering only viscous friction and a therefore linear velocity profile in the sub-phase and the surfactant induced surface tension gradient as a driving force, the front propagation scales as,

$$\frac{\delta x_f}{\delta t} \sim \frac{\Pi h_0}{\mu} \frac{1}{x_f - x_D}, \quad (6.1)$$

since at the front position the film thickness is always the undisturbed initial film thickness h_0 . An analogous argument can be applied for the position of the drop by replacing h_0 with an effective film thickness h_e that is the length scale characterizing the viscous stress at the position of the droplet.

$$\frac{\delta x_D}{\delta t} = \frac{\Pi h_e}{\mu} \frac{1}{x_f - x_D} \quad (6.2)$$

Here Π denotes the spreading pressure of the droplet surfactant. The distance between droplet and front is then given by subtracting eq.(6.2) from eq.(6.1) and subsequent integration considering $(x_f - x_D)(t = 0) = 0$.

$$x_f - x_D = \sqrt{\frac{2\Pi(h_0 - h_e)t}{\mu}} \quad (6.3)$$

inserting 6.3 into 6.2 and integration gives

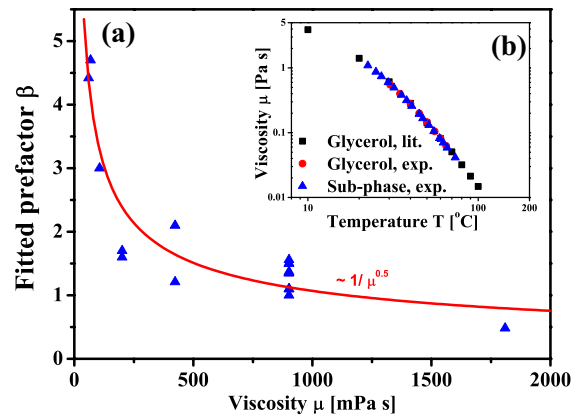
$$x_D = \frac{\Pi h_e}{\mu} \frac{2\sqrt{t}}{\sqrt{\frac{2\Pi(h_0 - h_e)}{\mu}}} = \sqrt{2\frac{\Pi}{\mu}} \frac{h_e}{\sqrt{h_0 - h_e}} \sqrt{t} \quad (6.4)$$

The expected propulsion exponent is therefore $\alpha = 0.5$ which coincides well with the experimentally observed values for $\epsilon \geq 0.25$. An extend analysis of the sub-phase configuration elucidating also the influence of the capillary pressure on the propelling droplet could potentially lead to a conclusive reason for the increase in the spreading exponent for lower aspect ratios.

6.6 Viscosity modulation

In order to vary the velocity of the self-propelling droplets, the modulation of the sub-phase viscosity offers an efficient possibility¹³². The viscosity of both sub-phase and droplet decreases with increasing temperature. In Fig. 6.5 b) the temperature dependence of the sub-phase viscosity is shown and coincides with literature values for pure glycerol. Within the studied range of viscosities, no qualitative difference in the propulsion behavior was found, i.e. the measured range of exponents for the initial film thickness of $h_0 = 250 \mu\text{m}$ was $0.53 \leq \alpha \leq 0.6$. Figure 6.5 a) shows the effect of the subphase viscosity on the pre-factor β fitted to the experimental data. The red solid line in Fig.

Figure 6.5: (a) Influence of the temperature modulated sub-phase viscosity on the propulsion dynamics. The pre-factor β is approximately inversely proportional to the square root of the sub-phase viscosity. (b) Sub-phase viscosity dependence on temperature, coinciding with literature values for pure glycerol.



6.5 a) corresponds to the relation $\beta \sim 1/\mu^{0.5}$ as expected from the scaling argument Eq. (6.4) and is a good approximation of the experimental data.

6.7 Meandering motion

In all the propulsion experiments discussed up to now, the initial conditions were as shown in Fig. 6.1, i.e. a drop was placed on a hydrophilic stripe, a rivulet of sub-phase material was advancing towards it and upon contact the droplet would slide onto the rivulet and propel along its length. As a result, the droplets propelled along the center-line of the sub-phase rivulets. Under different initial conditions the droplets can exhibit a meandering motion as shown in Fig. 6.6(d-o). In this experiment a droplet of the insoluble surfactant was deposited onto a rivulet of glycerol with initial height $h_0 \approx 400 \mu\text{m}$ and length $L = 40 \text{ mm}$ at an off-center position approximately 7 mm from one edge of the rivulet. The surfactant used in this experiment was oleic acid (Sigma O1008, 99% purity), which is chemically very similar to the previously used oleyl alcohol and exhibits the same propulsion behaviour for experimental conditions as described in section 6.3.

Upon deposition of the surfactant onto the rivulet liquid, the droplet split and a resulting daughter droplet initially propelled towards the nearby longitudinal edge of the rivulet. Associated with the deposition of the surfactant onto the rivulet was an initial Marangoni driven flow of sub-phase bulk liquid away from the location of deposition. Due to the small distance of $\approx 7 \text{ mm}$ between the end of the rivulet and the deposition site and the rather high sub-phase film thickness $h_0 \approx 400 \mu\text{m}$, the surfactant front, spreading away from the droplet, can be expected to have reached the end of the rivulet within several seconds. Once the surfactant front has reached the edge of the rivulet the surfactant surface concentration gradient $\partial\Gamma/\partial x$ and the associated surface tension gradient $(\partial\gamma/\partial\Gamma)(\partial\Gamma/\partial x)$ ahead of the droplet decreased due to accumulation of surfactant between the droplet and the edge of the rivulet. As a consequence, the Marangoni flow of sub-phase away from the droplet diminished and was offset by capillary and hydrostatic pressure driven flow of sub-phase liquid from the rivulet edge, where liquid had accumulated as a consequence of Marangoni flow, towards the droplet as indicated in Fig. 6.6(e). Under these conditions, the droplet engaged in a meandering motion against the main direction of the bulk flow which has never been reported in the scientific literature before. This propulsion behavior can be explained qualitatively considering the flow field of the sub-phase bulk around the droplet. When bulk liquid is flowing past the droplet on the negative y -coordinate part of the rivulet (Fig. 6.6(d-g)) the sub-phase surface is locally expanding due to spatial velocity gradients, $\Delta A/A \sim \partial u_x/\partial x \Delta t$. This expansion goes along with a local decrease in surfactant surface concentration $\Delta A/A \sim \Delta\Gamma/\Gamma$. The droplet propels towards regions of low surfactant surface concentration or high bulk flow rates and associated strong interface expansion. As the droplet propels in negative y -direction, the flow of sub-phase decreases since the presence of the droplet causes a thinning of the film surrounding it and is associated with sub-phase flow in the direction

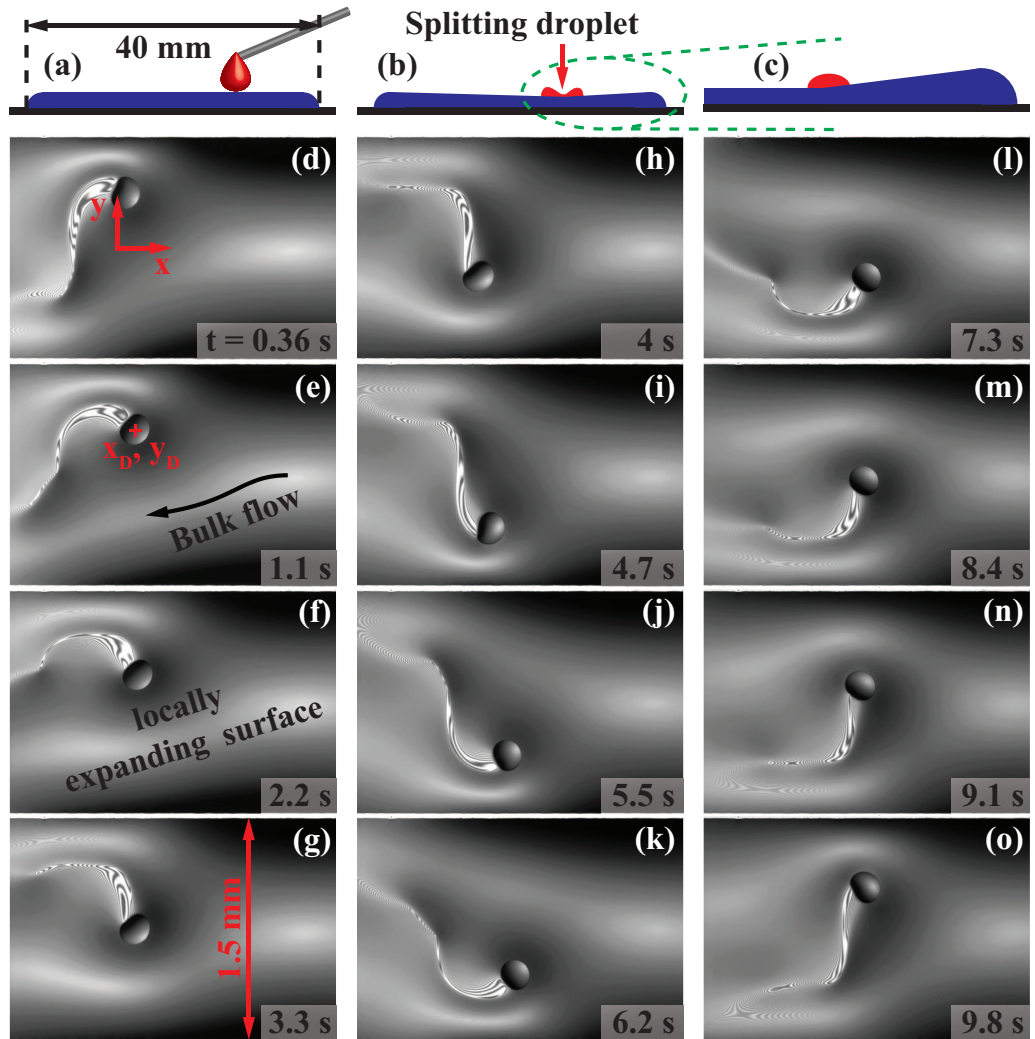


Figure 6.6: Interference microscopy images (illumination center wavelength $\lambda = 650$ nm) of a droplet undergoing a meandering motion. After off-centered initial deposition of an oleic acid droplet on a glycerol rivulet, the droplet split and a resulting daughter droplet propelled towards the end of the rivulet in a meandering motion as shown in (d-o). Due to capillary pressure the sub-phase exhibited a bulk-flow in negative x -direction, indicated in (e). This sub-phase flow, subject to flow rate modulation by the meandering droplet, is associated with a surface expansion, due to velocity gradients, that effectively reduces the surfactant surface concentration.

of drop motion. As the droplet approaches the rivulet border at $y = -0.75$ mm the sub-phase film ahead of it saturates with surfactant, since the chemical patterning imposes a no-flux boundary condition on the sub-phase and the surfactant at $y = -0.75$ mm. However since the droplet moved in negative y -direction, sub-phase began to flow in negative x -direction past it on the positive y -half of the rivulet Fig. 6.6(i-m). This in turn caused a decrease in local surfactant surface concentration on this rivulet section due to the local surface expansion causing the droplet to change from a translation with negative velocity in y -direction v_y to a positive v_y . The described interplay of surfactant surface concentration decreasing sub-phase flow past the droplet and spreading of surfactant from the droplet alongside its translational motion gives rise to the meandering propulsion characterized by a varying net motion in x -direction and an oscillating velocity component in y -direction with no net translation.

In Fig. 6.7(a) the x - and y - positions x_D and y_D of the droplet center as indicated in Fig. 6.6(e) are shown as a function of time in black and red respectively. x_D is increasing over time with short periods in which $\partial x_D / \partial t < 0$. In contrast, y_D is oscillating between $-0.4 \text{ mm} < y_D < 0.4 \text{ mm}$. The velocities of the droplet in x - and y -direction v_x

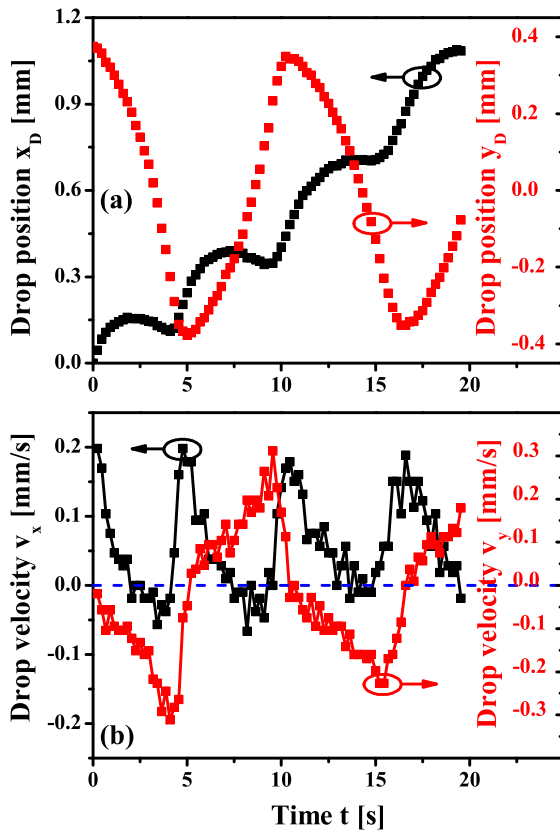


Figure 6.7: (a) Droplet center positions in x - and y -direction (left and right ordinate, respectively) along the x - and y -axes shown in Fig. 6.6(d) as a function of time. The y -position y_D is oscillating around an average value of $y_D = 0$ while the x -position exhibits a net increase. (b) Velocity components v_x and v_y in x - and y -direction (left and right ordinate, respectively) measured during the meandering propulsion. The scatter of the data is mainly due to discretization effects involved with the determination of the droplet center position.

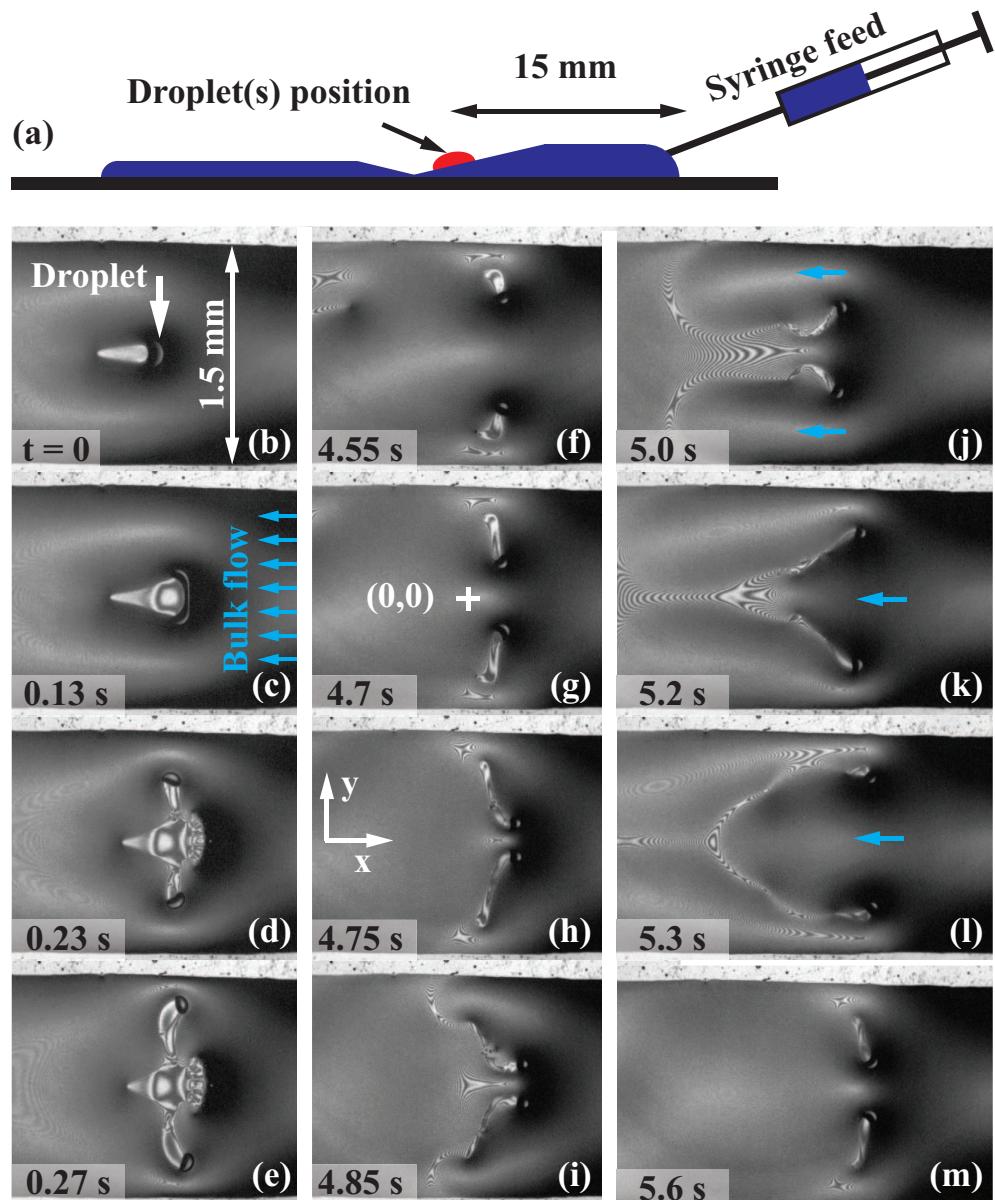


Figure 6.8: Optical interference images showing the break-up of a single droplet and the synchronized meandering motion of the two resulting daughter droplets against the bulk flow of the sub-phase. Bulk flow was induced by manual supply of sub-phase ahead of the droplet. The addition of sub-phase liquid resulted in the creation of surfactant free sub-phase surface ahead of the droplet and a bulk flow due to capillary pressure towards the droplet. As a consequence of a maximum in the flow rate of bulk supply, the initially single droplet (b) split (c) and the resulting two daughter droplets exhibited a synchronized meandering motion.

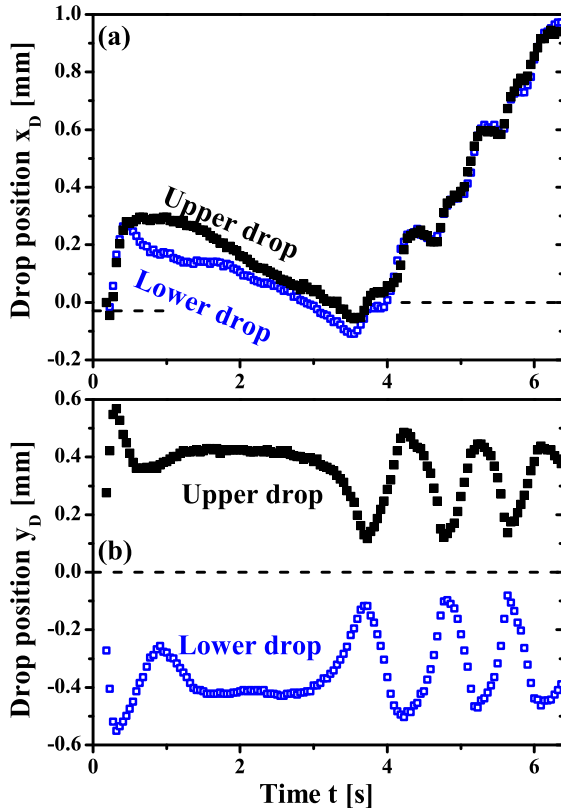


Figure 6.9: (a) Positions x_D of the droplets shown in Fig. 6.8(d-m) in x -direction. Directly after breakup of the original droplet, the two daughter droplets were initially convected with the sub-phase flowing in negative x -direction. With the onset of the meandering motion at $t \approx 3.5$ s the droplets exhibited a net motion in x -direction. (b) y -positions y_D of the droplets as a function of time. The trajectory of y_D for $t > 3.5$ s for the two drops resembles the data presented in Fig. 6.7(a) for a single droplet, with the difference that each of the droplet undergoes an oscillatory motion in its respective half of the rivulet.

and v_y are shown in Fig. 6.7(b) in black and red, respectively. The periods of $v_x < 0$ correspond to the times when the droplet is passing the centerline of the rivulet, i.e. as the droplet center position is around $y_D = 0$.

A pair of droplets engaged in the described meandering propulsion can undergo a synchronized motion. Experimental images of such a synchronized behavior are shown in Fig. 6.8(f-q). A single droplet was deposited onto a rivulet of glycerol with a water content of 10 wt% and the same sub-phase liquid was manually supplied via a glass pipette as shown in Fig. 6.8(a). Upon exceeding a certain threshold of the sub-phase flow rate, the droplet, previously being practically stationary in the flow of supplied sub-phase, extended in transversal direction and split, Fig. 6.8(b-e). Two resulting daughter droplets subsequently engaged in synchronized motion. In reference to the coordinate system shown in Fig. 6.8(g) the position of both droplets in x -direction x_D is shown in Fig. 6.9(a) as a function of time. After an initial steep increase, x_D slowly decreased, i.e. the droplets were convected with the sub-phase flow. This was followed by a forward motion in x -direction of both droplets that is reminiscent of the afore described motion of the single meandering droplet shown in Fig. 6.7(a). This forward motion started simultaneously with the oscillating motion in y -direction. The respective position of

the droplets in y -direction y_D are shown in Fig. 6.7(b) in black and blue for the upper and the lower droplet, respectively. The resemblance of the shown curve for $t > 3$ s with the data presented Fig. 6.7(a) is evident, with the difference that each of the individual droplets is exhibiting the meandering motion in their respective half of the rivulet. As explained above, the approach of a droplet to the border of the chemical surface pattern at $y = \pm 0.75$ mm goes along with an accumulation of surfactant ahead of the droplets due to the no flux boundary condition the border of the chemical pattern imposes on the surfactant and the sub-phase. This causes the droplet to change direction and to propel with a reversed sign of v_y . The approach of the droplets with each other has a similar effect since both droplets are sources of surfactant spreading along the sub-phase surface. Therefore, as the two droplets approach each other, the surfactant surface concentration between them increases. Since the droplets move towards regions of low surface concentration they eventually change the sign of their respective v_y and move away from each other towards the edges of the rivulet at $y = \pm 0.75$ mm, where sub-phase flow gradients have extended the surface and hence the surface concentration has decreased. These regions of high sub-phase flow rates are indicated in Fig. 6.8(j) by the light blue arrows. Analogously, as the droplets move apart sub-phase begins to flow in negative x -direction between the droplets as indicated by the blue arrows in Fig. 6.8(k,l). This in turn decreases the surfactant concentration in the center of the rivulet and the droplets eventually move towards the center again and the cycle restarts.

In summary, the described meandering motion of a single droplet as well as the synchronized motion of a droplet pair are a result of a complex interplay of surfactant spreading from the droplet, the influence of the related surfactant concentration gradients on the sub-phase flow and vice versa and the influence of the confinement due to the chemical surface patterning.

6.8 Intermittent propulsion

In Section 6.6 the effect of a viscosity reduction by means of a temperature increase on the propulsion speed was presented. Due to the uniform heating of the entire experimental setup in these measurements, the viscosity of the droplets also decreased. If the sub-phase viscosity is reduced by addition of water, the droplet viscosity remains unchanged and the viscosity ratio between subphase and droplet is modulated. For addition of up to 15 wt% DI-water the effect is practically equivalent to the viscosity modulation via temperature. At 15 wt% DI-water content and above, the droplets frequently broke up during mobilization. In this type of system sufficiently small droplets, however, i.e. with a footprint of ≤ 100 μm exhibited an *in the existing literature undescribed* intermittent mode of self-propulsion. In the measurements described here a sub-phase of glycerol with a 15 wt% DI-water content and the insoluble surfactant oleic acid (Sigma O1008, 99% purity) were used. As in the experiments described in Section 6.3 a surfactant droplet was placed onto one end of a rivulet with length 40 mm while the sub-phase liq-

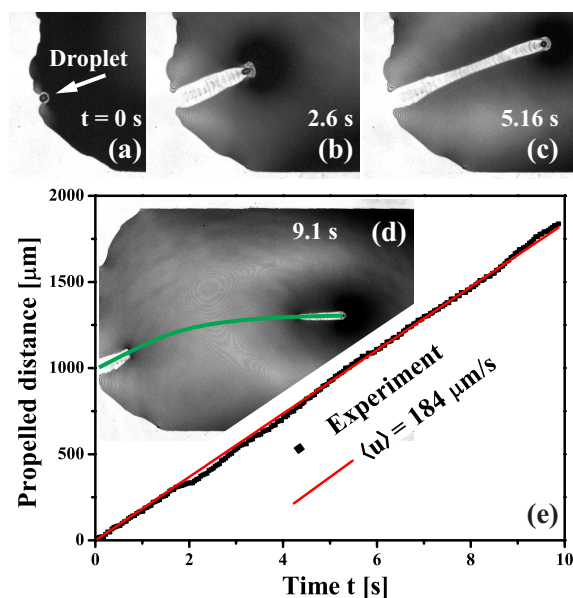


Figure 6.10: (a-c) Droplet in intermittent propulsion mode at $t = 0$ s $t = 2.6$ s and $t = 5.16$ s respectively. (d) Droplet position at $t = 9.1$ s. The green line shows the trajectory of the droplet from its initial position to the point when it has been completely consumed. (e) Propelled distance over time. The experimental data (symbols) is well approximated with a linear velocity of $184 \mu\text{m/s}$. Even though the drop decreases in volume over time its speed remains constant allowing the conclusion that the speed is independent of its size.

uid was deposited at the other end. The droplets engaged in self-propulsion upon contact of the sub-phase with the advancing sub-phase. Due to the abrupt nature of this intermittent propulsion mode, only sufficiently small droplets (footprint of $\leq 100 \mu\text{m}$) engaged in this type of propulsion. Larger droplets broke up upon contact with the sub-phase and the sub-phase surface was due to this break-up largely saturated with surfactant.

Experimental images of the intermittent propulsion are shown in Fig. 6.10 (a-d) for the droplet at times $t = 0$ s, $t = 2.6$ s, $t = 5.16$ s and $t = 9.1$ s respectively. When the droplet began to propel, it initially moved along the gradient of the height profile and then continued along the rivulet centerline where the sub-phase film thickness is highest. The trajectory of the droplet is indicated in Fig. 6.10 (d) by the green solid line. The initial motion towards the center of the rivulet is followed by a straight motion along the rivulet centerline. In Fig. 6.10 (d) the sub-phase has already started to flow back onto the former path of the droplet. For this intermittent mode, the time averaged propelled distance increases linearly with time as shown in Fig. 6.10 (e). A constant time averaged speed of $\langle u \rangle = 184 \mu\text{m/s}$ is a good approximation of the experimental data. The fact that the propelling droplet is depleted in the course of the experiment yet its speed remains constant during the experiment allows the conclusion that the droplet size is not a determining factor for the speed in this propulsion mode.

Figure 6.11(a-l) shows high resolution images illustrating the mechanism of the intermittent propulsion. When the droplet is in contact with the sub-phase ($t = 0$ ms, (a)) it begins to slide onto the sub-phase layer ahead of it ($t = 10$ ms, (b)) and moves forward. At $t = 10$ ms the triple line of the droplet is not clearly visible. Since the droplet consists of a surface active substance the rivulet interface around it is immediately covered by a

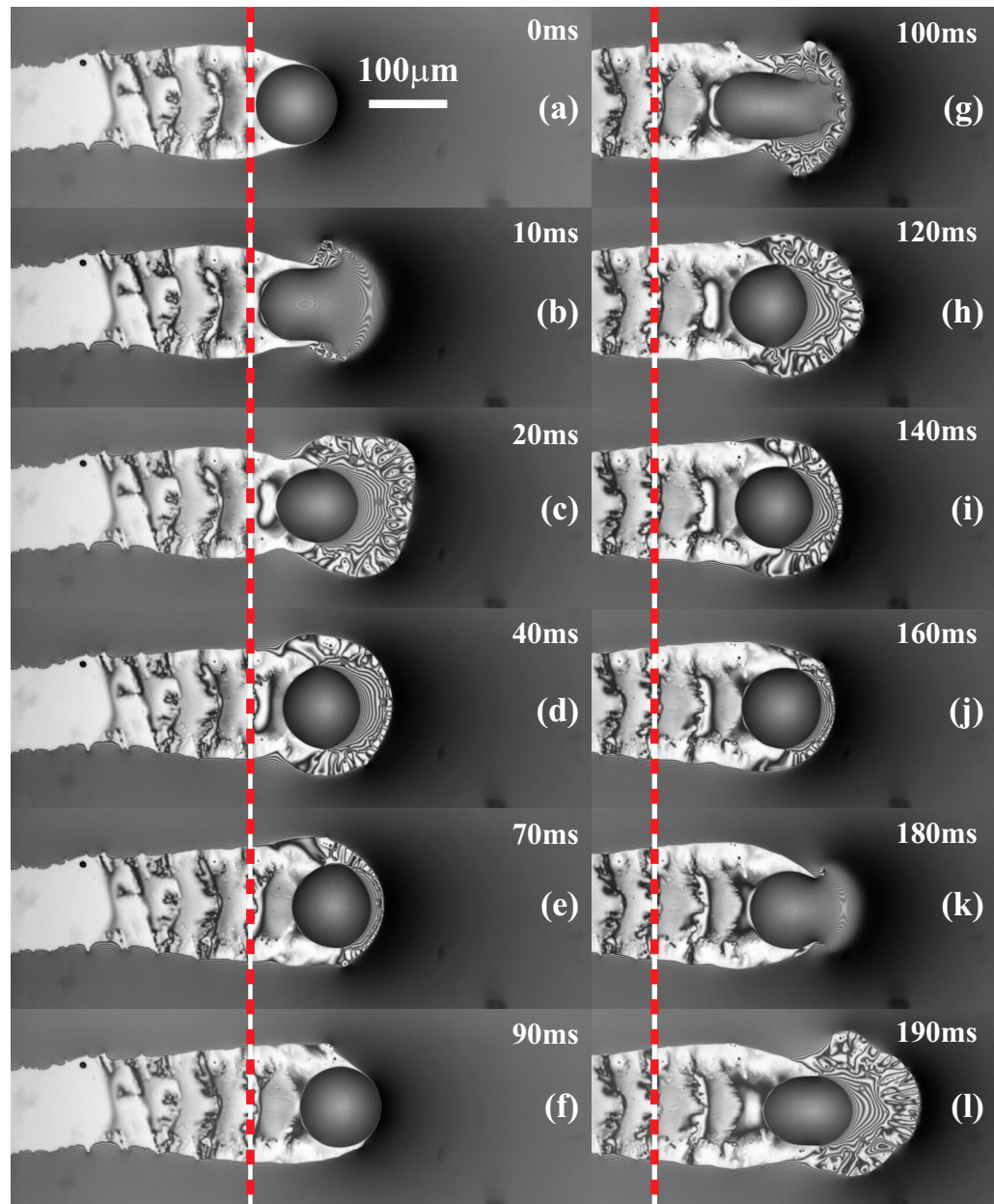


Figure 6.11: Series of interference microscopy images of a micro-droplet engaged in an intermittent mode of propulsion. (b) and (k), droplet in contact with the sub-phase bulk, it is impossible in these images to detect the triple line of the surfactant droplet. (c-e), (h-j) and (l), droplet gradually moving forward on the thin sub-phase film left behind by the retracting sub-phase bulk. (c,h,l) sub-phase in its most retracted state. (g) droplet in the moment of detachment from the sub-phase bulk.

dense mono-layer of the surfactant, leading to a strong localized reduction of its surface tension. The consequence of this local reduction in surface tension around the drop are strong gradients in surface tension giving rise to sub-phase flow away from the drop. Due to the low viscosity of the sub-phase (15 wt% DI-water) this retracting flow exceeds the speed with which the droplet is sliding onto the rivulet such that the droplet does not engage in a continuous motion as discussed in Section 6.3. This step is shown in Fig. 6.11 at $t = 10$ ms,(b), $t = 100$ ms,(g) and $t = 180$ ms,(k). Instead of the sliding on as in the continuous propulsion, the sub-phase ahead of the drop thins significantly leaving behind only a film of thickness $\approx 1 \mu\text{m}$ around the drop. This thin film is clearly visible by the interference fringes in the experimental images in Fig. 6.11. The thickness of this film increases towards the drop, where the sub-phase forms a meniscus with the contact line of the droplet elevating it from the substrate. Due to the curvature of the meniscus, capillary pressure causes the droplet to slide forward slowly ($t = 20$ ms to 70 ms, Fig. 6.11(c-e) and $t = 120$ ms to 160 ms Fig. 6.11(h-i)). The meniscus in the front of the droplet is clearly visible as well as the absence of such a meniscus in the back of the drop. The high surface concentration of the surfactant on the film that had contact with the droplet quickly redistributes over the entire length of the rivulet such that the overall surface concentration is diluted towards a low level. The sub-phase film then flows back towards the drop due to the capillary and hydrostatic pressure which is no longer overcome by the surfactant-induced surface tension gradients. Once the sub-phase has reached the droplet again, the process starts over until the entire droplet is depleted.

The entire process is therefore alternating between relatively fast drop motion following the contact of the drop with the sub-phase, Fig. 6.11(b,g,k), $t = 10$ ms, $t = 100$ ms and $t = 180$ ms and a slower motion as the drop is pulled forward by the negative capillary pressure due to the curved sub-phase meniscus left behind by the retracting sub-phase, $t = 20$ ms to 70 ms, Fig. 6.11(c-e) and $t = 120$ ms to 160 ms Fig. 6.11(h-i).

6.9 Summary and conclusions

Several newly discovered modes of self-sustained motion exhibited by insoluble surfactant droplets on thin liquid sub-phase films have been described in this chapter. The sub-phase films were confined by chemical surface patterns.

For the presented continuous mode of straight propulsion, the experimentally measured drop position was found to follow a powerlaw $x_D \propto \beta t^\alpha$. A systematic investigation of the propulsion conditions on viscous sub-phase films revealed two regimes with different propulsion exponents. When the droplet size exceeded a certain threshold compared to the initial sub-phase film thickness a pronounced increase of the propulsion exponents α was found, while the exponents appear constant for droplet sizes below that threshold. Fluorescence microscopy was employed to analyze the sub-phase topography around the droplets. When the sub-phase viscosity is strongly reduced by a change in its com-

position, leaving the drop viscosity unaltered, an intermittent mode of drop motion was discovered.

Note: The results presented in this chapter have in parts been presented in the 2012 *Small matters* video contest by the American Institute of Physics (AIP). The contribution was selected the contest winner by the Editorial Advisory Board of *Biomicrofluidics*.

Chapter 7

Self-propelling surfactant droplets in chemically-confined microfluidics

In the previous chapter it was shown that droplets of certain insoluble surfactants can exhibit self-sustained motion on a chemically confined sub-phase, provided suitable asymmetric initial conditions. The focus of chapter 6 was on the propulsion behavior and the different modes of motion depending on the experimental conditions. In this chapter, certain application related aspects in open-surface microfluidic devices are investigated for these self-propelling droplets.

Open-surface microfluidic devices offer certain advantages over conventional pressure-driven, channel-based microfluidic systems, such as easy access, but also suffer from draw-backs, e.g. the incompatibility with operation by mechanical pumps²⁰. Established liquid actuation techniques in open-surface microfluidic devices are optowetting⁶⁹, dielectrophoresis⁷⁷, thermocapillary actuation^{30,31,122}, and vibration²⁷ as well as electrowetting^{1,85,95,121}, which has recently also been applied in open/closed-surface hybrid devices². Specifically with respect to cheap, single-use-type devices, a drawback of these techniques is the necessity of an external power source and the integration of electrodes or electric heating elements into the microfluidic system. A viable alternative for these kind of devices are passive liquid actuation mechanisms, which have been demonstrated for closed^{10,88,124,147} as well as open-surface microfluidic devices²⁰.

This chapter illustrates the applicability of surfactant self-propulsion as a passive driving mechanism for droplets in chemically-confined microfluidics, eliminating the necessity of an externally powered actuation mechanism. The droplets, consisting of an insoluble surfactant, exhibit directed motion on thin films of a second liquid, termed sub-phase. These sub-phase layers are spatially confined by chemical surface patterns, forming fluidic pathways for the self-propelling droplets. The novel concept of using passively moving droplets to transport solid cargo particles is presented here. The cargo hereby is of a size comparable to the droplets themselves. Furthermore, it will be demonstrated that at fluidic junctions in the chemical patterning the droplets can be either split

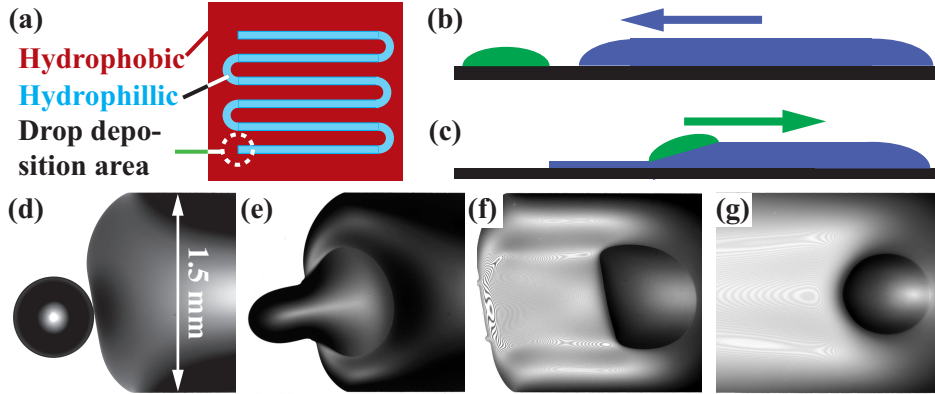


Figure 7.1: (a) Sketch of a typical hydrophobic/hydrophilic surface pattern. (b+c) Illustration of the mobilization of a droplet, (b) the sub-phase liquid spreads towards the droplets due to capillary pressure, (c) the droplet is in contact with the sub-phase, is mobilized, and propels along the confined sub-phase film. (d-g) Different stages in a propulsion experiment with initial film thickness $h_0 = 295 \mu\text{m}$. (d) Droplet ($V_D \approx 19 \text{ nl}$) prior to contact with the advancing sub-phase rivulet. (e) Droplet $\approx 0.1 \text{ s}$ after contact with the sub-phase, in the process of getting mobilized. (f,g) Droplet in an early ($t = 1 \text{ s}$) and later stage of the propulsion ($t = 77 \text{ s}$). The initially nearly half circular shape quickly relaxes towards a circular one.

or their trajectory can be controlled using thermal routing. The driving force for the droplet motion has its origin in the Marangoni-flows induced by the non-uniform surfactant distribution around the droplets. Related propulsion mechanisms for drop transport along liquid-air²³ as well as liquid-solid interfaces¹³⁹ have been studied in recent years.

7.1 Experimental details

The chemical patterning procedure, based on photolithography and self-assembling mono-layers of 1H,1H,2H,2H-perfluorooctyltrichlorosilane was described in detail in chapter 3, along with the subsequent cleaning step. Using this procedure chemically patterned surfaces on Si-substrates and borosilicate glass slides (thickness $150 \mu\text{m}$), with hydrophilic stripes of length $L \geq 220 \text{ mm}$ and width $w = 1.5 \text{ mm}$ on a hydrophobic background were created, as sketched in Fig. 7.1(a).

For experiments without cargo, a droplet of the surfactant cis-9-octadecen-1-ol (oleyl alcohol) is deposited on one edge of the hydrophilic region using a glass fiber as a dip-pen. The droplet volumes V_D in the experiments ranged from 4-60 nl. After droplet deposition, the sub-phase liquid (film thickness h_0), a 0.55 wt% solution of sodium

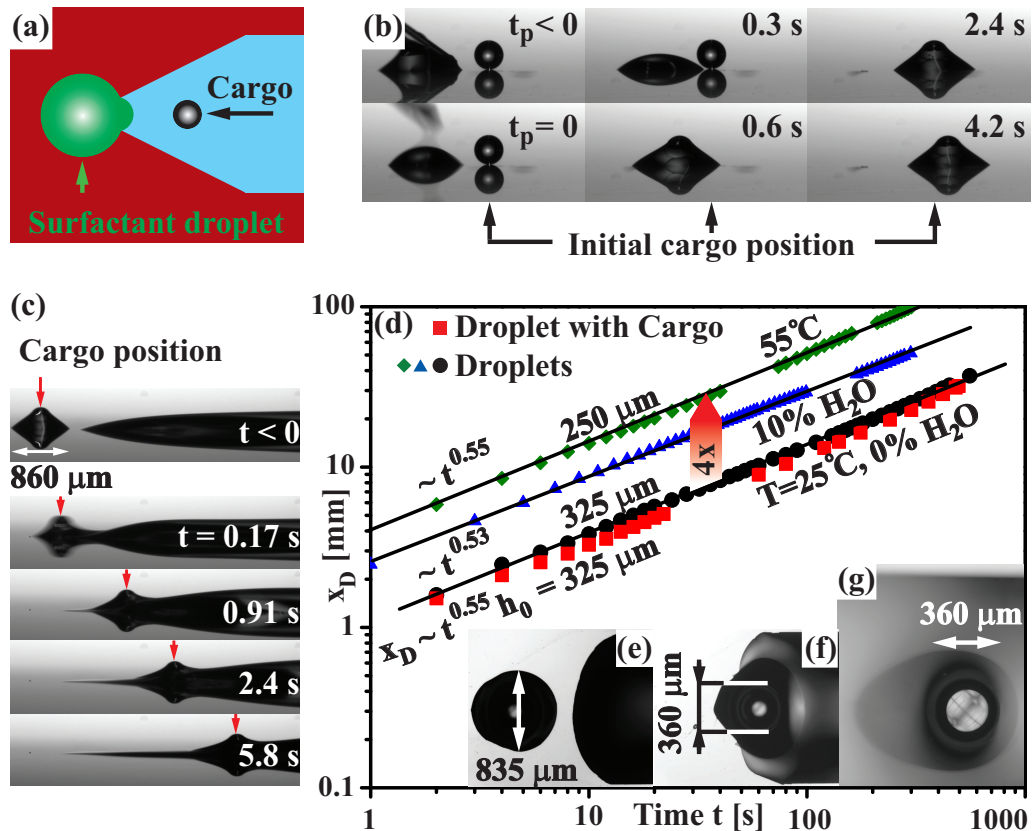


Figure 7.2: (a) Sketch of the surface pattern used for cargo loading, prior to sub-phase deposition. A droplet deposited on the tip of the hydrophilic wedge propels forward towards the cargo due to the increasing hydrophilic surface area covered by it. (b) Experimental images of the cargo pick-up, taken with a telecentric lens in a side-view configuration. The initial cargo position is indicated by the black arrows on the bottom. (c) Mobilization and propulsion of a particle transporting droplet. The cargo position in the micrograph sequence is indicated by the red arrows. (d) Droplet position as a function of time for a droplet and a particle transporting droplet indicated by the black circles and red squares respectively. Also shown, data for drop propulsion on sub-phase liquid with viscosities reduced by increased temperature (green diamonds) and 10 wt% DI-water addition (blue triangles). (e-g) top-view images of a particle transporting droplet, (e) prior to mobilization, (f) during mobilization, (g) propelling with the particle.

dodecyl sulfate (SDS) in anhydrous glycerol, is evenly distributed on the remaining hydrophilic region using a Hamilton 1710RN gastight micro-syringe, excluding a small area around the surfactant droplet.

Following deposition, the contact line of the sub-phase liquid advances towards the

surfactant droplet due to capillary spreading, as illustrated in Fig. 7.1(b). When the advancing sub-phase rivulet comes in contact with the surfactant droplet ($t = 0$), the latter is mobilized and slides onto the rivulet, as shown in Fig. 7.1(c,e). Subsequently, the surfactant droplet self-propels along the rivulet, whereby strong film-thinning behind the advancing droplet is evident. Optical micrographs of droplet mobilization and self-propulsion along a chemically confined sub-phase film ($h_0 = 295 \mu\text{m}$) are shown in Fig. 7.1(d,e) and (f,g), respectively. The experiment was monitored using an Olympus BX-51 upright microscope, with the illuminating light passband-limited around a center wavelength of $\lambda = 650 \text{ nm}$ with a bandpass of $\Delta\lambda \approx 10 \text{ nm}$.

Fig. 7.2(d) shows the position x_D of a droplet ($V_D \approx 23 \text{ nl}$) as a function of time t for propulsion on a sub-phase film of thickness $h_0 = 325 \mu\text{m}$ (black circles). To very good approximation the dynamics are described by a power-law of the form $x_D = t^{0.55}$.

As illustrated in Fig. 7.2(d), the propulsion speed can be adjusted by modulating the sub-phase viscosity. Experimental data is shown for an experiment at 55°C (green diamonds, $V_D \approx 9 \text{ nl}$) and at 25°C with 10 *wt%* of DI-water added to the sub-phase (blue triangles, $V_D \approx 13 \text{ nl}$), resulting in viscosities of 105 mPa-s and 152 mPa-s respectively (original sub-phase viscosity $\mu_{sub}(25^\circ\text{C}) = 870 \text{ mPa-s}$). In both cases the observed propulsion speed is strongly increased, while $x_D(t)$ remains well approximated by a power-law of the form $x_D = t^{0.55}$.

7.2 Cargo loading and transport

The self-propelling droplets can be used to transport solid cargo particles. In the experiments described here, poly-methyl-methacrylate (PMMA) beads (Altuglass, density = 1.19 kg/m^3) were used as a model cargo. In Fig. 7.2(a) a chemical surface pattern is sketched that facilitates controlled pickup of a cargo particle by the droplets. Prior to sub-phase deposition, the particle is deposited inside a hydrophilic wedge, a surfactant droplet is deposited on the tip of the hydrophilic wedge ($t_p = 0$), moves forward and, provided its volume V_D is sufficient, reaches the cargo particle and engulfs it. This short distance propulsion is based on the increase in hydrophilic surface area covered by the droplet as it moves forward in the hydrophilic wedge¹⁵⁴.

Experimental images of a typical pickup process are shown in Fig. 7.2 (b) with the initial cargo position indicated by the black arrows on the bottom. After the surfactant droplet detached from the dip-pen ($t_p = 0 \text{ s}$), it moved into the hydrophilic wedge, towards the cargo. When the droplet reached the cargo particle, it was initially drawn towards the droplet until it was completely engulfed ($t_p = 0.6 \text{ s}$), after which it moved with the droplet along the hydrophilic wedge.

Following the pickup of the cargo particle, sub-phase is deposited and the mobilization of the droplet on the liquid sublayer occurs in the same fashion as for droplets without cargo. Experimental images of the mobilization and propulsion of a particle transporting droplet are shown in Fig. 7.2(c,e-g), for an experiment in side-view config-

uration and taken with an up-right microscope, respectively. In Fig. 7.2(d) the position of a particle conveying droplet is shown as a function of time by the red squares. It is evident that the droplet dynamics are basically equivalent with the ones for a droplet propelling without a cargo particle (black circles). Cargo transport experiments were conducted with as-received, hydrophobic beads as well as UV/ozone treated (10 min) beads, hydrophilic, and no difference in the transport behavior was found.

7.3 Fluidic junction - splitting and routing

At binary junctions in the fluidic pathways, droplets can either be split or directed in one of the continuing branches. Experimental images of a splitting droplet ($V_D \approx 11$ nl) are shown in Fig. 7.3(a-c) ($h_0 = 250 \mu\text{m}$). When the droplet reached the junction ($t_j = 0$) it extended orthogonally to its original propulsion direction. After thinning in its center region the droplet split up and both daughter droplets propelled independently along their respective fluidic branches.

By increasing the temperature of one of the junction branches, the droplets can be directed into the opposite branch, without breakup occurring. Two different experimental implementations will be described here, demonstrating this thermal steering, both for droplets with and without cargo. The first implementation is depicted in Fig. 7.3(d). A small PDMS flow cell is attached to the bottom of the patterned glass substrate directly underneath one of the branches.

Figure 7.3(e-h) show experimental images of a droplet ($V_D \approx 24$ nl,) steered at a junction using this implementation ($h_0 = 285 \mu\text{m}$). Short before (≈ 2 s) the droplets reached the junction, water with a temperature of about 10°C above ambient temperature (25°C) was pumped through the flow cell at a flow rate of about 0.5 ml/s. Due to the thin substrate thickness ($150 \mu\text{m}$), the sub-phase film on top of the heated area quickly reaches the same temperature as the heating liquid. The droplet was initially stretched orthogonally to its propulsion direction, Fig. 7.3(f), retracted from the sub-phase liquid in the heated branch, Fig. 7.3(g), and propelled along the unheated branch, Fig. 7.3(h). It should be noted, that under standard conditions human body temperature would therefore be sufficient to provide the same temperature difference in the fluidic branches as this PDMS flow-cell setup.

In the second configuration, heating was performed using a focused infrared laser beam ($\lambda = 1470$ nm). The beam diameter at its focal point was $50 \mu\text{m}$ and the output power of the laser was measured to be 1 W. To ensure complete absorption of the laser beam, the patterned glass substrate was placed onto a *Schott KG-3* infrared-absorbing glass slide. The entire setup was placed onto an inverted microscope to monitor the droplets. This experimental implementation is sketched in Fig. 7.4 (a). When the droplets reached the junction, the laser was triggered for 1.5 s to illuminate a spot approximately 1 mm ahead of the droplets in one of the branches. As before, the droplets reliably

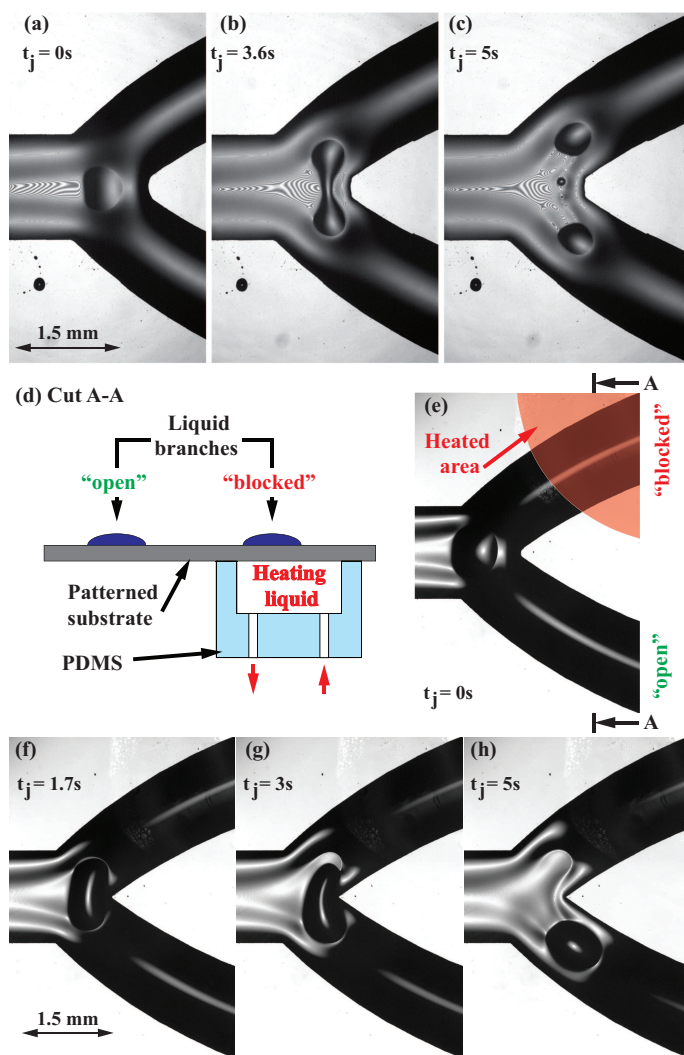


Figure 7.3: (a-c) Interference microscopy images of a droplet splitting at a fluidic junction. After reaching the junction, (a), the droplet was stretched orthogonally to the rivulet, thinned in its center, (b), and split into two independently propelling droplets, (c). (d) Experimental configuration for heat induced droplet steering at fluidic junctions using a PDMS flow cell. (e-h) Microscopy images of a droplet steered at a fluidic junction. (e) Short before the droplet reached the junction at $t_j = 0$, heating liquid was pumped through the flow cell. The droplet was stretched orthogonally to its propulsion direction, (f), detached from the sub-phase liquid in the heated branch, (g), and moved into the unheated branch, (h).

propelled along the unheated branch. Figure 7.4 (b-e) show microscopy images of a droplet steered at a fluidic junction using infrared illumination. The bright spot in the images on the lower branch is a guide laser, as marked in Fig. 7.4(c). It is illuminating an area around the focal point of the infrared laser. While this guide laser was switched on during the entire experiment, this was not the case for the infrared illumination. It should be noted that the droplet in the experiment shown in Fig. 7.4(b-e) was transporting a cargo bead (indicated in Fig. 7.4(e)).

The temperature asymmetry between the fluidic branches has two main effects. As shown in chapter 6, the viscosity of the sub-phase used in the experiments strongly decreases as temperature increases. Higher temperatures also lower the surface tension

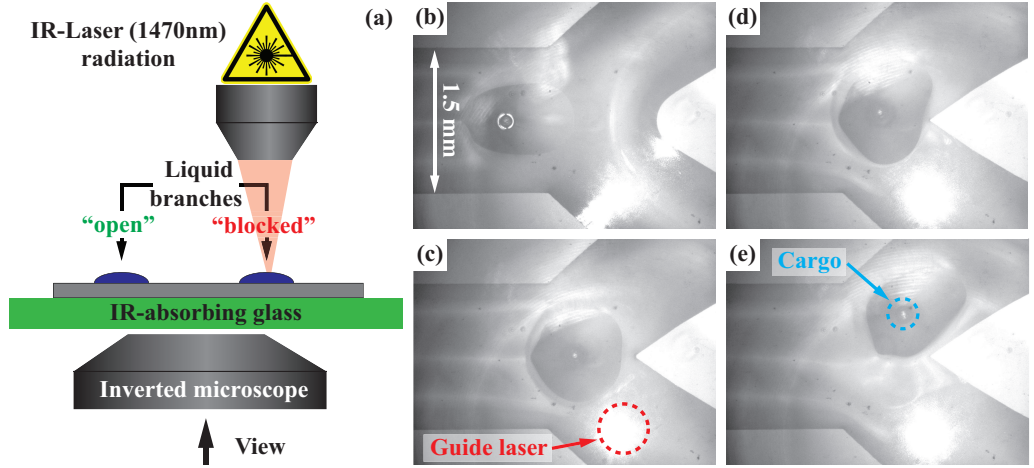


Figure 7.4: (a) Experimental configuration for heat induced droplet steering at fluidic junctions via infrared laser illumination. The glass substrate with a fluidic pathway including a junction is placed on an infrared absorbing glass. Inverted microscopy is used to monitor the drop dynamics. (b-e) Upon approach the droplet reaching the junction infrared laser illumination (nominal output power 1 W) of an area slightly ahead of the drop is triggered (illumination time ≈ 1 s). The localized temperature increase in the illuminated branch directs the droplet into the unheated branch. The bright spot in the lower branch of the microscope images is illumination by a guide laser, as marked in (c). The area illuminated by the infrared laser is in the center of this spot. The droplet in this experiment was transporting a cargo bead, as indicated in (e).

of most liquids, the temperature coefficient of glycerol is $\partial\gamma/\partial T \approx -0.06$ mN/(m K)¹¹⁷. The surface of the sub-phase (glycerol containing 0.55 wt% of SDS) directly ahead of the droplet is covered with with an unknown surface concentration Γ of the surfactant the droplet consists of. Considering the data shown in Fig. 6.2, the local surface tension of the sub-phase is therefore between $\gamma(\Gamma = 0) = 49.2$ mN/m and $\gamma(\Gamma = \Gamma_m) = \gamma(\Gamma = 0) - \Pi_{\text{droplet}} = 32.3$ mN/m, with Π_{droplet} denoting the spreading pressure of the droplet surfactant and Γ_m denoting the surface concentration corresponding to a dense mono-layer of this surfactant. To first order approximation the temperature coefficient of the sub-phase can be assumed to be same as for the pure glycerol, i.e. $\partial\gamma/\partial T \approx -0.06$ mN/(m K). In the case of steering via the PDMS flow cell shown in Fig. 7.3 the temperature of the steering fluid was $\Delta T = 10$ K above the experimental conditions. The flow-cell was attached on the bottom of a glass substrate with a thickness of ≈ 150 μm . Considering these experimental conditions, assuming a decay of the temperature increase from the heated area along the fluidic path over a distance of 0.5 mm is justified. The temperature gradient induces a surface tension gradient which then would be $\frac{\partial T}{\partial x} \frac{\partial \gamma}{\partial T} \approx -1.2 \frac{\text{mN/m}}{\text{mm}}$, assuming a linear temperature profile. When

considering the surfactant induced surface tension gradient, $\frac{\partial \Gamma}{\partial x} \frac{\partial \gamma}{\partial \Gamma}$ in an unmodulated branch a first order approximation is the assumption of a linear increase in surface tension from $\gamma(\Gamma = \Gamma_m) = \gamma(\Gamma = 0) - \Pi_{\text{droplet}} = 32.3 \text{ mN/m}$ to $\gamma(\Gamma = 0) = 49.2 \text{ mN/m}$. Here $\Gamma = 0$ corresponds to the condition of the sub-phase surface ahead of the leading edge of the droplet surfactant at x_{front} , which is spreading in a mono-layer ahead of the drop. For the surfactant induced surface tension gradient to be of the same order as the temperature induced gradient estimated before, the leading edge of the surfactant front x_{front} would therefore have to be $x_{\text{front}} - x_D \approx 14 \text{ mm}$. Steering experiments were conducted between approximately 30 s and several minutes after initial droplet mobilization. Considering the data shown in Fig. 3.6 for the spreading of a similar surfactant from a stationary source, these are realistic values. It can therefore be concluded that the mechanism underlying the thermal steering is a reduction of the interfacial and surface tension associated with a thermocapillary stress opposing the surfactant-induced Marangoni stress in the heated branch. The resulting inequality of the capillary and contact line forces on the droplet in the different branches facilitates the routing of the droplets.

7.4 Summary

It was demonstrated in this chapter that the self-propelling droplets described in chapter 6 can be applied as a transport mechanism for solid cargo particles. The trajectory of the droplets was prescribed by a chemically confined liquid substrate. A thermal routing mechanism was proposed for trajectory control of the droplets at fluidic junctions in the prescribed path. Two experimental implementations of this routing mechanism were demonstrated, a flow cell with temperature controlled liquid, as well as temperature modulation via infrared laser illumination. The independence from external power sources, integrated electrodes or heating elements to propel the droplets, makes the concept specifically interesting for applications in inexpensive, single-use-type devices.

Note: The results presented in this chapter have been published in *D. K. N. Sinz and A. A. Darhuber, Self-propelling surfactant droplets in chemically-confined microfluidics - cargo transport, drop-splitting and trajectory control, Lab on a Chip, 2012, Vol. 12 pp. 705-707* and in parts were also presented in the 2012 *Small Matters* Video contest by the American Institute of Physics (AIP). The entry was selected the contest winner by the Editorial Advisory Board of *Biomicrofluidics*.

Chapter 8

Summary and Perspectives

This thesis summarizes addresses experimental work regarding flow in thin liquid films induced by spatially non-uniform surfactant distributions. The flow dynamics as a consequence of the deposition of a droplet of an insoluble surfactant onto a thin liquid film covering a solid substrate where discussed as a starting point in Chapter 2. The conditions in the vicinity of the surfactant source, neglected in previous studies, were closely investigated. Application of interference and fluorescence microscopy revealed that the radially outwards directed displacement of the subphase, induced by the surfactant induced Marangoni stresses, is strongly influenced by the conditions near the surfactant source, i.e. the supply rate of surfactant from the source as the spreading proceeds. In this context a novel oscillatory contact line instability of the surfactant droplet was described. This instability modulates the flow rate of liquid from under the droplet and with it indirectly the supply of surfactant from the location of the source to the spreading front.

Considering conditions relevant to surfactant spreading in an oil reservoir in Chapter 3 the influence of a chemically imposed confinement on the sub-phase, along the surface of which a surfactant spreads, was investigated. A pronounced transition in the morphology evolution of the flowing thin film was found to be induced by the spatial restriction imposed through chemical surface patterns. The experimental results are in excellent agreement with numerical simulations by Myroslava Hanyak^{61,134}. With respect to conditions in an oil reservoir results the spreading of surfactants along liquid-air interfaces can only give a first order approximation. The studies of Chapter 3 were therefore extend to the interface between two thin liquid films in Chapter 4. Surfactant spreading was studied here along the liquid-liquid interface of thin liquid films. Resembling reservoir conditions, the films were subject to both, physical confinement as well as confinement imposed by a wettability pattern.

In the context of surfactant spreading, it is a conceptually entirely new discovery, that surfactant induced Marangoni flows cannot only transport surfactants along fluid interfaces but can also efficiently transport surfactants along interfaces exhibiting con-

siderably sized discontinuities. All existing literature in the field of surfactant spreading exclusively regarded continuous fluid interfaces. This novel phenomenon was the topic of Chapter 5. The convective surfactant spreading along discontinuous interfaces is directly relevant to the spreading of surfactants in an oil reservoir. In these porous underground rock formations the oil-water interface is not necessarily connected, such that surfactant spreading through a reservoir involves transport over interface discontinuities.

In future studies it would be of interest to investigate the possibility of utilizing the described surfactant induced flow phenomena as a transport mechanism of functional substances¹⁵⁰, e.g. wettability modifiers. This would be specifically interesting for dead-end pore geometries as they are inaccessible to pressure driven flows. Suitable alteration of the wettability conditions in such pores might induce oil expulsion, e.g. via gravity driven mobilization of previously trapped oil volumes.

The implications of surfactant induced flow phenomena in printing and coating applications is another field suggesting itself for fruitful future research. Surfactants causing crater formation and dry spot nucleation in coating layers can induce mottling and therefore, in the case of protective coatings as found in automotive applications, be a precursor of wear and corrosion¹⁴⁸. The presence of surfactants in the ink used for inkjet printing was recently shown to retard the leveling process of printed lines⁶⁰. Since solidification prior to leveling should be avoided to ensure high quality prints this phenomenon extends the drying time of the inks. Combining qualitatively different surfactants, e.g. slow and fast adsorbing types, might reduce the flow retarding surface tension gradients induced by the surface deformation during leveling. Such a surfactant combination would therefore have a positive effect on the leveling times.

Lubrication of rolling bearings is another technological application in which thin film fluid flow plays a significant role. The lubrication of the bearings is often the determining factor for their lifetime^{25,145}, provided correct operating conditions. A rolling bearing is properly lubricated if the rolling element is separated from the raceway surface via low shear separation layer formed by the lubricant (oil or grease). Fluorinated surfactants could possibly modulate the surface tension of lubricant fluids sufficiently to induce flows under suitable conditions. Already minute contributions towards the reformation of lubrication layers could significantly extend the service life of closed roller bearings where lubrication cannot be ensured via regular maintenance. In this context it could also be of interest to investigate the possibility of fluid management via surface energy modification.

A focus of this thesis besides the spreading of surfactants was on the self-propulsion of surfactant droplets. Experimental results of these studies were presented in Chapter 6 and 7. Self-propulsion dynamics exhibited by insoluble surfactant droplets on thin liquid films are systematically investigated in Chapter 6. Several modes of motion were described. A directed continuous propulsion as well as a meandering mode of propulsion. This meandering motion can also be exhibited by a pair of droplets in a synchronized fashion. Finally an intermittent form of droplet propagation was described.

The systematic study of the various modes of propulsion is complemented with the

outline of a potential application in microfluidic devices in Chapter 7. In this context the novel phenomenon of transporting solid cargo particles using these self-propelling droplets is described. Navigation of the droplets across micro-fluidic networks is demonstrated by controlling the temperature field around the drop e.g. using an infrared laser. The independence from external power sources, integrated electrodes or heating elements to propel the droplets, makes the concept specifically interesting for applications in inexpensive, single-use-type devices.

Bibliography

- [1] M. Abdelgawad, S. L. S. Freire, H. Yang, and A. R. Wheeler. All-terrain droplet actuation. *Lab on a Chip*, 8:672–677, 2008.
- [2] M. Abdelgawad, M. W. L. Watson, and A. R. Wheeler. Hybrid microfluidics: A digital-to-channel interface for in-line sample processing and chemical separations. *Lab on a Chip*, 9:1046–1051, 2009.
- [3] J. Adler and L. Sowerby. Shallow three-dimensional flows with variable surface tension. *Journal of Fluid Mechanics*, 42:549–559, 1970.
- [4] A. B. Afsar Siddiqui, P. F. Luckham, and O. K. Matar. The spreading of surfactant solutions on thin liquid films. *Advances in Colloid and Interface Science*, 106:183–236, 2003.
- [5] A. B. Afsar Siddiqui, P. F. Luckham, and O. K. Matar. Unstable spreading of aqueous anionic surfactant solutions on liquid films. part 1. sparingly soluble surfactant. *Langmuir*, 19:696–702, 2003.
- [6] A. B. Afsar Siddiqui, P. F. Luckham, and O. K. Matar. Unstable spreading of aqueous anionic surfactant solutions on liquid films. part 2. highly soluble surfactant. *Langmuir*, 19:703–708, 2003.
- [7] J. Ahmad and R. S. Hansen. A simple quantitative treatment of the spreading of monolayers on thin liquid films. *Journal of Colloid and Interface Science*, 38:601–604, 1972.
- [8] C. Bain, G. Burnett Hall, and R. Montgomerie. Rapid motion of liquid drops. *Nature*, 372:414–415, 1994.
- [9] S. Berg. Marangoni-driven spreading along liquid-liquid interfaces. *Physics of Fluids*, 21:032105, 2009.
- [10] E. Berthier and D J. Beebe. Flow rate analysis of a surface tension driven passive micropump. *Lab on a Chip*, 7:1475–1478, 2007.

-
- [11] M. S. Borgas and J. B. Grotberg. Monolayer flow on a thin film. *Journal of Fluid Mechanics*, 193:151–170, 1988.
- [12] A. Borhan, H. Haj Hariri, and A. Nadim. Effect of surfactants on the thermocapillary migration of a concentric compound drop. *Journal of Colloid and Interface Science*, 149:553–560, 1992.
- [13] F. Brochard. Motions of droplets on solid surfaces induced by chemical or thermal gradients. *Langmuir*, 5:432–438, 1989.
- [14] J. B. Brzoska, N. Shahidzadeh, and F. Rondelez. Evidence of a transition temperature for the optimum deposition of grafted monolayer coatings. *Nature*, 360:719–721, 1992.
- [15] J. Bull and J. B. Grotberg. Surfactant spreading on thin viscous films: film thickness evolution and periodic wall stretch. *Experiments in Fluids*, 34:1–15, 2003.
- [16] M. Cachile and A. M. Cazabat. Spontaneous spreading of surfactant solutions on hydrophilic surfaces in ethylene and diethylene glycol. *Langmuir*, 15:1515–1521, 1999.
- [17] M. Cachile, M. Schneemilch, A. Hamraoui, and A. M. Cazabat. Films driven by surface tension gradients. *Advances in Colloid and Interface Science*, 96:59–74, 2002.
- [18] D. W. Camp and J. C. Berg. The spreading of oil on water in the surface-tension regime. *Journal of Fluid Mechanics*, 184:445–462, 1987.
- [19] S. T. Chang, V. N. Paunov, D. N. Petsev, and O. D. Velev. Remotely powered self-propelling particles and micropumps based on miniature diodes. *Nature materials*, 6:235–240, 2007.
- [20] S. Chao and D. R. Meldrum. Spontaneous, oscillatory liquid transport in surface tension-confined microfluidics. *Lab on a Chip*, 9:867–869, 2009.
- [21] M. Chaudhury and G. Whitesides. How to make water run uphill. *Science*, 256:1539–1541, 1992.
- [22] J. Chen and K. J. Stebe. Surfactant-induced retardation of the thermocapillary migration of a droplet. *Journal of Fluid Mechanics*, 340:35–59, 1997.
- [23] Y.-J. Chen, Y. Nagamine, and K. Yoshikawa. Self-propelled motion of a droplet induced by marangoni-driven spreading. *Physical Review E*, 80:16303, 2009.
- [24] R. V. Craster and O. K. Matar. On autophobing in surfactant-driven thin films. *Langmuir*, 23:2588–2601, 2007.

- [25] B. Damiens, C.H. Venner, P.M.E. Cann, and A.A. Lubrecht. Starved lubrication of elliptical ehd contacts. *Journal of Tribology*, 126:105–111, 2004.
- [26] S. Daniel and M. K. Chaudhury. Rectified motion of liquid drops on gradient surfaces induced by vibration. *Langmuir*, 18:3404–3407, 2002.
- [27] S. Daniel, M. K. Chaudhury, and P.-G. de Gennes. Vibration-actuated drop motion on surfaces for batch microfluidic processes. *Langmuir*, 21:4240–4248, 2005.
- [28] A. A. Darhuber, J. Z. Chen, J. M. Davis, and S. M. Troian. A study of mixing in thermocapillary flows on micropatterned surfaces. *Philosophical Transactions of the Royal Society of London. Series A: Mathematical, Physical and Engineering Sciences*, 362(1818):1037–1058, 2004.
- [29] A. A. Darhuber and S. M. Troian. Marangoni driven structures in thin film flows. *Physics of Fluids*, 15:S9, 2003.
- [30] A. A. Darhuber, J. P. Valentino, J. M. Davis, S. M. Troian, and S. Wagner. Microfluidic actuation by modulation of surface stresses. *Applied Physics Letters*, 82:657–659, 2003.
- [31] A. A. Darhuber, J. P. Valentino, and S. M. Troian. Planar digital nanoliter dispensing system based on thermocapillary actuation. *Lab on a Chip*, 10:1061–1071, 2010.
- [32] A.A. Darhuber, J.P. Valentino, S.M. Troian, and S. Wagner. Thermocapillary actuation of droplets on chemically patterned surfaces by programmable microheater arrays. *Journal of Microelectromechanical Systems*, 12:873–879, 2003.
- [33] S. H. Davis, A.-K. Liu, and G. R. Sealy. Motion driven by surface-tension gradients in a tube lining. *Journal of Fluid Mechanics*, 62:737–751, 1974.
- [34] A. H. Demond and A. S. Lindner. Estimation of interfacial tension between organic liquids and water. *Environmental Science & Technology*, 27(12):2318–2331, 1993.
- [35] A. D. Dussaud, O. K. Matar, and S. M. Troian. Spreading characteristics of an insoluble surfactant film on a thin liquid layer: comparison between theory and experiment. *Journal of Fluid Mechanics*, 544:23–51, 2005.
- [36] A. D. Dussaud and S. M. Troian. Dynamics of spontaneous spreading with evaporation on a deep fluid layer. *Physics of Fluids*, 10:23–38, 1998.
- [37] A. D. Dussaud, S. M. Troian, and S. R. Harris. Fluorescence visualization of a convective instability which modulates the spreading of volatile surface films. *Physics of Fluids*, 10:1588–1596, 1998.

- [38] B. D. Edmonstone, R. V. Craster, and O. K. Matar. Surfactant-induced fingering phenomena beyond the critical micelle concentration. *Journal of Fluid Mechanics*, 564:105–138, 2006.
- [39] B.D. Edmonstone and O.K. Matar. Simultaneous thermal and surfactant-induced marangoni effects in thin liquid films. *Journal of Colloid and Interface Science*, 274:183–199, 2004.
- [40] F. F. Espinosa, A. H. Shapiro, J. J. Fredberg, and R. D. Kamm. Spreading of exogenous surfactant in an airway. *Journal of Applied Physiology*, 75:2028–2039, 1993.
- [41] P.L. Evans, L.W. Schwartz, and R.V. Roy. A mathematical model for crater defect formation in a drying paint layer. *Journal of Colloid and Interface Science*, 227:191–205, 2000.
- [42] D. W. Fallest, A. M. Lichtenberger, C. J. Fox, and K. E. Daniels. Fluorescent visualization of a spreading surfactant. *New Journal of Physics*, 12:073029, 2010.
- [43] J. A. Fay. *In Oil on the Sea*. Plenum: N.Y., 1969.
- [44] B. J. Fischer, A. A. Darhuber, and S. M. Troian. Streamlets and branching dynamics in surfactant driven flow. *Physics of Fluids*, 13:S11, 2001.
- [45] B. J. Fischer and S. M. Troian. Growth and decay of localized disturbances on a surfactant-coated spreading film. *Physical Review E*, 67:016309, Jan 2003.
- [46] B. J. Fischer and S. M. Troian. Thinning and disturbance growth in liquid films mobilized by continuous surfactant delivery. *Physics of Fluids*, 15:3837–3845, 2003.
- [47] M. Foda and R. G. Cox. The spreading of thin liquid films on a water-air interface. *Journal of Fluid Mechanics*, 101:33–51, 1980.
- [48] D. Follows, F. Tiberg, R.K. Thomas, and M. Larsson. Multilayers at the surface of solutions of exogenous lung surfactant: Direct observation by neutron reflection. *Biochimica et Biophysica Acta*, 1768:228–235, 2007.
- [49] B. Frank and S. Garoff. Origins of the complex motion of advancing surfactant solutions. *Langmuir*, 11:87–93, 1995.
- [50] M. Fricke and K. Sundmacher. Mass transfer model of triethylamine across the n-decane/water interface derived from dynamic interfacial tension experiments. *Langmuir*, 28:6803–6815, 2012.
- [51] D. P. Gaver and J.B. Grotberg. The dynamics of a localized surfactant on a thin film. *Journal of Fluid Mechanics*, 213:127–148, 1990.

- [52] D. P. Gaver and J.B. Grotberg. Droplet spreading on a thin viscous film. *Journal of Fluid Mechanics*, 235:399, 1992.
- [53] A. Georgiadis, G. Maitland, J. P. M. Trusler, and A. Bismarck. Interfacial tension measurements of the (h₂o + n-decane + co₂) ternary system at elevated pressures and temperatures. *Journal of Chemical & Engineering Data*, 56:4900–4908, 2011.
- [54] A. Goebel and K. Lunkenheimer. Interfacial tension of the water/n-alkane interface. *Langmuir*, 13:369–372, 1997.
- [55] H. P. Greenspan. On the motion of a small viscous droplet that wets a surface. *Journal of Fluid Mechanics*, 84:125–143, 1978.
- [56] J. B. Grotberg. Pulmonary flow and transport phenomena. *Annual Review of Fluid Mechanics*, 26:529–571, 1994.
- [57] D. Halpern and J. B. Grotberg. Dynamics and transport of a localized soluble surfactant on a thin film. *Journal of Fluid Mechanics*, 237:1–11, 1992.
- [58] A. Hamraoui, M. Cachile, C. Poulard, and A.M. Cazabat. Fingering phenomena during spreading of surfactant solutions. *Colloids and Surfaces A: Physicochemical and Engineering Aspects*, 250:215–221, 2004.
- [59] R. Hanumanthu and K. J. Stebe. Transient enhancement of thermocapillary flow in a two-dimensional cavity by a surfactant. *Physics of Fluids*, 19:042103, 2007.
- [60] M. Hanyak, A. A. Darhuber, and M. Ren. Surfactant-induced delay of leveling of inkjet-printed patterns. *Journal of Applied Physics*, 109:074905, 2011.
- [61] M. Hanyak, D. K. N. Sinz, and A. A. Darhuber. Soluble surfactant spreading on spatially confined thin liquid films. *Soft Matter*, 8:3660–3671, 2012.
- [62] Y. Hayashima, M. Nagayama, Y. Doi, S. Nakata, M. Kimurac, and M. Iida. Self-motion of a camphoric acid boat sensitive to the chemical environment. *Physical Chemistry Chemical Physics*, 4:1386–1392, 2002.
- [63] Y. Hayashima, M. Nagayama, and S. Nakata. A camphor grain oscillates while breaking symmetry. *Journal of Physical Chemistry B*, 105:5353–5357, 2001.
- [64] S. He and J. B. Ketterson. Surfactant-driven spreading of a liquid on a vertical surface. *Physics of Fluids*, 7:2640–2647, 1995.
- [65] E. Heisler, N. J. Suematsu, A. Awazu, and H. Nishimori. Swarming of self-propelled camphor boats. *Physical Review E*, 85:055201, 2012.

- [66] D P Hoult. Oil spreading on the sea. *Annual Review of Fluid Mechanics*, 4:341–368, 1972.
- [67] C. Huh, M. Inoue, and S. G. Mason. Uni-directional spreading of one liquid on the surface of another. *The Canadian Journal of Chemical Engineering*, 53:367–371, 1975.
- [68] M. Ibele, T. E. Mallouk, and A. Sen. Schooling behavior of light-powered autonomous micromotors in water. *Angewandte Chemie*, 121:3358–3362, 2009.
- [69] K. Ichimura, S. Oh, and M. Nakagawa. Light-driven motion of liquids on a photoresponsive surface. *Science*, 288:1624–1626, 2000.
- [70] R. F. Ismagilov, A. Schwartz, N. Bowden, and G. M. Whitesides. Autonomous movement and self-assembly. *Angewandte Chemie*, 114:674–676, 2002.
- [71] O. E. Jensen. Self-similar, surfactant-driven flows. *Physics of Fluids*, 6:1084–1094, 1994.
- [72] O. E. Jensen. The spreading of insoluble surfactant at the free surface of a deep fluid layer. *Journal of Fluid Mechanics*, 293:349–378, 1995.
- [73] O. E. Jensen and J. B. Grotberg. Insoluble surfactant spreading on a thin viscous film: shock evolution and film rupture. *Journal of Fluid Mechanics*, 240:259–288, 1992.
- [74] O. E. Jensen and J. B. Grotberg. The spreading of heat or soluble surfactant along a thin liquid film. *Physics of Fluids A: Fluid Dynamics*, 5:58–68, 1993.
- [75] O. E. Jensen and S. Naire. The spreading and stability of a surfactant-laden drop on a prewetted substrate. *Journal of Fluid Mechanics*, 554:5–24, 2006.
- [76] K. John, M. Bär, and U. Thiele. Self-propelled running droplets on solid substrates driven by chemical reactions. *The European Physical Journal E*, 18:183–199, 2005.
- [77] T. B. Jones, M. Gunji, M. Washizu, and M. J. Feldman. Dielectrophoretic liquid actuation and nanodroplet formation. *Journal of Applied Physics*, 89:1441–1448, 2001.
- [78] P Joos and J V. Hunsel. Spreading of aqueous surfactant solutions on organic liquids. *Journal of Colloid and Interface Science*, 106:161–167, 1985.
- [79] T. Kajiya, D Kaneko, and M Doi. Dynamical visualization of coffee stain phenomenon in droplets of polymer solution via fluorescent microscopy. *Langmuir*, 24:12369–12374, 2008.

- [80] H. Kitahata, S. Hiromatsu, Y. Doi, S. Nakata, and Mo. R. Islam. Self-motion of a camphor disk coupled with convection. *Physical Chemistry Chemical Physics*, 6:2409–2414, 2004.
- [81] T. R. Kline, W. F. Paxton, T. E. Mallouk, and A. Sen. Catalytic nanomotors: Remote-controlled autonomous movement of striped metallic nanorods. *Angewandte Chemie*, 117:754–756, 2005.
- [82] I. Lagzi, S. Soh, P. J. Wesson, Kevin P. Browne, and Bartosz A. Grzybowski. Maze solving by chemotactic droplets. *Journal of the American Chemical Society*, 132:1198–1199, 2010.
- [83] L. W. Lake. *Enhanced oil recovery*. Prentice-Hall, 1989.
- [84] P. Lazar and H. Riegler. Reversible self-propelled droplet movement: A new driving mechanism. *Physical Review Letters*, 95:136103, 2005.
- [85] J. Lee and C. Kim. Surface-tension-driven microactuation based on continuous electrowetting. *Journal of Microelectromechanical Systems*, 9:171–180, 2000.
- [86] S. W. Lee, D. Y. Kwok, and P. E. Laibinis. Chemical influences on adsorption-mediated self-propelled drop movement. *Physical Review E*, 65:051602, 2002.
- [87] V. G. Levich. *Physicochemical Hydrodynamics*. Prentice-Hall, 1962.
- [88] N. S. Lynn and D. S. Dandy. Passive microfluidic pumping using coupled capillary/evaporation effects. *Lab on a Chip*, 9:3422–3429, 2009.
- [89] N. Magome and K. Yoshikawa. Nonlinear oscillation and ameba-like motion in an oil/water system. *Journal of Physical Chemistry*, 100:19102–19105, 1996.
- [90] K. Masahiro, Y. Hayashima, M. Nagayama, and S. Nakata. Synchronized self-motion of two camphor boats. *Langmuir*, 17:7124–7129, 2001.
- [91] O. K. Matar and R. V. Craster. Dynamics of surfactant-assisted spreading. *Soft Matter*, 5:3801–3809, 2009.
- [92] O. K. Matar and S. M. Troian. Growth of non-modal transient structures during the spreading of surfactant coated films. *Physics of Fluids*, 10:1234–1236, 1998.
- [93] O. K. Matar and S. M. Troian. The development of transient fingering patterns during the spreading of surfactant coated films. *Physics of Fluids*, 11:3232–3246, 1999.
- [94] N. Morrow and J. Buckley. Improved oil recovery by low-salinity waterflooding. *Journal of Petroleum Technology*, 63, 2011.

- [95] F. Mugele and J. Baret. Electrowetting: from basics to applications. *Journal of Physics: Condensed Matter*, 17:R705–R774, 2005.
- [96] M. Nagayama, S. Nakata, Y. Doi, and Y. Hayashima. A theoretical and experimental study on the unidirectional motion of a camphor disk. *Physica D*, 194:151–165, 2004.
- [97] M. Nagayama, M. Yadome, M. Murakami, N. Kato, J. Kirisakae, and S. Nakata. Bifurcation of self-motion depending on the reaction order. *Physical Chemistry Chemical Physics*, 11:1085–1090, 2009.
- [98] S. Nakata, Y. Doi, and Y. Hayashima. Intermittent motion of a camphene disk at the center of a cell. *Journal of Physical Chemistry B*, 106:11681–11684, 2002.
- [99] S. Nakata, Y. Doi, and H. Kitahata. Synchronized motion of a mobile boundary driven by a camphor fragment. *Journal of Colloid and Interface Science*, 279:503–508, 2004.
- [100] S. Nakata, Y. Doi, and H. Kitahata. Synchronized sailing of two camphor boats in polygonal chambers. *Journal of Physical Chemistry B*, 109:1798–1802, 2005.
- [101] S. Nakata and Y. Hayashima. Spontaneous dancing of a camphor scraping. *Journal of the Chemical Society, Faraday Transactions*, 94:3655–3658, 1998.
- [102] S. Nakata and Y. Hayashima. Spontaneous motion of a solid is sensitive to the ph of an aqueous phase. *Langmuir*, 15:1872–1875, 1999.
- [103] S. Nakata, Y. Hayashima, and T. Ishii. Self-motion of a camphoric acid boat as a function of ph of aqueous solutions. *Colloids and Surfaces A: Physicochemical and Engineering Aspects*, 182:231–238, 2001.
- [104] S. Nakata, Y. Hayashima, and H. Komoto. Spontaneous switching of camphor motion between two chambers. *Physical Chemistry Chemical Physics*, 2:2395–2399, 2000.
- [105] S. Nakata and S. Hiromatsu. Intermittent motion of a camphor float. *Colloids and Surfaces A: Physicochemical and Engineering Aspects*, 224:157–163, 2003.
- [106] S. Nakata, S. Hiromatsu, and H. Kitahata. Multiple autonomous motions synchronized with complex formation. *Journal of Physical Chemistry B*, 107:10557–10559, 2003.
- [107] S. Nakata, Y. Iguchi, S. Ose, M. Kuboyama, T. Ishii, and K. Yoshikawa. Self-rotation of a camphor scraping on water: New insight into the old problem. *Langmuir*, 13:4454–4458, 1997.

- [108] S. Nakata, Y. Iguchi, S. Ose, and Toshio Ishii. pH-sensitive self-motion of a solid scraping on an aqueous phase. *Journal of Physical Chemistry B*, 102:7425–7427, 1998.
- [109] S. Nakata, N. Kawagishib, M. Murakamia, N. J. Suematsua, and M. Nakamura. Intermittent motion of a camphor float depending on the nature of the float surface on water. *Colloids and Surfaces A: Physicochemical and Engineering Aspects*, 349:74–77, 2009.
- [110] S. Nakata and J. Kirisaka. Characteristic motion of a camphanic acid disk on water depending on the concentration of triton x-100. *Journal of Physical Chemistry B*, 110:1856–1859, 2006.
- [111] S. Nakata and J. Kirisaka. Characteristic motion of a camphanic acid disk on water depending on the concentration of triton x-100. *Journal of Physical Chemistry B*, 110:1856–1859, 2006.
- [112] S. Nakata, J. Kirisaka, Y. Arima, and T. Ishii. Self-motion of a camphanic acid disk on water with different types of surfactants. *Journal of Physical Chemistry B*, 110:21131–21134, 2006.
- [113] S. Nakata, M. I. Kohira, and Y. Hayashima. Mode selection of a camphor boat in a dual-circle canal. *Chemical Physics Letters*, 322:419–423, 2000.
- [114] S. Nakata, H. Komoto, K. Hayashi, and Michael Menzinger. Mercury drop “attacks” an oxidant crystal. *Journal of Physical Chemistry B*, 104:3589–3593, 2000.
- [115] S. Nakata and K. Matsuo. Characteristic self-motion of a camphor boat sensitive to ester vapor. *Langmuir*, 21:982–984, 2005.
- [116] S. Nakata and M. Murakami. Self-motion of a camphor disk on an aqueous phase depending on the alkyl chain length of sulfate surfactants. *Langmuir*, 26:2414–2417, 2010.
- [117] A. A. Newman. *Glycerol*. CRC Press, 1968.
- [118] A. Oron, S. H. Davis, and S. G. Bankoff. Long-scale evolution of thin liquid films. *Reviews of Modern Physics*, 69:931–980, 1997.
- [119] W. F. Paxton, K. C. Kistler, C. C. Olmeda, A. Sen, S. K. St. Angelo, Y. Cao, T. E. Mallouk, P. E. Lammert, and V. H. Crespi. Catalytic nanomotors: Autonomous movement of striped nanorods. *Journal of the American Chemical Society*, 126:13424–13431, 2004.
- [120] R. J. Petrie, T. Bailey, C. B. Gorman, and J. Genzer. Fast directed motion of “fakir” droplets. *Langmuir*, 20:9893–9896, 2004.

- [121] M. G. Pollack, A. D. Shenderov, and R. B. Fair. Electrowetting-based actuation of droplets for integrated microfluidics. *Lab on a Chip*, 2:96–101, 2002.
- [122] V. Pratap, N. Moumen, and R. S. Subramanian. Thermocapillary motion of a liquid drop on a horizontal solid surface. *Langmuir*, 24:5185–5193, 2008.
- [123] L. Rayleigh. On the tension of recently formed liquid surfaces. *Proceedings of the Royal Society of London*, 47:281–287, 1890.
- [124] P. J. Resto, B. J. Mogen, E. Berthier, and J. C. Williams. An automated microdroplet passive pumping platform for high-speed and packeted microfluidic flow applications. *Lab on a Chip*, 10:23–26, 2010.
- [125] J. Sagiv. Organized monolayers by adsorption. 1. formation and structure of oleophobic mixed monolayers on solid surfaces. *Journal of the American Chemical Society*, 102:92–98, 1980.
- [126] D. Santos, F. Domingues, and T. Ondarçuhu. Free-running droplets. *Physical Review Letters*, 75:2972–2975, 1995.
- [127] L. L. Schramm. *Surfactants: fundamentals and applications in the petroleum industry*. Cambridge University Press:Cambridge, 2000.
- [128] O. Schulz and M. Markus. Velocity distributions of camphor particle ensembles. *Journal of Physical Chemistry B*, 111:8175–8178, 2007.
- [129] L. W. Schwartz and R. R. Eley. Simulation of droplet motion on low-energy and heterogeneous surfaces. *Journal of Colloid and Interface Science*, 202:173–188, 1998.
- [130] J. B. Segur and H. E. Oberstar. *Industrial and Engineering Chemistry*, 43:2117–2120, 1951.
- [131] D. O. Shan and R. S. Schechter. *Improved oil recovery by surfactant and polymer flooding*. Academic Press Inc.: New York, 1977.
- [132] D. K. N. Sinz and A. A. Darhuber. Self-propelling surfactant droplets in chemically-confined microfluidics - cargo transport, drop-splitting and trajectory control. *Lab on a Chip*, 12:705–707, 2012.
- [133] D. K. N. Sinz, M. Hanyak, and A. A. Darhuber. Immiscible surfactant droplets on thin liquid films: Spreading dynamics, subphase expulsion and oscillatory instabilities. *Journal of Colloid and Interface Science*, 364:519–529, 2011.
- [134] D. K. N. Sinz, M. Hanyak, J. C. H. Zeegers, and A. A. Darhuber. Insoluble surfactant spreading along thin liquid films confined by chemical surface patterns. *Physical Chemistry Chemical Physics*, 13:9768–9777, 2011.

- [135] S. Soh, K. J. M. Bishop, and B. A. Grzybowski. Dynamic self-assembly in ensembles of camphor boats. *Journal of Physical Chemistry B*, 2008:10848–10853, 2008.
- [136] V. M. Starov, A. Ryck, and M. G. Velarde. On the spreading of an insoluble surfactant over a thin viscous liquid layer. *Journal of Colloid and Interface Science*, 190:104–113, 1997.
- [137] R. Stocker and J. W. M. Bush. Spontaneous oscillations of a sessile lens. *Journal of Fluid Mechanics*, 583:465–475, 2007.
- [138] N. J. Suemats, Y. Ikura, M. Nagayama, H. Kitahata, N. Kawagishi, M. Murakami, and S. Nakata. Mode-switching of the self-motion of a camphor boat depending on the diffusion distance of camphor molecules. *Journal of Physical Chemistry C*, 114:9876–9882, 2010.
- [139] Y. Sumino, N. Magome, T. Hamada, and K. Yoshikawa. Self-running droplet: Emergence of regular motion from nonequilibrium noise. *Physical Review Letters*, 94:068301, 2005.
- [140] T. F. Svitova, R. I. M. Hill, and C. J. Radke. Spreading of aqueous dimethyldodecylammonium bromide surfactant droplets over liquid hydrocarbon substrates. *Langmuir*, 15:7392–7402, 1999.
- [141] E. Tan and S. T. Thoroddsen. Marangoni instability of two liquids mixing at a free surface. *Physics of Fluids*, 10:3038–3040, 1998.
- [142] S. M. Troian, E. Herbolzheimer, and S. A. Safran. Model for the fingering instability of spreading surfactant drops. *Physical Review Letters*, 65:333–336, 1990.
- [143] S. M. Troian, X. L. Wu, and S. A. Safran. Fingering instability in thin wetting films. *Physical Review Letters*, 62:1496–1499, 1989.
- [144] W. Tsai and L.-Y. Liu. Transport of exogenous surfactants on a thin viscous film within an axisymmetric airway. *Colloids and Surfaces A: Physicochemical and Engineering Aspects*, 234:51–62, 2004.
- [145] C.H. Venner, M.T. van Zoelen, and P.M. Lugt. Thin layer flow and film decay modeling for grease lubricated rolling bearings. *Tribology International*, 47:175–187, 2012.
- [146] M. von Bahr, F. Tiberg, and B. V. Zhmud. Spreading dynamics of surfactant solutions. *Langmuir*, 15:7069–7075, 1999.
- [147] G. M. Walker and D. J. Beebe. A passive pumping method for microfluidic devices. *Lab on a Chip*, 2:131–134, 2002.

-
- [148] M. R. E. Warner, R. V. Craster, and O. K. Matar. Dewetting of ultrathin surfactant-covered films. *Physics of Fluids*, 14:4040–4054, 2002.
- [149] M. R. E. Warner, R. V. Craster, and O. K. Matar. Fingering phenomena associated with insoluble surfactant spreading on thin liquid films. *Journal of Fluid Mechanics*, 510:169–200, 2004.
- [150] D. T. Wasan and A. D. Nikolov. Spreading of nanofluids on solids. *Nature*, 423:156–159, 2003.
- [151] H. A. R. Williams and O. E. Jensen. Surfactant transport over airway liquid lining of nonuniform depth. *Journal of Biomechanical Engineering*, 122:159–166, 2000.
- [152] C.-S. Yih. Fluid motion induced by surface-tension variation. *Physics of Fluids*, 11:477–480, 1968.
- [153] S. Zeppieri, J. Rodríguez, and A. L. López de Ramos. Interfacial tension of alkane + water systems. *Journal of Chemical & Engineering Data*, 46:1086–1088, 2001.
- [154] J. Zhang and Y. Han. Shape-gradient composite surfaces: Water droplets move uphill. *Langmuir*, 23:6136–6141, 2007.

List of symbols

t	time.
x, y, z	spatial coordinates in a Cartesian coordinate system.
r, ϕ, z	spatial coordinates in a Cylindrical coordinate system.
μ	viscosity.
p	pressure.
p_{cap}	capillary pressure.
m	mass.
γ	surface or interfacial tension.
Γ	surface concentration of a surface active substance.
γ_m	surface tension of a liquid covered by a dense monolayer of surfactant.
Γ_m	surface concentration of a surface active substance on a liquid covered by a dense monolayer of this surfactant.
c	surfactant bulk concentration.

Π	spreading pressure of a surfactant, the difference in surface tensions between a liquid surface covered with a certain surface concentration of a surfactant and without this surfactant.
λ	wavelength of light, e.g. illuminating light.
$n_{Substance}$	refractive index of a substance.
I	fluorescence intensity.
Δt	duration of the global subphase expulsion stage, as discussed in chapter 2.
r_{max}	rim position in radial spreading experiments.
h_0	initial sub-phase film thicknesses.
R_0	droplet diameter.
V_0	volume of sub-phase initially located under the deposited surfactant droplet, as discussed in chapter 2.
V_{gl}	volume of sub-phase expelled in the global expulsion stage, as discussed in chapter 2.
w	width of chemical surface patterns.
L	length of chemical surface patterns.
ω	spinning speed during spin coating.
ϵ	aspect ratio, film thickness divided by pattern width or subphase film thickness divided by droplet width.
w_{Gap}	distance between consecutive pillars in the experiments of chapter 5.
D_P	pillar diameter in the experiments as discussed in chapter 5.

h_P	pillar height in the experiments as discussed in chapter 5.
x_D, y_D	x - and y -position of self-propelling droplets, chapter 6.
v_x, v_y	velocity components of self-propelling droplets in x - and y -direction, respectively, chapter 6.
V_D	droplet volume, chapter 6.

List of publications

The work described in this thesis is in parts presented in the following journal publications:

- David K. N. Sinz, Myroslava Hanyak, Jos C. H. Zeegers and Anton A. Darhuber, *Insoluble surfactant spreading along thin liquid films confined by chemical surface patterns*, Physical Chemistry Chemical Physics, 2011, **13**, 9768-9777.
- David K. N. Sinz, Myroslava Hanyak and Anton A. Darhuber *Immiscible surfactant droplets on thin liquid films: Spreading dynamics, subphase expulsion and oscillatory instabilities* Journal of Colloid and Interface Science, 2011, **364**, 519-529.
- David K. N. Sinz and Anton A. Darhuber, *Self-propelling surfactant droplets in chemically-confined microfluidics - cargo transport, drop-splitting and trajectory control*, Lab on a Chip, 2012, **12**, 705-707.
- Myroslava Hanyak, David K. N. Sinz and Anton A. Darhuber, *Soluble surfactant spreading on spatially confined thin liquid films*, Soft Matter, 2012, **8**, 7660-7671.

Manuscripts in preparation:

- David K. N. Sinz, Myroslava Hanyak and Anton A. Darhuber, *Surfactant spreading over discontinuous interfaces*.
- David K. N. Sinz and Anton A. Darhuber, *On the self-sustained motion of droplets*.
- Myroslava Hanyak, David K. N. Sinz and Anton A. Darhuber, *spreading of surfactants along liquid-liquid interfaces of thin films*.

Summary

The topic of the experimental work summarized in my thesis is the flow in thin liquid films induced by non-uniformly distributed surfactants. The flow dynamics as a consequence of the deposition of a droplet of an insoluble surfactant onto a thin liquid film covering a solid substrate were discussed as a starting point in Chapter 2. A strong focus in this context was on the effect of the conditions in the vicinity of the surfactant source. It was shown, by application of interference and fluorescence microscopy, that the radially outwards directed displacement of the subphase, induced by the surfactant induced Marangoni stresses, is strongly influenced by the conditions near the surfactant source, i.e. the supply of surfactant from the source as the spreading proceeds. A novel oscillatory contact line instability of the surfactant droplet was described which modulates the flow rate of liquid from underneath the droplet.

Considering conditions relevant to surfactant spreading in an oil reservoir in Chapter 3 the influence of a chemically imposed confinement on the sub-phase, along the surface of which a surfactant spreads, was investigated. A pronounced transition in the morphology evolution of the flowing thin film was found to be induced by the spatial restriction imposed through chemical surface patterns. The experimental results are in excellent agreement with numerical simulations reported by Myroslava Hanyak. Regarding conditions in an oil reservoir, results for the spreading of surfactants along liquid-air interfaces can only give a first order approximation. The studies of Chapter 3 were therefore extended to the interface between two thin liquid films in Chapter 4. Here the spreading of a surfactant, soluble in one phase, is studied along the liquid-liquid interface of thin films. Resembling reservoir conditions, the films were subject to both, physical as well as chemical confinement, the later imposed by a wettability pattern.

In the context of surfactant spreading, it is a conceptually entirely new discovery that surfactant induced Marangoni flows cannot only transport surfactants along fluid interfaces but can also efficiently transport surfactants along interfaces exhibiting considerably sized discontinuities. All existing literature in the field of surfactant spreading exclusively regards continuous fluid interfaces. This novel phenomenon is the topic of Chapter 5. The convective surfactant spreading along discontinuous interfaces is directly relevant to the Marangoni driven spreading of surfactants in an oil reservoir. In these porous underground rock formations the oil-water interface is not necessarily connected, such that surfactant spreading through a reservoir involves transport over inter-

face discontinuities.

Besides the spreading of surfactants, I also studied the self-propulsion of surfactant droplets. The results of my experimental studies were presented in Chapter 6 and 7. Self-propulsion dynamics exhibited by insoluble surfactant droplets on thin liquid films are systematically investigated in Chapter 6. Several modes of motion were described, from directed continuous propulsion over a meandering mode of propulsion, that can also be exhibited by a pair of droplets in a synchronized fashion, to an intermittent form of droplet propagation.

The systematic study of the various modes of propulsion is complemented with the outline of a potential application in microfluidic devices in Chapter 7. In this context I am describing the novel phenomenon of transporting solid cargo particles using these self-propelling droplets which can be routed across micro-fluidic networks by controlling the temperature field around the drop e.g. using an infrared laser. The independence from external power sources, integrated electrodes or heating elements to propel the droplets, makes the concept specifically interesting for applications in inexpensive, single-use-type devices.

In this thesis surfactant induced flows are studied in a wide range of system configurations. Confinement effects on the spreading dynamics are investigated systematically. These studies are complemented by the presentation of novel phenomena such as the Marangoni driven convective transport of surfactants along discontinuous interfaces.

Acknowledgements

Looking back at the last four years I am grateful for all the experience I gained and the impressions I received, many of which due to the people that accompanied me during this period.

First I want to thank my wife Heather. After she left the US to live with me in Germany, together with me, she took another step into the unknown and we moved to the Netherlands. Her support in stressful times and inexhaustible understanding for long evenings and weekends in the office were a major factor in the completion of this thesis. The biggest gratitude, however, I owe to her for being the most loving and caring mother to our daughter Annabella.

To Anton Darhuber I am grateful for his commitment as my promoter. I benefited from his excellent advice and enjoyed great scientific freedom during the last four years. Well-thought-out comments and corrections were a great help regarding countless reports and presentations, our papers and last but not least this thesis.

During the study of this thesis the observant reader will have frequently stumbled upon the name Myroslava Hanyak. She conducted the numerical counterpart to most of my experiments. Together we discussed experimental and numerical setups to translate matter into mathematics and finally reached the agreement between our data that we are proud of today. For this excellent collaboration and her companionship during the past four years, I want to thank her.

The financial support of the Dutch Technology Foundation STW and Shell International Exploration and Production is gratefully acknowledged. In this context I also have to thank Axel Makurat, Hans Reinten, Michel Riepen, Herman Wijshoff and Bo Xiao Zhou for their suggestions and feedback during our review meetings. In particular, I want to thank Steffen Berg for his input and feedback in this project and his explanations of EOR techniques. Of course I also greatly appreciate the interest and feedback of the members of my Doctorate Committee, Rob Lammertink, Kees Venner, Dick Broer and Jens Harting.

For all my big and small needs related to metal work, I could always count on Henny Manders who translated my sketches into technical drawings. Jørgen van der Veen was a great help when it came to the selection optical components and always provided a quick fix for all problems related to them. Even though being a member of the Electrical Engineering department, Barry Smalbrugge always had time to discuss the finer points

of photolithography and cleanroom work with me, for which I am very thankful.

Many other inhabitants of Cascade turned the last four years into a great experience. To name and thank just a few, Ad, Aniruddha, Ariel, Brigitte, Christian, Devis, Ergun, Eric, the Florians, Freek, Gunes, Herald, Jan Willems, Jemil, Margit, Matias, Mico, Oleksii, Raoul, Rafal, Sebastian, Stefan, Theo, Valentina, Willem and Yan. Among these a special thanks to Florian G., who frequently shared his joke with me.

And finally, I am truly grateful for my friendship with Jorge and Humberto. Living with them and being introduced to the Hispanic community was an unexpected but most welcome facet of my stay in Eindhoven. We shared many great and memorable times together.

Curriculum Vitae

1982 June 9th	Born in Stuttgart, Germany
1992-2001	High School Education Max-Planckh Gymnasium Nürtingen, Germany
2001-2002	Civil Service Bodel Schwingschule Nürtingen, Germany
2002-2008	Dipl. Ing. Process Engineering (Verfahrenstechnik) University of Stuttgart, Germany Theses: - <i>Simulation of Rarified Gas Flows using the Lattice Boltzmann Method and Molecular Dynamics</i> - <i>Robust Model Predictive Control for Sampled-data Systems: An LMI Approach</i>
2004	Internship University of Belgrade, Serbia
2005	Exchange Student University of Kansas, Lawrence, Kansas, USA
2005	Internship Research and Development Department Lurgi AG, Frankfurt, Germany Topics: <i>Synthetic Fuels, Catalyst Characterization</i>

2008-2012

PhD in Applied Physics

Mesoscopic Transport Phenomena Group

Department of Applied Physics

Eindhoven University of Technology, The Netherlands

Topic: *Experimental study of surfactant induced flows in thin liquid films***Honours and Awards**

2008

LEWA Preis

Awarded for the Diploma thesis at the University of Stuttgart

2011

STOOR Prijs

Onderwijsprijs / teaching award presented at the Eindhoven University of Technology

2012

Winner of the Small Matters Video Contest

Organized by Biomicrofluidics, published by the American Institute of Physics